University of Trento

DEPARTMENT OF PHYSICS

LASER DIAGNOSTICS OF NON–EQUILIBRIUM PLASMAS

NICOLA GATTI

Tutor: prof. Paolo Tosi
Co–Tutor: dr. ir. Gerard van Rooij

XXX PhD Cycle

Nicola Gatti: *Laser diagnostics of non–equilibrium plasmas.*
In partial fulfillment of the requirements for the degree of Doctor of Philosophy . © February 2018

MEMBERS OF THE COMMITTEE

- Professor Richard Engeln, Technische Universiteit Eindhoven, The Netherlands;
- Dr. Olivier Guaitella, Laboratoire de Physique des Plasmas, Ecole Polytechnique route de Saclay, France;
- Professor Giulio Monaco, Universitá degli Studi di Trento, Italy.

Trento, 23rd February 2018

PUBLICATIONS

[1] D. van den Bekerom, N. den Harder, T. Minea, N. Gatti, J. P. Linares, W. Bongers, and G. J. van Rooij. "Non-equilibrium Microwave Plasma for Efficient High Temperature Chemistry". In: *J. Vis. Exp.* 126 (2017). DOI: 10.3791/55066.

[2] L. M. Martini, N. Gatti, G. Dilecce, M. Scotoni, and P. Tosi. "Rate constants of quenching and vibrational relaxation in the $OH(A^2\Sigma^+, v = 0, 1)$, manifold with various colliders". In: *J. Phys. D: Appl. Phys.* 50 (2017), p. 114003. DOI: 10.1088/1361-6463/aa5b28.

[3] L M Martini, N Gatti, G Dilecce, M Scotoni, and P Tosi. "Laser induced fluorescence in nanosecond repetitively pulsed discharges for CO_2 conversion". In: *Plasma Physics and Controlled Fusion* 60.1 (2018), p. 014016. DOI: 10.1088/1361-6587/aa8bed.

[4] Gatti N., Ponduri S., Peeters F.J.J., van den Bekerom D.C.M., Minea T., Tosi P., van de Sanden M.C.M, and van Rooij G.J. "Preferential vibrational excitation in microwave nitrogen plasma assessed by Raman scattering". In: *submitted* (2018).

ACKNOWLEDGEMENTS

Although only one author is listed in the first page of this thesis, several persons are to be thanked for their help in producing the results herein presented.

First and foremost, I would like to thank my tutor Paolo. I am thankful to you for the great assistance you provide me with during my PhD, for all the insightful discussions and for the careful reading of my manuscripts. Such manuscripts report on experimental work that I would have not been able to carry out if it wasn't for the assistance of Luca, Giorgio and Mario. I warmly thank you for having shared your precious expertise with me.

Lucky me, I have been given the opportunity to become a member of two scientific families. In fact, halfway thorough my PhD I moved to Eindhoven (The Netherlands), for an internship in the group of Gerard. To you, Gerard, I am thankful for the proficient guidance, for the many scientific discussions and for all the support I received. But even the finest ship is nothing more than a floating piece of wood if it is not sailed by a proper crew; and Gerard's is definitely one of a kind. Thank you Dirk, Teo, Srinath and Floran for having got me aboard; it was a joyful sail. My thanks go to Qin and Tom too, who joined the team later on, working with you guys was a pleasure.

A special thought goes to Mohammad, who relentlessly kept his optics shop open providing me with the right components just at the right time, without you my optical setup would have not been the same. How to forget the guy next door? Thank you Bram for all the inspiring discussions we had and for hueling[1] with me. Thank you Anna, Fiona, Matteo, Renato, Yannic and all the DIFFER people with whom I had the opportunity to spend a wonderful time. Last but not least, thank you Hennie and Jordy for not having kicked me out of your offices after the many requests of help; your support was crucial.

1 Huel is a delicious nutritionally complete food perfect to be consumed with friends before going to the gym after a long day in the lab.

CONTENTS

1 GENERAL INTRODUCTION

1.1 GLOBAL WARMING

Fossil fuels are the most central energy sources humankind is dependent upon because of their availability, usability and high energy density. Their exploitation enabled rapid and unprecedented developments, boosting economical and technological growth. However, burning fossil fuels not only gives access to the precious energy stored in their chemical bonds, but also releases harmful compounds, like CO and NO_x, and greenhouse gases (GHGs), like N_2O and CO_2. Nowadays, the consequences of the exploitation of fossil fuels are threatening the natural balance of the Earth's ecosystem.

Modern atmospheric CO_2 levels are estimated to be about 140% of their pre–industrial levels, increasing from 280 ppm to 400 ppm between the start of the industrial era (~1750) and 2014 [88]. Although precise measurements have only begun in 1958 at Mauna Loa (Hawaii) by means of an infrared gas analyser, experimental data concerning earlier ages is available thanks to ice core measurements, nevertheless. Atmospheric measurements show that CO_2 concentration has been rising steadily since 1958. The overall increase of the CO_2 atmospheric concentration can be safely attributed to fossil fuel exploitation. This thesis can be supported by:

- judicious analysis of the time frame over which the atmospheric CO_2 concentration has been rising;
- measurement of the $^{13}CO_2/^{12}CO_2$ isotope ratio. In fact, CO_2 emitted from the combustion of coal, gas and oil has a $^{13}C/^{12}C$ isotopic ratio smaller than that of atmospheric CO_2. It is shown that the atmospheric CO_2 isotopic ratio is decreasing at a rate consistent with emissions of CO_2 from fossil origin [81].

Alongside CO_2, CH_4 and N_2O are other two GHGs the concentration of which is influenced by human activity. Especially CH_4 plays a major role in the atmosphere, since its ability to absorb, and then re–radiate, infrared radiation is even larger than that of CO_2 because of its larger number of vibrational modes.

The role that GHGs play in increasing the world's temperature is very well understood. Acting as a gaseous blanket, they absorb infrared radiation preferentially emitted by the Earth towards the space and homogeneously re–emit it. As a result, part of the infrared radiation is stopped from leaving the Earth causing a global temperature

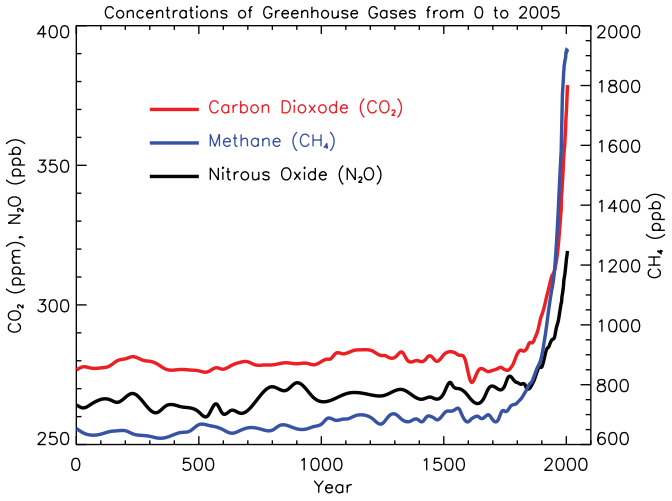

Figure 1: Atmospheric concentrations of important long–lived greenhouse gases over the last 2,000 years. Increases since about 1750 are attributed to human activities in the industrial era. Concentration units are parts per million (ppm) or parts per billion (ppb), indicating the number of molecules of the greenhouse gas per million or billion air molecules, respectively, in an atmospheric sample. Figure 1, page 135 of [74]

increase. The influence of GHGs to the global warming increase is usually measured by means of a parameter called radiative forcing. Radiative forcing is defined as the difference between the energy received from the sun and that amount that is radiated back to space, measured at the top of the atmosphere. As shown in Figure 2, the negative record for the highest radiative forcing pertains to CO_2, even though anthropogenic CO_2 emissions are only a small fraction of the total annual emission of CO_2 [81]. However, the introduction of CO_2 from fossil resources is sufficient to put the delicate natural CO_2 cycle – where photosynthesis and absorption by the oceans are the major sinks for CO_2 – out of balance. The Earth's system, overloaded with the additional introduction of CO_2 from fossils, is not able to regulate the atmospheric concentration of CO_2, that accumulates in the atmosphere. The radiative forcing has increased by about $1.5\,W\,m^{-2}$ due to human activities, the average global temperature is therefore rising steadily.

Consequences of the global temperature increase are well known. The most infamous one is the melting of the polar ice caps. Melting of solid water reservoirs found in the Arctic and Antarctic regions results in a dangerous increase of the sea levels. The effects of the increase in the open water levels will be particularly dramatic for coastal regions that will experience, among others, a decrease of the inhabitable space and an increase in floods and storms. But not only coastal sites will be affected by the climate change, with the mainland experiencing profound modifications as well. On one hand tropical

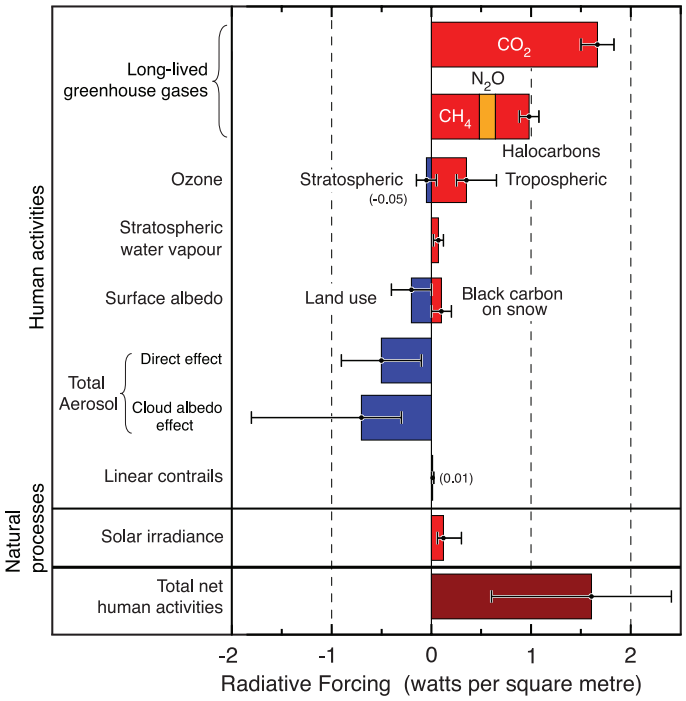

Figure 2: Summary of the principal components of the radiative forcing of climate change. All these radiative forcings result from one or more factors that affect climate and are associated with human activities or natural processes as discussed in the text. The values represent the forcings in 2005 relative to the start of the industrial era (about 1750). Human activities cause signifi cant changes in long-lived gases, ozone, water vapour, surface albedo, aerosols and contrails. The only increase in natural forcing of any signifi cance between 1750 and 2005 occurred in solar irradiance. Positive forcings lead to warming of climate and negative forcings lead to a cooling. The thin black line attached to each coloured bar represents the range of uncertainty for the respective value. Figure 2, page 136 of [74]

deserts will expand while, on the other one, northern region so far covered in ice will turn green. Especially the effects that a global temperature rise will have on the permafrost – a frozen layer of soil typically found in cold regions like Alaska, Scandinavia and Russia – are of a major concern. In fact, since it stores natural reserves of methane, the loss of this frozen layer will result in massive emission of natural gas in the atmosphere. In the end, the release of large amounts of GHGs from their natural storage sites to the atmosphere will trigger a positive feedback behaviour.

Nowadays, there is a common understanding that the global warming is threatening for the Earth natural balance and, subsequently, for our life therein. Many political efforts have been done in this sense by trying to reach an agreement to lower the emission of GHGs. Negotiations have recently gave birth to the Paris agreement, signed the 22nd of April in New York, USA. The Paris agreement aims to hold "the

increase in the global average temperature to well below 2 °C above pre–industrial levels and to pursue efforts to limit the temperature increase to 1.5 °C above pre–industrial levels, recognizing that this would significantly reduce the risks and impacts of climate change." The goal set by the agreement is certainly not trivial to reach. According to the current estimations[1], in order to have at least 50% chance of achieving this goal, current GHGs emissions should not continue for more than ten years. Consequently, the massive use of fossil fuels must therefore be addressed quickly with effective countermeasures, and a transition from a carbon–based energy economy to a sustainable energy one, is essential.

1.2 THE ENERGY LANDSCAPE OF THE FUTURE

Renewable energy sources have the potential to replace fossil fuels at a global scale [84], and then to largely reduce the emission of GHGs. However, this transition brings a multitude of challenges.

Although ultimately provided by the Sun, renewable energy is available on the Earth in different forms. To name a few, we are now exploiting 1) solar energy directly by means of solar panels, 2) wind energy by means of windmills and 3) water energy (hydroelectric energy and tidal energy) mainly. The largest share of renewable energy sources is in electricity generation [24]. Within this context, especially the market of photovoltaic panels is experiencing a rapid growth [83]. Given this increased implementation of photovoltaic electricity generation, some limitations of renewable energy sources become apparent:

- intermittency of solar energy within the diurnal cycle;
- dephasing between production and demand peaks;
- spatial inhomogeneity of the solar irradiation.

A solution that simultaneously tackles these issues is represented by the utilization of CO_2 by means of non–thermal plasma reactors. When powered by renewable electric energy, these reactors can be used to produce synthetic fuels – usually referred to as solar fuels – for the storage of electric energy in chemical form. This approach would solve intermittency and dephasing problems, as excess electric energy can be used at a later stage by burning the solar fuel, and the inhomogeneity as well, since the reactors could be run in regions of maximum solar irradiation. The advantages are sizeable: directly powered by renewable electricity, these reactors will use excess energy to produce value added products from CO_2 that would otherwise be poured in the atmosphere. Additionally, synthetic fuels are especially interesting because they allow the storage of energy in a stable and

1 http://bit.ly/carboncountdown

dense form. The storage of electric energy is arguably the bottleneck limiting the growth of an infrastructure for the production and utilization of green electricity. Technological progress in the storage of electrical energy will therefore enable a much larger exploitation of renewable sources. Consequently, the use of fossil sources will be reduced with the direct consequence of containing the CO_2 emission. However, it is worth noting that carbon containing fuels will still be required in the future for those sectors where energy density is pivotal, e.g hauling and aviation. As a term of comparison, the most efficient lithium–ion batteries can reach energy densities ranging from $0.9\,MJ\,L^{-1}$ to $2.6\,MJ\,L^{-1}$, definitely smaller than $36\,MJ\,L^{-1}$ of diesel or $16\,MJ\,L^{-1}$ of methanol.

Besides the production of solar fuels as energy carriers, this process is an example of Carbon Capture and Utilization (CCU), where the carbon cycle is closed when CO_2 is sourced from industrial exhausts – which are convenient sources of CO_2 in high purity. However, CO_2 will ultimately have to be sequestered from the atmosphere if we are to restore natural levels of radiative forcing.

In addition to their use as fuels for power generation, fossil hydrocarbons are extensively used to produce synthetic compounds. The chemical industry is playing a major role in modern society by synthesizing plastics, pharmaceuticals, fertilizers etc. Because of global development it will continue to grow. It is worth bearing in mind that if it is possible to rely on carbon free energy, the same does not hold for chemicals and materials that will always be carbon based. Consequently, the abandonment of fossils as a source of energy and chemical feedstock requires valid alternatives to be found. One of such alternatives is the plasma synthesis of valuable chemical precursors from abundant compounds like CO_2, CH_4, N_2 and H_2O.

An interesting application of non–thermal plasmas is the dry reforming of CO_2 and CH_4 to produce liquid fuels, like methanol. One might argue that processing CH_4, a gas coming from fossil resources, into a liquid fuel is not helpful in reducing the emission of greenhouse gases. This is only partially true since CO_2 would be utilised in the reaction, hence effectively reducing its emission into the atmosphere. Moreover, the turning of natural gas into methanol yields an energy vector with a much higher energy density, making the storage and transportation of energy through the existing grid more efficient.

Furthermore, the continuously growing human population demands increasing quantities of food to be produced. For this reason, the production of synthetic fertilizers is essential for the intensive agriculture our society relies on. As an example, the worldwide production of ammonia is about 206 million tonnes in 2017. It is mainly produced by means of the Haber–Bosch process, an industrial process that requires high pressure (200 bar) and relatively high temperature (400 °C). It consumes almost 2% of the world total energy production and emits

300 million tons of CO_2 per year [95]. In the context of the electrification of the chemical industry, it is then natural to seek for alternative reactors that are compact, efficient and can directly use green electricity.

Given climate change and an ever growing chemical industry, the quest for innovative sources able to convert abundant compounds, like N_2 and H_2O, and GHGs, like CO_2 and CH_4, into value added products, becomes of a paramount importance. Ultimately, new reactors need to be efficient in driving endothermic[2] chemical reactions and have to be powered by renewable electric energy.

1.3 THE ELECTRIFICATION OF THE CHEMICAL INDUSTRY

In this scenario of a modern chemistry powered by renewable electric energy, it is clear that there is a strong need to modify those processes that have insofar used high temperature, as obtained by the exploitation of fossils, to activate chemical reactions. Therefore, novel reactor concepts, able to directly use electrical energy to efficiently drive chemical reactions, need to be found.

Electrochemical conversion and plasma conversion are, at the moment, the most promising technologies able to directly use green electric energy for the dissociation of CO_2. Electrochemical conversion is performed by supplying electrical energy to the stream of CO_2 by means of two electrodes. Although showing remarkable assets, low performance is preventing this technology to lead the field of CO_2 dissociation. It is indeed recognised that the biggest challenge is represented by low activity, selectivity and stability of the employed electrocatalysts [100].

The plasma conversion approach uses plasma to transfer energy to a molecular gas and then enable chemical reactions. Electrical energy is directly used to sustain a plasma where free electrons, ions, neutral and excited molecules coexist. In order for a chemical reaction to happen, the reactants have to possess sufficient energy to overcome the energy barrier that separates them from the products. In classical high temperature chemistry, this energy is provided in the form of heat and, consequently, all the molecule's modes – rotational, translational and vibrational – are excited as predicted by equilibrium thermodynamics. However, the fraction of energy present in each mode does not equally influence the faith of a chemical reaction. According to Polanyi's laws [31] – which are the standard to study chemical reactions from a microscopic stand point – the key driver to efficiently enable endothermic reactions is the vibrational excitation. From this point of view, vibrational excitation is considered to be essential to obtain the transition state that leads to product formation in the case of

2 Reactions need to be endothermic if the goal is to efficiently store energy in chemical bonds.

endothermic reactions. Consequently, vibrational energy of reactants becomes the control knob since it is required to overcome the energy barrier and assist in achieving high energy efficiency [28].

In this regard, it would be ideal to develop a reactor able to selectively load energy – in the form of electrical energy from renewable sources – into the vibrational modes of the species of interest. If that happens, the system will experience a deviation from thermal equilibrium and the distribution of energy among the available modes will differ from what equilibrium thermodynamics predicts. This state of vibrational non–equilibrium – where more energy is present in the vibrational mode rather than in the rotational–translational ones – is achievable in cold plasmas. Cold plasmas are plasmas for which the electron temperature – a quantity related to the electron mean kinetic energy – is lower than $10\,eV$. Such plasmas are suitable to activate molecules because vibrational non–equilibrium can be enhanced at low electron temperature.

1.4 THIS THESIS

In the context of the electrification of the chemical industry, this thesis sets itself the goal of studying two promising plasma reactors: a nanosecond repetitively pulsed (NRP) discharge and a microwave discharge. The NRP reactor has been investigated for the dissociation of CO_2. The microwave discharge has been used for studies of vibrational energy loading into N_2, as a first step towards the non–thermal synthesis of NO for fertilizer production.

The complicated system that a non–equilibrium plasma represents requires sophisticated diagnostics. Such diagnostics have to be species specific and provide spatial and time resolved information about the quantities of interest, such as temperature (vibrational and rotational), product concentration and energy deposition. Given these requirements, diagnostics based upon the use of pulsed lasers are usually employed to study systems where fast kinetics are at play. The diagnostics of choice are Laser Induced Fluorescence (LIF) and vibrational Raman scattering.

1.4.1 *Studies of hydroxyl radical by LIF*

The hydroxyl radical (OH) is one of the several reactive oxygen species (ROS), together with O, O_3, H_2O_2, HO_2 and $O_2(a^1\Delta_g)$, contributing to oxidation processes in a variety of environments. Concerning the field of plasmas and discharges operating at atmospheric pressure, the importance of OH as an oxidation agent is well known. For example, its role in the chemical kinetics is considered important in plasma assisted combustion [102][103][1] and plasma medicine [82][34].

Additionally, ROS are also of interest in the research areas of biology and life science. In fact, they are produced in the human body during aerobic metabolism and through enzymatic reactions. They are associated with various human diseases generated by the oxidation of lipid membranes. As a first step to understand such a complex mechanisms, the role of OH in the oxidation of Fatty Acid Methyl Esters (FAME) has been recently demonstrated by a joint theoretical and experimental work [63].

Besides the paramount importance of OH as an oxidation agent in plasma medicine, pollutants removal and plasma assisted combustion, recent studies suggest it may also play a critical role in the plasmolysis CO_2. In particular, in a CO_2/H_2O dielectric barrier discharge, kinetic modelling indicates that OH can react with CO to form CO_2 (see reaction R_4 in Table 1) and then limit the CO_2 dissociation [101]. In [101], it has been shown that a small percentage of H_2O already causes a steep drop in the CO_2 conversion, slowly decreasing as the H_2O content increases. H_2O is frequently found in CO_2 plasma conversion technology, either as a part of the initial mixture – when it is used as a cheap hydrogen source – or as a process by–product. Moreover, H_2O is naturally present in industrial waste gas or biogas. When H_2O is present in the mixture, the formation of OH is unavoidable and its role as intermediate of reaction should be taken into account.

However, the presence OH is not limited to that of H_2O in the mixture. In fact, it has been reported that the formation of H_2O – that can be linked to OH by the reaction R_5 in Table 1 – occurs also in the dry reforming of CO_2 and CH_4 by a NRP discharge [91]. Therefore, the formation of OH might be detrimental for the conversion CO_2/CH_4 although H_2O is not added to the initial mixture. In an industrially meaningful plasma CO_2 conversion, the chemical kinetics must then cope with the presence of water, and then of the OH radical.

However, whether OH is desired or not in CO_2 containing mixtures is not completely clear yet. Indeed, a recent study suggests OH to be an important species for oxygenates formation – mainly acetic acid, methanol and ethanol – in the dry reforming of CO_2 and CH_4 by DBDs [116]. See the proposed reaction scheme [116] and the associated reactions Table 1. This is a case in which the kinetics of a transient species can determine both process selectivity to different products and conversion efficiency. Hence, it is clear that the experimental investigation of OH in such discharges is essential to unveil the true chemical mechanisms important for the CO_2 plasmolysis and the direct conversion of CO_2 and CH_4. Because of the relatively fast rates reported in Table 1, OH can play a central role in CO_2 and CO_2/CH_4 discharges, provided it is present in sufficiently high concentration. Consequently, it is importance to quantify it and reveal its kinetics in the aforementioned discharges. Experimental information about its density and temporal evolution can be compared with rate

coefficients of possible reactions to better understand its role in the conversion process.

Reaction		Rate $[cm^3\ molecule^{-1}\ s^{-1}]$
(R_1)	$CH_4 + OH \rightarrow CH_3 + H_2O$	6.68×10^{-15} [116]
(R_2)	$CH_3CO + OH \rightarrow CH_3COOH$	
(R_3)	$CO + OH \rightarrow COOH$	1.50×10^{-12} [60]
(R_4)	$CO + OH \rightarrow CO_2 + H$	1.57×10^{-13} [6]
(R_5)	$OH + OH \rightarrow H_2O + O$	2.5×10^{-12} [2]
(R_6)	$CH_3 + OH \rightarrow CH_3OH$	9.84×10^{-11} [116]
(R_7)	$C_2H_6 + OH \rightarrow C_2H_5 + H_2O$	2.55×10^{-13} [116]
(R_8)	$C_2H_5 + OH \rightarrow C_2H_5OH$	9.34×10^{-11} [116]

Table 1: Possible reactions involving OH in the direct reforming of CO_2 and CH_4.

To this end, LIF is an optimal candidate because of its high spatial and temporal resolution. OH has already been the subject of several studies where LIF has been employed to its investigation [22, 73, 78, 87, 109, 114, 115, 120]. However, work needs still to be done, especially to optimize the use of LIF in molecular mixtures at high pressure where fast variations of the mixture composition and temperature occur.

When using LIF, the electronic ground state density of the target species is inferred by measuring the fluorescence emission due to radiative relaxation of the excited electronic state populated by resonant absorption of light. Consequently, any process that interferes with such a fluorescence emission disturbs the measurement of the ground state molecules. Therefore, knowledge concerning the collisional rate coefficients – rates describing the non-radiative depopulation of a molecule excited state – and the gas composition is required. To this end, number density of collisional partners and their associated energy transfer rates (electronic quenching (Q) and vibrational energy transfer (VET)) need to be known.

In the context of applying LIF to a collisional environment for the measurement of OH number density in a NRP, the work presented in this thesis is twofold. First, a fundamental study is done on a gas cell with the goal of measuring Q and VET rate coefficients for collisional partners found in CO_2 plasmas. Specifically, Q and VET are measured when OH radicals (produced by photo-fragmentation of H_2O_2) are embedded in a gas mixtures singularly containing H_2, D_2, O_2, N_2, H_2O, CH_4, C_2H_2, C_2H_4, C_2H_6, CO or CO_2. In this way, existing literature is updated and enriched with new rate coefficients. Additionally, a novel data reduction procedure is demonstrated. The

obtained spectroscopic information is subsequently used to quantify CO in a NRP. By making the assumption of not having other gases than CO, CO_2 and O_2 in the mixture, the temporal variation of the CO concentration is inferred from OH LIF spectra.

1.4.2 *Monitoring vibrational energy loading by Raman scattering*

The second part of the thesis describes the use of Raman scattering for the investigation of a microwave discharge for the processing of N_2. As compared with LIF, Raman scattering allows the direct measurement of the ground state density of the target species, because collisional processes do not interfere with the measurement. However, LIF and Raman cross sections differ by about three orders of magnitude, making Raman signals much fainter than LIF ones. As a result, the need for long exposure times is the main drawback in using Raman scattering. Nevertheless, the developed setup allowed measurements of rotational (T_r) and vibrational (T_v) temperatures from 500 K to 7000 K, at pressure from 17 mbar to 800 mbar.

The microwave N_2 plasma has been mapped both radially and axially to calculate the ratio T_v/T_r which is indicative of the deviation from thermal equilibrium. The closer T_v/T_r to unity, the closer the gas to thermal equilibrium. Values of T_v/T_r close to four have been measured provided suitable conditions of pressure, flow and input power are met. This is a strong indication that an appreciable amount of energy can be loaded in the vibrational mode.

The investigation is further extended to calculate profiles of energy deposition, both in the rotational/translational modes and in the vibrational one. The energy deposition profile due to the microwave field is larger than the spatial coverage of the diagnostics. Therefore, the diagnostics would not yield correct results if molecules are gaining energy while flowing through the plasma. Hence, measurements performed downstream of the plasma are better at quantifying the overall energy efficiency of the reactor. Such measurements show selective deposition of energy into the vibrational mode (T_v = 2400 K) at a relatively low rotational temperature (T_r = 600 K).

It is calculated that the microwave discharge is able to selectively couple about 23% of the specific energy input (SEI) into the vibrational mode. It is therefore clear that such a microwave flowing reactor is capable of creating conditions favourable for driving vibrationally enhanced chemistry.

2

MEASUREMENTS OF COLLISIONAL ENERGY TRANSFER COEFFICIENTS OF OH

ABSTRACT

Laser Induced Fluorescence (LIF) is intensively used for the detection of hydroxyl radical (OH) in several discharge reactors operating at atmospheric pressure . At this pressure, a quantitative knowledge of the collisional phenomena occurring at the OH excited state is crucial.

This chapter reports measurements of rate coefficients of electronic quenching (Q) and vibrational energy transfer (VET) of OH $A^2\Sigma^+$ ($v' = 0, 1$). The investigation is executed at a constant temperature equal to T = 300 K and in condition of complete rotational thermalization.

The collisional partners are those relevant in the fields of plasma chemistry – the reforming of light hydrocarbons and remedation of CO_2 are two well known examples – and plasma medicine: N_2, O_2, H_2O, CO_2, CO, H_2, D_2, CH_4, C_2H_2, C_2H_4, C_2H_6.

The experimental data is obtained by means of a novel data reduction method – able to solve some drawbacks related to the usual way of measuring rate coefficients. Results of this work are critically compared with published data obtained in condition of partial, or absent, rotational thermalization.

In the end, a large dataset of rate coefficients for the non–radiative de–excitation of OH by means of molecular collisions is given. Principally the knowledge concerning Q and VET of OH $A^2\Sigma^+$ ($v' = 0, 1$) is enriched.

2.1 INTRODUCTION

When using Laser Induced Fluorescence (LIF), the density of a species electronic ground state is inferred by measuring the fluorescence emission. Such emission is the result of radiative relaxation of the electronic state resonantly excited by absorption of laser photons. Consequently, it can be naïvely said that any process interfering with such a fluorescence emission disturbs the measurement of the ground state molecules. Therefore, knowledge concerning the collisional rate coefficients – second order rates with units $s^{-1}\,cm^3$ describing the non–radiative depopulation of a molecules excited state – and the number density of collisional partners composing the mixture is required.

The knowledge of the collisional rate coefficients is crucial when LIF is performed at atmospheric pressure (ATP) in a quantitative fashion. The reason relies on the fact that, at this pressure, collisional quenching can be orders of magnitude faster than the radiative decay. Hence, the fluorescence emission greatly depends upon collision occurring at the excited state. Moreover, collisional processes are collisional partner specific. In the end, the intensity and the spectral pattern of the fluorescence emission varies as a function of composition, temperature and pressure of the gaseous mixture. Collisional energy transfer processes can be divided in three classes:

ELECTRONIC QUENCHING (Q) : non–radiative relaxation from an excited electronic state to a lower one;

VIBRATIONAL ENERGY TRANSFER (VET) : non–radiative relaxation from a vibrational state to a lower one within the same electronic state;

ROTATIONAL ENERGY TRANSFER (RET) : non–radiative relaxation from a rotational state to a lower one within the same vibrational state.

Although the outcomes of these three processes are intrinsically different, they share some common characteristics:

- they transfer population from one state to another without emission of light;
- they are species specific – depending on both collisional partner and target molecule;
- they linearly depend on the collisional partner concentration;
- both RET [44, 45] and Q [16, 17] rates depend on the rotational quantum number of the excited state;
- they have a temperature dependence.

Recent studies show that quantitative LIF is a powerful tool to measure the gas composition with high spatial and temporal resolution, provided the collisional energy transfer rates are known [20, 22, 87]. However, the current availability of collisional rate coefficients is incomplete. Especially experimental data on VET is scarce.

The vast majority of the available data on OH comes from studies performed in the field of atmospheric chemistry [16, 17, 118, 119]. For this reason, the data is limited to collisional partners that are abundant in the atmosphere. From this source, information concerning species like CO_2, CO and light hydrocarbons, that are of primary interest in the field of plasma–chemistry, is not available. Experimental data with these species as collisional partners is provided to some extent by the field of combustion research. However, in this case experiments were performed in flames, therefore at high temperatures [107]. Consequently, this data is not suitable to be used in the field of plasma–chemistry where there is a strong desire to maintain the temperature of the system as low as possible. Additionally, these studies were performed by making assumptions on the flame composition. As a result, species specificity is not guaranteed.

This chapter presents the measurement of collisional rate coefficients at room temperature, at relatively high pressure ($\simeq 100\,\mathrm{mbar}$) and in condition of complete rotational equilibrium. Specifically, electronic quenching and vibrational relaxation of the OH $A^2\Sigma^+$ ($v' = 0, 1$) manifold has been measured with the following species as collisional partners: N_2, O_2, H_2O, CO_2, CO, H_2, D_2, CH_4, C_2H_2, C_2H_4, C_2H_6. As compared to the existing literature, a new technique is used for the acquisition of the experimental data. This improvement solves some issues related to the collection and analysis of the data when either complete thermalization is not ensured, or strong VET is at play. Additionally, a novel method for the data fitting is presented.

2.2 LASER INDUCED FLUORESCENCE

When light interacts with matter, energy can be exchanged. Among many, and limited to the scope of this chapter, this energy exchange can occur through absorption and emission of light. Both the processes are bounded to the presence of a finite number of allowed transitions. These transitions are species specific and all together they form a spectrum, a unique fingerprint that any molecule, or atom, possesses. Knowledge about these specific patterns allows the unambiguous identification of the species target of the investigation.

A range of spectroscopic techniques has been developed and are known to date. LIF is a technique by which the target species is excited to an electronic state via resonant absorption. Fluorescence emission due to radiative decay of the excited state occurs subsequently to the absorption. This fluorescence light is the physical observable.

This section presents a brief overview of the physics of LIF. Given the scope of the chapter, particular emphasis is devoted to the discussion of the collisional energy transfer processes occurring at the electronic excited state. Most of the following material has been adapted from [58], reference to which the reader is pointed to for a more detailed treatment.

LIF has been selected because it shows some characteristics that are desirable for the study of fast processes occurring in a nanosecond pulsed discharges. Specifically:

- the time resolution is given by the temporal width of the laser pulse, usually of the order of tens of ns;
- spatial resolution is high because the signal is collected in scattering mode. The sampled volume is given by the intersection of the pump beam with the collection cone.
- spectral selectivity is available on the detection of the fluorescence as well; Consequently, noise can be effectively reduced by equipping the detectors with band pass filters;
- the signal is recorded directly, and not obtained as the difference between two signals, as in the case of absorption spectroscopy. Hence, sensitivity is greatly enhanced;
- the cross section is high, several orders of magnitude larger than Rayleigh and Thomson scattering [69];
- because of resonant excitation it is not only species specific, but rotational state specific also.

The quantities that can be measured by LIF are:

- the rotational temperature (T_r) that is often tantamount to the gas temperature – since very few collisions are necessary to equilibrate a molecule's rotational distribution to the gas temperature (T_{gas});
- the population of the electronic ground state;
- when the target molecule is embedded in a collisional environment, it can be used as a probe to measure variations in the concentration of the collisional partner – provided VET, Q and the mixture composition are known. An example of the application of this technique to the quantification of CO is given in Chapter 3 .

While the rotational temperature can be obtained from a well established fitting procedure, the quantification of the ground state population is not a trivial task to complete. Indeed, quantitative knowledge about the collisionality of the system is required when LIF is used for

absolute density measurements. On the contrary, absolute quantification of the ground state population can be more easily performed by using a Raman scattering technique. In this case, the ground state is probed directly. Consequently, the scattered light linearly depends on the ground state population, see Chapter 5.

2.2.1 *5–level model*

The LIF process can be mathematically represented by a set of differential equations describing the temporal variation of the relevant states. In this work, five states are considered and the corresponding equations are shown in Equation 1. The Jablonski diagram of the developed 5–level system [22] is displayed in Figure 3.

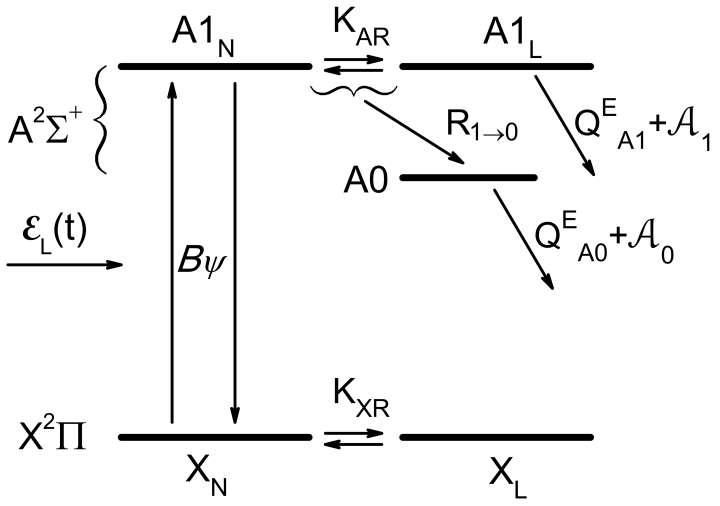

Figure 3: Scheme of the 5–level taken from [22] and slightly modified to adapt to the present terminology. See text for symbols explanation. $\mathcal{A}_1$ and $\mathcal{A}_0$ are the Einstein coefficients.

$$
\begin{cases}
\frac{dN_{X_N}[t]}{dt} &= -BE_L[t]\psi(N_{X_N} - N_{A1_N}) + (F_{X_N}N_X - N_{X_N})K_{X_R} \\
\frac{dN_{X_L}[t]}{dt} &= (N_{X_N} - F_{X_N}N_X)K_{X_R} \\
\frac{dN_{A1_N}[t]}{dt} &= BE_L[t]\psi(N_{X_N} - N_{A1_N}) - Q_{A_1}N_{A1_N} \\
&\quad + (F_A P_{A1} - N_{A1_N})K_{A_R} \\
\frac{dN_{A1_L}[t]}{dt} &= (N_{A1_N} - F_A N_{A1})K_{A_R} - Q_{A1}N_{A1_L} \\
\frac{dN_{A0}[t]}{dt} &= R_{1\to0}N_{A1} - Q_{A0}N_{A0}
\end{cases}
\tag{1}
$$

- $N_X = N_{X_N} + N_{X_L}$ and $N_{A1} = N_{A1_N} + N_{A1_L}$ are the shorthand notations for the populations in the ground and excited state, respectively;
- X_N is the $(X, v = 0, N)$ state absorbing the incident radiation;
- $A1_N$ is the $(A, v' = 1, N')$ state populated by optical absorption;
- X_L is the sum of all the rotational levels of $(X, v = 0)$ but N. In Equation 1, X_N is depleted by absorption of the laser light, populated by stimulated and spontaneous emission from $(A, v = 1, N')$ and by RET collisions from X_L. Refilling of X_N by RET occurs through redistribution of molecules from the lumped state X_L;
- $A1_L$ is the analogous of X_L in the excited electronic state. It is the sum of all the rotational levels of $(A, v' = 1)$ but N'. $A1_L$ is populated by rotational redistribution from the pumped $A1_N$ state and depopulated by spontaneous and stimulated emission and by non radiative decay. In Figure 3, Q^E_{A1} is the rate of de–excitation (non–radiative) electronic quenching and A_1 is the Einstein coefficient for spontaneous emission;
- $A0$ is the sum of all rotational states in the $(A, v = 0)$ state. It is populated by vibrational relaxation from $(A, v = 1)$ state with rate $R_{1\to0}$. It is depopulated by spontaneous emission with rate equal to the Einstein coefficient A_0 and by electronic quenching with rate Q^E_{A0};
- B is the Einstein coefficient of absorption;
- $E_L(t) = W(t)/cS$ is the laser radiant energy density. Where c is the speed of light, S the cross–section at the beam waist and $W(t)$ is the laser energy temporal profile. $W(t)$ is calculated by normalizing the laser temporal profile such that the time integrated $W(t)$ is equal to the pulse energy.
- ψ is the spectral overlap integral of the laser line and the absorption line:

$$\psi = \int_{-\infty}^{+\infty} \epsilon(\nu - \nu_l) b(\nu - \nu_l)\, d\nu,$$

  where $\epsilon(\nu)$ and $b(\nu)$ are the spectral profile of the laser and of the absorption line, respectively.

It is worth pointing out that all the rates of energy redistribution – may they be Q, VET or RET – are state dependent. Therefore, the correct calculation should treat energy redistribution between individual rotational levels by state–to–state energy transfer rates. However, there is poor knowledge of these state–to–state rates. Moreover,

the large number of rotational states involved in the process – since many are populated by rotational energy distribution after the resonant energy transfer $X_N \leftarrow A1_N$ – makes the definition of the system Equation 1 in a state–to–state fashion a difficult task to achieve. Additionally, the applicability of such a system would be limited to a well defined rotational state distribution. For these reasons, it is wiser to use a system of equations as Equation 1 where two fictitious rotational states are considered.

The states X_L and $A1_L$, called in this thesis "lumped" states, are ensembles of rotational states in the ground and excited electronic state, respectively. They are coupled to the two rotational states taking part in the resonant transition, X_N and $A1_N$. An overall transfer rate is applied to describe the rotational relaxation to and from the lumped states. The effective rates K_{XR} and K_{AR} are defined as the average of state–to–state rates describing the exchange of energy between the lumped states and X_N and $A1_N$.

Consequently, such an average rate is meaningful only provided the distribution of rotational states is well defined. It is clever to choose a distribution that naturally occurs and the applicability of which is broad. Such distribution is the Boltzmann distribution, describing the distribution of energy in condition of thermal equilibrium, see Section 4.3 for a thorough discussion. Experimental conditions assuring complete thermalization of the excited state rotational distribution are presented in detail in the next Section 2.4. Additionally, the experimental verification of the rotational thermalization is reported.

2.3 SPECTROSCOPIC SCHEME

In this thesis, LIF is applied to the spectroscopic scheme presented in Equation 2. The hydroxyl radical (OH) has typical lifetime of few µs at room temperature and at pressure of the order of 100 mbar. Consequently, it needs to be produced on demand and to be readily available for excitation by the laser pulse. In this work, OH is produced by photofragmentation of water peroxide (H_2O_2) in gas phase via UV laser light at about 282 nm. Therefore, the same laser pulse serves the double purpose of producing and probing the OH molecules.

$$\begin{aligned} \mathrm{OH}(X, v'' = 0) + h\nu_L \longrightarrow \mathrm{OH}(A, v' = 1) &\longrightarrow \mathrm{OH}(X, v'' = 1) + h\nu_{(1,1)} \\ \downarrow \text{ VET} & \\ \longrightarrow \mathrm{OH}(A, v' = 0) &\longrightarrow \mathrm{OH}(X, v'' = 0) + h\nu_{(0,0)} \end{aligned} \tag{2}$$

The spectroscopic scheme used in the present work is the typical excitation–detection one that involves transitions of the 3064 Å system [21]. It is presented in Equation 2.

The laser is tuned to the $Q_1(1)$ transition of $A^2\Sigma^+(v = 1) \leftarrow X^2\Pi(v = 0)$ branch at 281.913 nm. The nomenclature is the same as the one used by Luque and Crosley for the LIFBASE Spectroscopy Tool [55] and by Brown and Carrington in their book [56]. The relevant angular momenta required to describe the transition are:

S is the electronic spin angular momentum;

J is the total angular momentum;

N = J - S is the total angular momentum excluding the electron spin.

Angular momenta can be coupled in different ways, usually referred to as the Hund's coupling cases. The reader is invited to refer to [56] for a detailed treatment of the subject. Specifically for the transition $A^2\Sigma^+(v = 1) \leftrightarrow X^2\Pi(v = 0)$ of OH, the state $^2\Sigma$ belongs to Hund's case (b) and $^2\Pi$ as well for temperature from 300 K to 500 K [37]. Since the measurements presented in this thesis have been performed at room temperature, both electronic ground and excited states have been modelled by the Hund's case (b) set. The nomenclature then becomes:

$$\Delta N_{F'F''}(N''), \tag{3}$$

where $\Delta N = N' - N'' = -2, -1, 0, 1, 2 \equiv O, P, Q, R, S$ are the possible rotational branches, $F = 1$ is the F_1 sub–manifold such that $J = N + 1/2$ and $F = 2$ is the F_2 sub–manifold such that $J = N - 1/2$. For the special case $F' = F''$ only one value is reported. Primed (') and double primed (") quantum numbers refer to the upper and lower states, respectively.

2.4 EXCITED STATE ROTATIONAL THERMALIZATION

Collisional rates Q^E_{A0}, Q^E_{A1} and $R_{1\to0}$ have a marked dependence upon the rotational state [16, 17]. In the LIF process, a single rotational level of the OH(A) state is populated. Subsequently, this population is redistributed over the rotational manifold by means of RET. Finally, fluorescence emission occurs. Hence, the spectral pattern of the fluorescence light is defined by the rotational distribution obtained by RET.

Thermalization of a distribution is achieved through collisions with the surrounding. For the case of rotational distribution, very few collisions are necessary to achieve a thermalized Boltzmann distribution to the gas temperature T_{gas} [75]. The kinetic of the thermalization is very important when counteracting processes are at play, as it is the case with Q and RET. The former prevents thermalization to happen while the latter drives it. Therefore, it is the balance between these two processes that defines the thermalization of the rotational distri-

bution. Specifically, the rotational distribution is always thermalized during the fluorescence pulse provided

$$K_{AR} \gg Q_{A1}, Q_{A0}, \tag{4}$$

where $Q_{A0} = A_0 + Q_0^E$ and $Q_{A1} = A_1 + Q_1^E + R_{1\to0}$ are the total quenching rates of the A0 and A1 states, respectively. This point is key if the measurement of collisional energy transfer rates is to be performed on a thermalized distribution of rotational states.

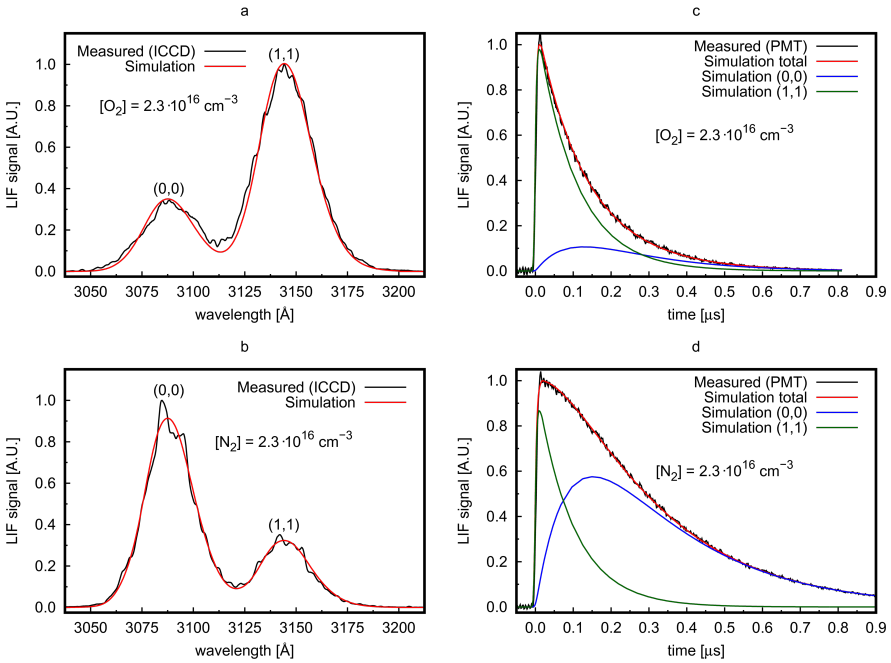

Figure 4: Sample measurement outcomes at total gas pressure of 100 mbar. a,b: fluorescence spectrum with model simulation; c,d: (0,0)+(1,1) bands time resolved pulse with model simulation and individual band contributions. a,c: O_2 collisional partner; b,d: N_2 collisional partner. The two collisional partners represent cases with slow and fast VET, respectively. The simulations are obtained by the fitting procedure described in Section 2.6.

2.4.1 *Measurable quantities*

The measurable quantity is the fluorescence light emitted by the excited OH(A) state. Two complementary measurements can be obtained:

- a time–integrated spectrally–resolved fluorescence spectrum;
- a time–resolved spectrally–integrated fluorescence pulse.

Examples of such measurements are shown in Figure 4. In the presence of VET, fluorescence light is emitted from both the directly excited $v' = 1$ vibrational level, and from the $v' = 0$ one, see Figure 3 and Equation 2. These are the (1,1) and (0,0) bands of the 3064 Å system, respectively.

Both temporal variation and spectral components of the fluorescence signal strongly depend upon the collisional processes the excited OH molecules undergo. It is worth stressing that rotational thermalization is obtained provided Equation 4 is satisfied. The manifestation of a non thermalized rotational distribution can be appreciated in Figure 5.

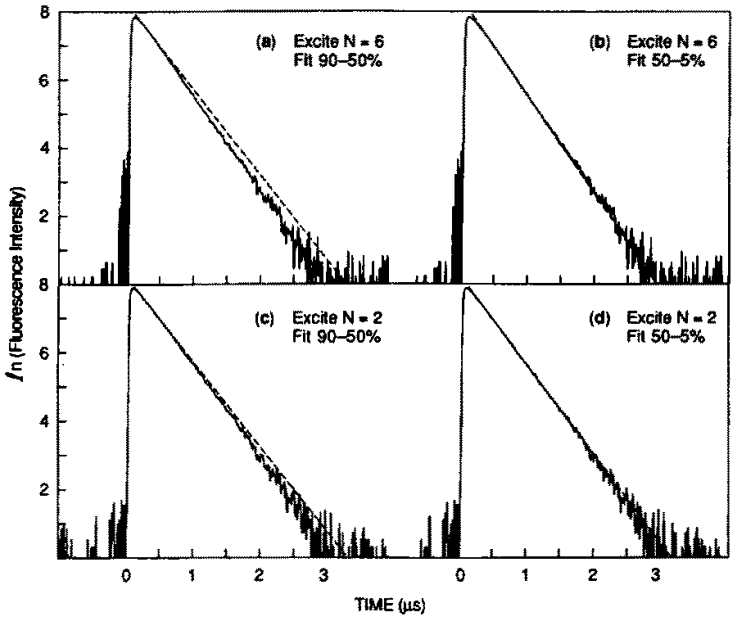

Figure 5: Time resolved OH $A^2\Sigma^+$ ($v' = 0$) fluorescence pulses. OH is embedded in an argon gas bath to ensure (partial) rotational thermalization. The collisional partner is CO_2. Pulses are fitted with a single exponential function the slope of which changes while varying the fitting domain. This is due to the fact that the rotational distribution varies in time since RET redistributes the population during the first hundred of ns. Since Q significantly decreases with increasing rotational level, the higher the excited rotational level the more visible the effect. Reproduced from [119], with the permission of AIP Publishing.

That panel shows the results of a study performed by Wysong et al. on the quenching of $OH(A^2\Sigma^+)$ with CO_2 as collisional partner. They estimated that, when 5 Torr of argon is used as gas bath, initial OH populations of $N' = 2$ and $N' = 6$ will be thermalized within 50 ns and 300 ns, respectively. By looking at Figure 5, a strong indication that complete rotational thermalization was not achieved is found. The effect of a non thermal rotational distribution manifests itself when the collisional partner's quenching rate depends upon the rotational quantum number [13]. Figure 5 shows that the outcome of a fit with a single exponential varies while changing the fitting domain. This is due to the fact that the rotational distribution varies in time since RET redistributes the population during the first hundred of ns. Consequently, the decay of the first part of the fluorescence pulse is faster than that of the tail. The reason is the significant decrease of Q with increasing rotational level; the higher the excited rotational level the more visible the effect. The difference in exciting different rotational levels can be appreciated by comparing the top and bottom panels. Excitation of the $N' = 6$ rotational level results in a large deviation from a single exponential decay. On the other hand, since Q for $N' = 2$ (when CO_2 is the collisional partner) is about the same as a thermal distribution, such effect is reduced when the N'=2 rotational level is excited.

Figure 5 its a clear example of how a non–thermal rotational distribution reflects into a non–single exponential decay of the fluorescence pulse. As explained before, the reason is the variation of the electronic quenching coefficient as a function of the rotational quantum number. When looking at time–resolved LIF pulses, one might argue that, although present, the effect of a non–thermal rotational distribution is not extreme in shaping the pulse. On the contrary, such an effect can be clearly appreciated by investigating the spectrally dispersed signals.

For the sake of presenting the influence that RET and VET have in defining the shape of the fluorescence spectra, simulations are shown in Figure 6. These simulations are obtained by using the LIFBASE Spectroscopy Tool [55] with an experimental resolution equal to 0.2 nm.

Figure 6a displays the nascent spectrum obtained for a condition of absent rotational and vibrational energy transfer ($K_{AR} = R_{1\to0} = 0$). The excited rotational line is the $Q_1(1)$. The emission lines are those for which $\Delta N = N' - N'' = -2, -1, 0, +1, +2$. They correspond to the O, P, Q, R and S branches, respectively. Each branch is double degenerate because of the $F = 1, 2$ sub–manifold, see Equation 3. Among these allowed transitions, only those satisfying

$$N'' = N' - \Delta N = 1 - \Delta N > 0,$$

occur.

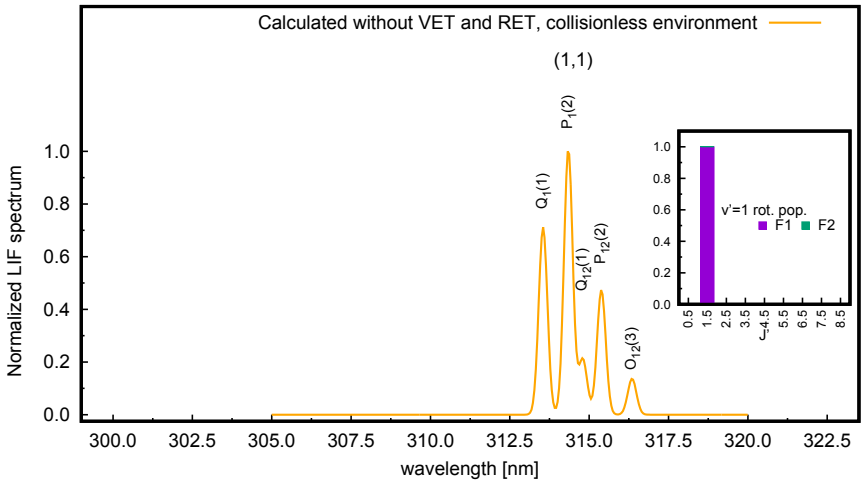

(a) Nascent rotational spectrum, $K_{AR} = R_{1\to0} = 0$.

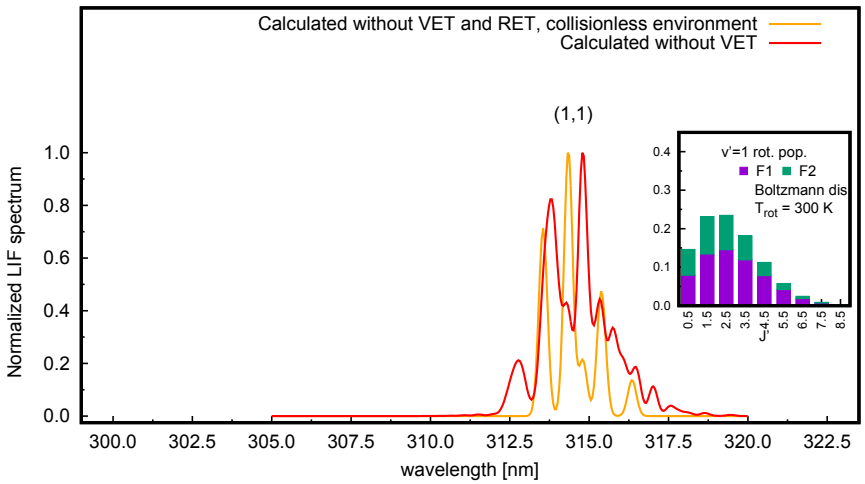

(b) Thermalized rotational spectrum, $K_{AR} \neq 0$, $k_{1\to0} = 0$.

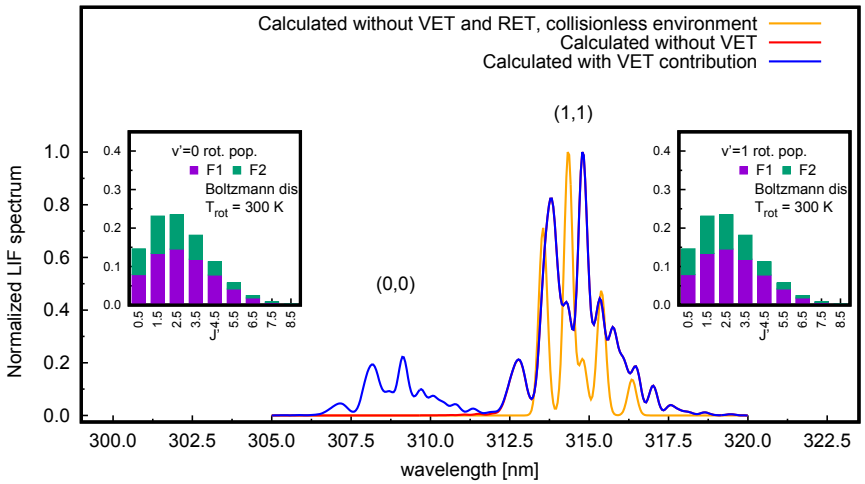

(c) Rotationally thermalized spectrum in the presence VET, $K_{AR} \neq 0$, $k_{1\to0} \neq 0$.

Figure 6: Simulations of emission spectra of OH after excitation of the $Q_1(1)$ rotational line at 281.913 nm. The resolution is set to 0.2 nm. Plots show the contribution of K_{AR} and $R_{1\to0}$ in shaping the spectrum. Histograms show Boltzmann distributed populations obtained by RET.

The spectrum is then composed by five lines, see Table 2, the intensity of which is given by the state–to–state emission coefficients.

	N''	F''	J''	N'	F'	J'	wl [nm]
$O_{12}(3)$	3	2	5/2	1	1	1/2	316.261
$P_{12}(2)$	2	2	3/2	1	1	3/2	315.294
$P_1(2)$	2	1	5/2	1	1	1/2	314.253
$Q_1(1)$	1	1	3/2	1	1	1/2	313.458
$Q_{12}(1)$	1	2	1/2	1	1	3/2	314.709

Table 2: Allowed transitions after excitation of the $Q_1(1)$ line.

Figure 6b shows a spectrum for a population rotationally thermalized at 300 K in condition of absent vibrational energy transfer ($K_{AR} \neq 0$, $K_{1\to0} = 0$). Thermalization acts by redistributing the molecules promoted through the $Q_1(1)$ transition among the different rotational levels. Emission then occurs from several rotational states resulting in a larger number of allowed transitions. The rotational distribution is thermalized if RET is faster than the rate at which the excited state decays,

$$K_{AR} \gg Q_{A1} = A_{Q_1(1)} + Q^E_{A1} + R_{1\to0}, \tag{5}$$

where the total quenching Q_{A1} addresses both radiative and non–radiative processes.

In this work, complete rotational thermalization is guaranteed by performing the measurements at the constant pressure of 100 mbar. A conspicuous amount of He constitutes the gas bath with an additional variable concentration of collisional partner. He is chosen because it ensures a fast rotational relaxation with negligible contribution to the electronic quenching. The rate coefficients for electronic quenching by He is in fact about $4 \times 10^{-14}\,cm^3\,s^{-1}$ [22]. Conversely, with RET rate coefficients of the order of $(1 \text{ to } 2) \times 10^{-10}\,cm^3\,s^{-1}$ (see [42] and the discussion in [22]), RET frequencies of the order of $(3 \text{ to } 6) \times 10^8\,s^{-1}$ are obtained. As long as the total quenching frequency remains lower than about $(3 \text{ to } 6) \times 10^7\,s^{-1}$, RET frequencies are at least one order of magnitude larger than quenching ones. Therefore, the population is rotationally thermalized at any time during the decay of the fluorescence pulse.

With a rotational distribution thermalized at 300 K, low J' are the most populated states, see histograms in Figure 6 for a pictorial representation. Consequently, the emission of the whole vibrational band decays with an effective rate mostly determined by the fast–decaying low J' states.

Experimentally, rotational thermalization has been verified by fitting the fluorescence spectra of a selected sample of measurements. For this check–up, few spectra are measured at high resolution equal to 0.2 nm. Afterwards, since rotational resolution is not required to calculate the vibrational band ratio, measurements are performed at a lower resolution equal to 2 nm to increase the signal intensity.

Figure 6c shows a simulation obtained with the addition of a source of vibrational energy transfer, therefore $R_{1\to0} \neq 0$. The vibrational level $v' = 0$ is then populated through vibrational energy transfer. Subsequently, light is emitted from the rotational manifold of this second vibrational state to form the (0,0) band. The (0,0) band is rotationally thermalized also, because the condition $K_{AR} \gg Q_{A0}$ holds as well.

2.5 EXPERIMENTAL SETUP AND DESIGN CONSIDERATIONS

2.5.1 *Gas handling*

The schematic of the experimental apparatus is shown in Figure 7. Measurements are carried out in a quartz cell 400 mm long and 40 mm in diameter. Three flows are mixed before entering the cell:

Φ^c_{He} : a flow of He of about $\simeq$ 700 sccm is used for the rotational thermalization;

Φ^b_{He} : a smaller amount of He, 10 sccm, flows through a bubbler containing water peroxide 50 *wt*%. H_2O_2 is added to the main stream at its partial pressure in the bubbler;

Φ_{coll} : a variable flow of collisional partner is directly added to the cell.

The flows are controlled by MKS controller. A digitally implemented feedback acting on the flow controllers ensures the partial pressure of water peroxide mixture to be kept constant while changing the concentration of the collisional partner. In order to maintain a constant vapour pressure and avoid condensation on the pipe walls, the bubbler is kept at a constant temperature of 15 °C by a Peltier device. The pressure inside the gas cell is maintained at a constant value of 100 mbar. The calculation of the collisional partner concentration is based on its fraction of the total flow:

$$n_{coll} = n_{tot} \frac{\Phi_{coll}}{\Phi_{coll} + \Phi^b_{He} + \Phi^c_{He}}, \tag{6}$$

where n_{tot} is the total number density in the cell, Φ_{coll} is the collisional partner flow, Φ^b_{He} is the flow of He through the bubbler and Φ^c_{He} is the carrier He flow.

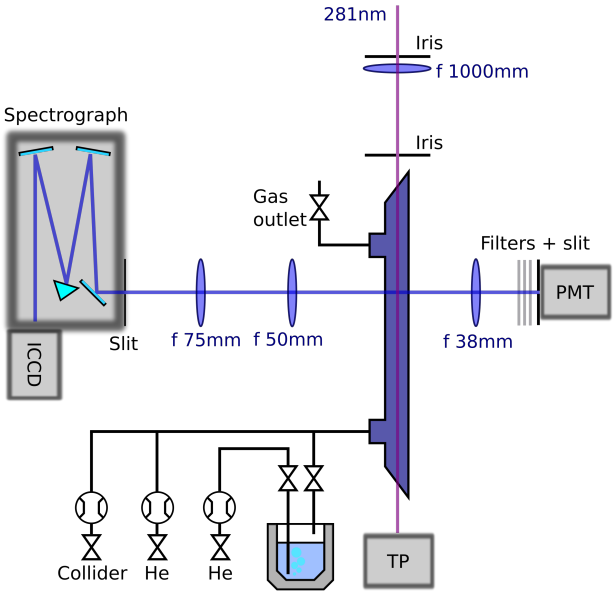

Figure 7: Scheme of the experimental apparatus. The laser is mildly focussed by a long focal length lens. Two dielectric bandpass filters (Semrock 320-40 and Semrock 315-15), a bandpass coloured glass filter (ThorLabs FGUV11) and a set of neutral metallic filters (Thorlabs NDUV**B) are placed in front of the photomultiplier (PMT). TP is a thermopile for laser energy monitoring.

Concerning the special case of H_2O as collisional partner, few words are worth spending on how its concentration is calculated. It is worth remembering that H_2O is sourced from a 50 $wt\%$ mixture of H_2O and H_2O_2. The H_2O concentration in the cell is then obtained from its vapour pressure in the bubbler. However, the prevalence of hydrogen bonding in both H_2O and H_2O_2 leads to considerable deviation from ideal behaviour in H_2O/H_2O_2 mixtures [94]. Consequently, when diluted in such mixture, the vapour pressures of the pure components change. The H_2O vapour pressure $P^{\nu}_{H_2O}$ in the mixture is calculated by the help of a seven–parameters equation [59]:

$$\begin{aligned}\log_{10}[P^{\nu}_{H_2O}[\mathrm{Torr}]] = {} & 19.389127 \\ & - 2861.9133 T^{-1} \\ & - 3.2418662 \log_{10}[T] \\ & - 1.08 \times 10^{-4} T \\ & - 7.92 \times 10^{-6} T^2 \\ & + 1.54 \times 10^{-8} T^3 \\ & - 8.19 \times 10^{-12} T^4 .\end{aligned} \tag{7}$$

By using Equation 7, the H_2O vapour pressure in the mixture at 15 °C is calculated to be equal to 12.7927 Torr. Raoult's law is then used to calculate the partial pressure of H_2O in the bubbler

$$P^{b}_{H_2O} = P^{v}_{H_2O} \cdot \chi_{H_2O} \cdot g_{H_2O}, \tag{8}$$

where χ_{H_2O} is the H_2O mole fraction and g_{H_2O} is the H_2O activity coefficient. The activity coefficient g for H_2O is calculated as

$$g_{H_2O} = \exp\left[\frac{\chi^2_{H_2O}}{RT}\left(B_0 + B_1(3-4\chi_{H_2O}) + B_2(1-2\chi_{H_2O})(5-6\chi_{H_2O})\right)\right] \tag{9}$$

where $T = 288.15$ K is the mixture temperature, $R = 8.3144\ J\ K^{-1}\ mol^{-1}$ is the gas constant, $B_0 = -737.4945$, $B_1 = 85$, $B_2 = 13$ are constants taken from [97][1].

In the end, the H_2O partial pressure in the cell is calculated as

$$P^{cell}_{H_2O} = P^{b}_{H_2O}\frac{\Phi^{b}_{He}}{\Phi^{b}_{He} + \Phi^{c}_{He}}. \tag{10}$$

Similar arguments can be made to calculate the partial pressure of H_2O_2 in the cell – that is in the end the source of OH radicals. Its vapour pressure in the mixture can be calculated by using again a seven–parameters equation [59]:

$$\begin{aligned}\log_{10}(P_{H_2O_2}[\text{Torr}]) = {} & 24.8436 \\ & - 3511.54T^{-1} \\ & - 4.61453\log_{10}[T] \\ & - 3.602\,45 \times 10^{-3}T \\ & - 7.734\,23 \times 10^{-6}T^2 \\ & + 1.783\,55 \times 10^{-8}T^3 \\ & - 2.270\,08 \times 10^{-13}T^4.\end{aligned} \tag{11}$$

Using Equation 11 the H_2O_2 vapour pressure in the mixture at 15 °C is equal to 1.1273 Torr. The H_2O_2 partial pressure in the bubbler can be calculated by using Equation 8 with new values for χ and g. Given the very low vapour pressure of H_2O_2 as compared to H_2O, the relative concentration of the two components in the cell is equal to

$$\frac{P^{b}_{H_2O_2}}{P^{b}_{H_2O}} = 0.02. \tag{12}$$

1 To be found online at: https://catalog.hathitrust.org/Record/001113603

Hence, for a given Φ^{b}_{He} the concentration of H_2O in the cell greatly exceeds that of H_2O_2.

When working with collisional partners different than H_2O, it is important to ensure that the concentration of H_2O in the cell is much lower than that of the collisional partner under investigation. This is necessary to make Q and VET by H_2O negligible. Consequently, because of Equation 12, the concentration of H_2O_2 in the cell is always minute. Hence, since the production of OH via photofragmentation of H_2O_2 is not an efficient process, high laser fluence is required.

2.5.2 *Laser source and optics*

The UV source is a Quantel TDL50 dye laser pumped by a Quantel YG580 Q–switched Nd:YAG laser. The dye is Rhodamine 590 chloride. The dye laser is operated without amplifier and the output energy of the oscillator plus pre–amplifier is $11\,mJ\,pulse^{-1}$. A KDP crystal generates the second harmonic at about $282\,nm$. The UV energy is about $0.53\,mJ\,pulse^{-1}$ and the spectral profile is almost lorentzian with a FWHM of about $10^{-3}\,nm$. With common dye laser bandwidths, of the order of $0.2\,cm^{-1}$, it is easy to tune the wavelength to a single line – rotational lines have typical line widths of about $0.15\,cm^{-1}$ at $760\,Torr$ at $400\,K$ – such that light absorption causes overpopulation of a single rotational level N', and a single spin–orbit sublevel (F_1 or F_2). In this work, the laser is tuned to the $Q_1(1)$ transition of $A^2\Sigma^+(v=1) \leftarrow X^2\Pi(v=0)$ branch at $281.913\,nm$ and with FWHM = $10^{-4}\,nm$ single–line excitation is achieved.

The UV beam is separated from the fundamental one by means of a Pellin–Broca prism. The number of lossy optic components has been carefully chosen to be as low as possible to feed as much energy as possible into the cell.

The beam travels axially through the cell, so that the LIF signal mainly arises from the cell axis. A plano convex lens with $f = 1\,m$ has been chosen to focus the beam in the middle of the cell, where it has a beam waist of about $0.7\,mm$. The relatively large focal length is meant to cure the intrinsic beam divergence in order to

- lower as much as possible the stray light;
- increase the power density to enhance the production of OH by photofragmentation.

It is worth noting that none of the quenching reagents can be photodissociated by the laser photons at $282\,nm$ [121]. For this reason, the increase of laser power density does not affect the concentration of collision partners nor generates new undesired species. Scattered light is the major source of noise, therefore appropriate precautions were taken against it. The beam is spatially filtered by using multiple irises and the collection optics is carefully shielded.

2.5.3 *Fluorescence detection*

For all the collisional partners investigated in this work, both vibrational energy transfer and electronic quenching are at play. Consequently, as displayed in Equation 2, fluorescence light coming from two vibrational bands has to be recorded if both Q_{A0} and Q_{A1} are to be measured.

The system of differential equations Equation 1 can be solved analytically for time $t > t_0$ after the end of the excitation pulse. In this case, the system simplifies to:

$$\begin{cases} \frac{dN_{A1}[t]}{dt} & = -Q_{A1}N_{A1}[t] \\ \frac{dN_{A0}[t]}{dt} & = R_{1\to0}N_{A1}[t] - Q_{A0}N_{A0}[t] \end{cases} \tag{13}$$

where $Q_{A0} = A_0 + Q_0^E$ and $Q_{A1} = A_1 + Q_1^E + R_{1\to0}$ are the total quenching rates of the $A0$ and $A1$ states, respectively. According to this notation, N_{A0} and N_{A1} are the total populations of the $v' = 0$ and $v' = 1$ vibrational states, respectively. The solutions are:

$$\begin{cases} N_{A0}[t] & = \left(N_{A0}[t_0] - \frac{R_{1\to0}}{Q_{A0}-Q_{A1}}N_{A1}[t_0]\right)e^{-Q_{A0}t} + \frac{R_{1\to0}}{Q_{A0}-Q_{A1}}N_{A1}[t_0]e^{-Q_{A1}t} \\ & \simeq \frac{R_{1\to0}}{Q_{A0}-Q_{A1}}N_{A1}[t_0](e^{-Q_{A1}t} - e^{-Q_{A0}t}) \\ N_{A1}[t] & = N_{A1}[t_0]e^{-Q_1 t} \end{cases} \tag{14}$$

where the approximation in Equation 14 is obtained for the case of negligible $N_{A0}(t_0)$. It is then clear how the two bands decay at a different rate. The (1,1) band decays with a single exponential. The (0,0) one shows a double exponential decay accounting for depopulation through total quenching and refilling from the $v' = 1$ state at rates equal to Q_{A0} and Q_{A1}, respectively. By time integrating equations in Equation 14 it is possible to obtain:

$$\frac{\int N_{A0}[t]\,dt}{\int N_{A1}[t]\,dt} = \frac{R_{1\to0}}{Q_{A0}}. \tag{15}$$

Hence, $R_{1\to0}$ can be isolated provided Q_{A0} and Q_{A1} are known. However, the two vibrational bands partially overlap in the spectram region from 3120 Å to 3125 Å, see Figure 4(a,b). Therefore, two domains where overlapping does not occur would have to be found if Q_{A0} and Q_{A1} were to be measured directly. This method requires the use of two photomultiplier tubes (PMTs) and dedicated spectral filters in order to isolate two uncontaminated regions of the two vibrational bands. Moreover, it is also based on the assumption that RET does not vary the fractional spectral area illuminating the PMTs. In the end, a complicated system needs to be implemented to ensure that Q_{A0} and Q_{A1} can be measured directly from the temporal decay of each band, see [118].

Given the challenges and uncertainties in the direct measurement of Q_{A0} and Q_{A1}, this thesis presents a novel method based on the fit of the system of equations shown in Equation 1. The 5–level model is simultaneously fitted to the time–resolved fluorescence pulse and to the spectrally–dispersed spectrum. In this context, both (0,0) and (1,1) bands are collected by the same PMT so as to remove the issue of spectrally isolating the two bands. The signal yielded by the PMT is then equal to:

$$S[t] = CV_s(A_{(1,1)}N_1[t] + A_{(0,0)}N_0[t]), \tag{16}$$

where C is a constant accounting for the collection efficiency of the system, V_s is the sampled volume given by the intersection of the excitation beam and the collection cone, $(A_{(0,0)}, N_0[t])$ and $(A_{(1,1)}, N_1[t])$ are the Einstein emission coefficients and the populations of the $v' = 0$ and $v' = 1$ vibrational bands, respectively.

Two sensors are used to collect the required experimental data. The time–resolved pulse is recorded by a PMT. Two dielectric bandpass filters (Semrock 320-40 and Semrock 315-15) and a bandpass coloured glass filter (Thorlabs FGUV11) are placed in front of the PMT to define a spectral range tight around the (0,0) and (1,1) band emission. A set of neutral metallic filters (Thorlabs NDUV**B) is additionally used to avoid saturation of the PMT and to work within its linear response region. The fluorescence light is collected via a short focal length (f = 38 mm) lens placed at a distance 2f from the cell axis.

A one–to–one image is projected on the PMT, placed at 2f from the lens. To additionally suppress the scattered light contribution to the PMT signal, a 1.5 mm wide slit, oriented parallel to the cell axis, covers its entrance. In such a way, only light coming from a laser chord as wide as the slit is projected on the PMT. The PMT signal is measured as a voltage drop across a 50 Ω resistance by an Agilent Infiniium 54831B oscilloscope, with 600 MHz bandwidth and sampling at 8 bit and 4 Gs s^{-1}.

The same gas volume is also sampled via a separate collection optics illuminating a Shamrock 303i 300 mm focal length spectrograph, where a 1200 grooves/mm reflective grating is used as dispersing element. The sensor is an Andor DH334T-18U-03, 1024 × 1024 pixels iCCD operated at full vertical binning. The iCCD yields the spectrally–dispersed LIF signal.

2.5.4 *Calibration of LIF detectors*

Both the detectors used for the acquisition of the LIF signals have been characterized in order to check their linear behaviour and spectral response.

The linearity of the PMT has been checked by using a UV LED as source of illumination. Results are shown in Figure 8. During the

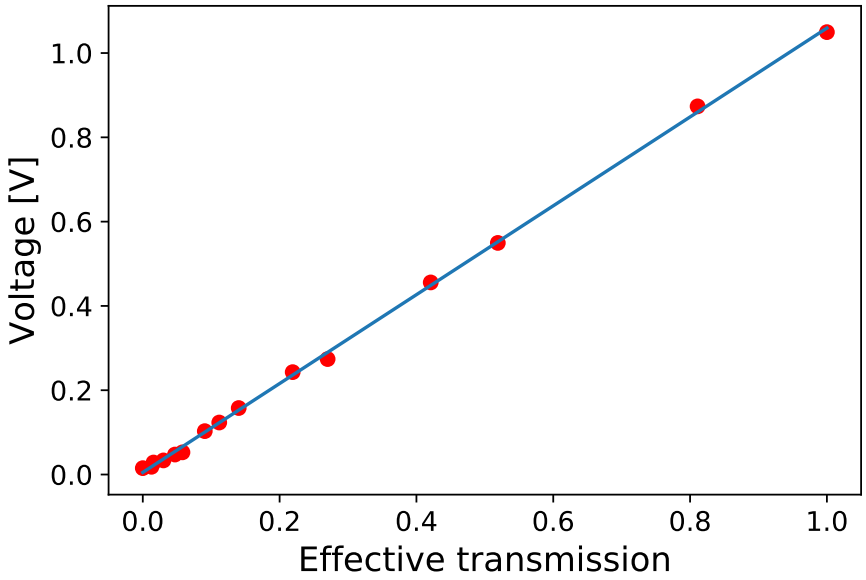

Figure 8: Linearity check for the PMT Hamamatsu H10721-210. The illumination source is a UV LED (UVTOP305) with emission peak at 310 nm and typical FWHM = 10 nm. The intensity of the illumination is varied by using a combination of Thorlabs NDUV[0.1–0.3–0.6–1.0]B neutral metallic filters.

measurements, the signal intensity varies by a large amount while changing the collisional partner concentration. It is important to operate the PMT well within its linear regime. Consequently, neutral filters covering the PMT entrance are added or removed while varying the collisional partner concentration.

In addition to the linearity check, filters covering the PMT entrance have been characterized also, see Figure 9. The combination of the set of filters Semrock 320-40, Semrock 315-15 and ThorLabs FGUV11 covering the PMT entrance has a bandpass transfer function centred at 317 nm with FWHM = 14 nm. This combination has been chosen so as to illuminate the PMT with the spectral window corresponding to the (0,0) and (1,1) bands only – extending from 306 nm to 320 nm. However, the effective transmittance of the set of filters is not flat in this region. Consequently, signals coming from the two fluorescence bands are not presented with the same efficiency at the PMT. Therefore, the total LIF pulse (see Figure 4(c,d)) is given by the combination of two signals – those corresponding to the (0,0) and (1,1) bands – detected with a different efficiency.

It is worth remembering that Q_1^E and Q_0^E (see Figure 3) are calculated by fitting the (0,0) and (1,1) contributions to the total LIF pulse. Hence, a correction that takes into account the non flat transmittance of the filters is required. In this work, it has been chosen to rescale the Einstein emission coefficient of the (0,0) band – that is equivalent

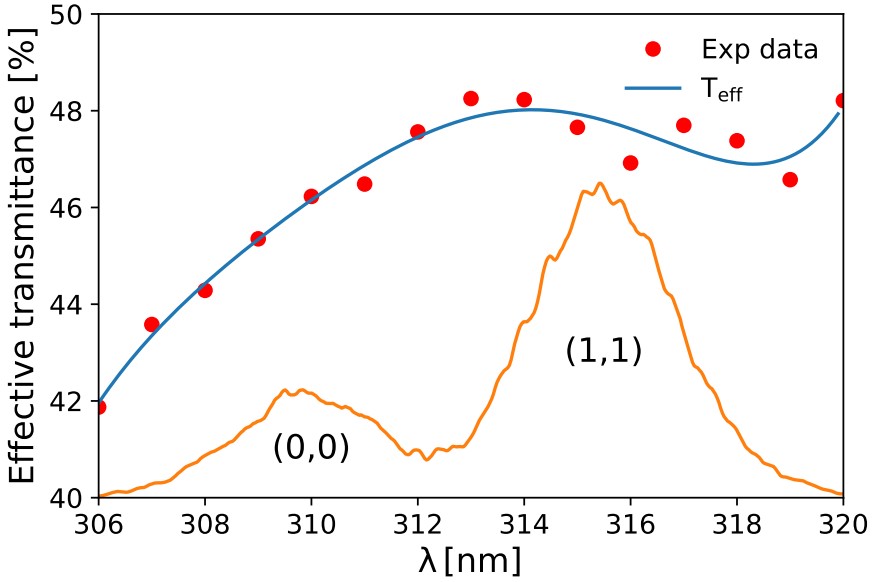

Figure 9: Calibration of the set of filters, Semrock 320-40, Semrock 315-15 and ThorLabs FGUV11, used to filter the signal at the PMT. The effective transmittance has been experimentally measured by using a UV–VIS spectrometer. Vibrational bands are overlaid as to indicate how the measurement can be affected by the filter transfer function.

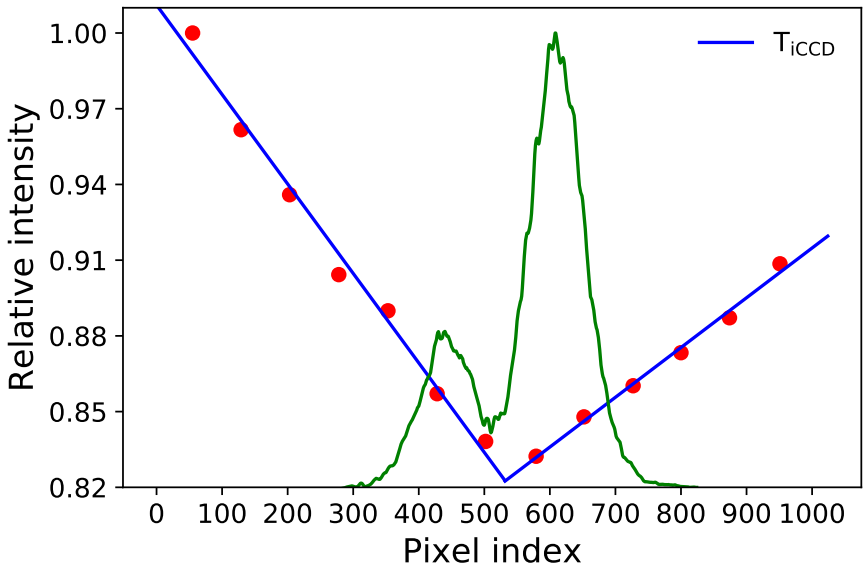

Figure 10: iCCD spectral response calibration. The source of illumination is a UV LED (UVTOP305) with emission peak centred at 310 nm and typical FWHM = 10 nm. Experimental point are obtained by rotating the grating. The overlay with the measured (0,0) and (1,1) indicates how such a non flat response can influence the measurement.

to rescale the collection efficiency for this band. The rescaling factor $t_{(0,0)}$ was calculated as

$$t_{(0,0)} = \frac{\int S_{(0,0)}[\nu]\, d\nu}{\int T_{eff}[\nu] S_{(0,0)}[\nu]\, d\nu} = 1.06, \tag{17}$$

where $S_{(0,0)}[\nu]$ is the (0,0) band fitted function and $T_{eff}[\nu]$ is the effective transfer function of the filters. Such a correction factor is used to calculate a corrected Einstein emission coefficient $A^c_{(0,0)}$ as:

$$A^c_{(0,0)} = A_{(0,0)} t_{(0,0)}. \tag{18}$$

Concerning the acquisition of the spectrally–dispersed LIF signal, also in this case it is important to have knowledge of the efficiency by which the (0,0) and (1,1) band are recorded. In fact, if the response of the iCCD is not flat across its wavelength axis, signals from the two bands might be acquired with different efficiencies. Consequently, error in the estimation of the band ratio – necessary for the calculation of $R_{1\to0}$ – could be introduced. The characterization is obtained by illuminating the spectrometer with the same UV LED used for the PMT linearity check. The iCCD's spectral response is obtained by illuminating different regions of the iCCD by rotating the grating.

The vibrational energy transfer rate $R_{1\to0}$ is calculated from the band ratio $b_r = \int S(0,0)[\nu]\, d\nu / \int S(1,1)[\nu]\, d\nu$. Therefore, it is necessary to take into account the non flat response of the iCCD in the calculation. In the end, the band ratio is calculated as:

$$b_r = \frac{\int S(0,0)[\nu] \cdot T_{iCCD}[\nu]^{-1}\, d\nu}{\int S(1,1)[\nu] \cdot T_{iCCD}[\nu]^{-1}\, d\nu}, \tag{19}$$

where $T_{iCCD}[\nu]$ is the function describing the iCCD spectral response as obtained from Figure 10.

2.6 DATA REDUCTION

As explained in Section 2.4.1, results presented in this thesis have been obtained by using an alternative approach to what is usually done in the literature. The novel procedure is based upon the analysis of:

- the fluorescence pulse including both the (0,0) and (1,1) bands, see Figure 4(a) for an example;
- the fluorescence spectrum, see Figure 4(b) for an example;

to which the 5–level model is simultaneously fitted. The experimental data is conditioned as follows:

i) LIF signals are centred to their maxima and then averaged. Typically, about 1000 pulses are collected for each experimental condition;

ii) in the simulation, the LIF pulse corresponding to the (0,0) band is calculated by using the corrected Einstein emission coefficient $A^c_{(0,0)}$, see Equation 18. This is necessary to account for the different efficiencies by which the (0,0) and (1,1) components of the LIF pulse are detected by the PMT;

iii) the LIF spectra are rescaled by taking into account the spectral response of the iCCD, see Equation 19;

iv) the band ratio is calculated by fitting a LIFBASE [54] simulation to the spectrally–resolved experimental data. The synthetic spectrum is convoluted with a Gaussian function representing the experimental transfer function. A good match is obtained with a rotational temperature of 300 K. Small changes of the rotational temperature do not affect appreciably the fit of the vibrational bands;

v) the temporal evolution of the laser pulse used for the simulation of the 5–level model is experimentally measured. It is obtained by acquiring with the PMT, after removal of the spectral filters, some scattered light at the pump wavelength. During this operation the cell is maintained at the vacuum limit.

2.6.1 *Fitting routine*

In order to obtain reliable results, a reasonably fine step was chosen while varying the collisional partner concentration. Additionally, up to 11 species have been investigated. Consequently, a large amount of data needs to be processed in order to obtain the desired results. Moreover, long computation time is required to simulate the 5–level model. Consequently, the fitting routine, implemented in MATLAB, has been developed with the concept of parallel programming. The fitting routine works on the:

- LIF pulse signal including both (0,0) and (1,1) contributions;
- band ratio calculated from the conditioned LIF spectra;
- Einstein coefficients, conveniently modified to account for the transmittance of the spectrometer;
- experimental profile of the laser pulse.

In order to reduce the computation time, the simulation of the 5–level model is divided in two temporal domains. The complete set of five differential equations is solved for time $t < t_0 = 4 \times 10^{-8}$ s

with the time origin ($t = 0$) aligned to the laser peak. Afterwards, the resulting $N_1[t_0] = N_{A1_N}[t_0] + N_{A1_L}[t_0]$ and $N_0[t_0] = N_{A0}[t_0]$ populations are used as starting values to solve the simplified system of differential equations shown in Equation 13. After 4×10^{-8} s it is possible to simplify the system of equations because the excitation term due to the laser pumping vanishes. The simplified system is numerically solved till 3×10^{-6} s.

This procedure is embedded into a function whose outputs are the time–resolved emission profiles $f[t]_{(0,0)}$ and $f[t]_{(1,1)}$ of the fitted (0,0) and (1,1) bands, respectively. As soon as this function returns to the caller, the integrals $I_{(0,0)} = \int f_{(0,0)}(t)\,dt$ and $I_{(1,1)} = \int f_{(1,1)}(t)\,dt$ are calculated. Afterwards, a zero finding algorithm is fed with 1) the measured band ratio and 2) the ratio $I_{(0,0)}/I_{(1,1)}$. The minimization of

$$\left(\frac{I_{(0,0)}}{I_{(1,1)}}\right)_{\text{model}} - \left(\frac{I_{(0,0)}}{I_{(1,1)}}\right)_{\text{experimental}}, \tag{20}$$

drives the fitting routine.

Fit examples are shown in Figure 4, for two cases of slow (O_2 collisional partner) and fast (N_2 collisional partner) vibrational relaxation.

2.6.2 *Calculation of collisional rate coefficients*

The fitting procedure explained in Section 2.6.1 is performed for each collisional partner concentration and for all the 11 investigated species. The outcomes are the rates Q_0^E, Q_0^E and $R_{1\to0}$. These rates, with units s^{-1}, are function of collisional partner number density.

The next step is to draw what are usually referred to as Stern–Volmer plots, the obtained ones are shown in Figure 11. These plots display the rate of collisional relaxation versus the collisional partner number density. Linear regression is performed on the data to yield slope (k) and intercept (q) of the lines.

The slope is the desired value and it is called collision rate coefficient. Collisional rate coefficients k_{Q0}, k_{Q1} and $k_{1\to0}$, with units $cm^3\,s^{-1}$, are calculated from the Stern–Volmer plots of Q_0^E, Q_0^E and $R_{1\to0}$, respectively. They describe the variation of the rate coefficient as a function of the collisional partner density.

The intercept is a value including contributions from the residual pollutants and the Einstein emission coefficient. It is worth remembering that the main pollutant in the cell is H_2O, since it is sourced from the bubbler, see Section 2.5.1. Measurements are performed in such a way that the total pressure and the partial pressure of H_2O and H_2O_2 in the cell are kept constant while varying the collisional partner concentration. In this way, the small contribution of H_2O and H_2O_2 to Q and VET is constant. Consequently, Q and VET due to residual H_2O and H_2O_2 contributes to q only. Hence, the measurement of the rate

coefficients is not influenced by the residual concentration of H_2O and H_2O_2.

A least squares Levenberg–Marquardt algorithm is used to perform the linear regression. Inverse square errors for both frequency and concentration are used to weight each data point. Values such that either Q_{A0} or Q_{A1} is larger than $5 \times 10^7\ s^{-1}$ are excluded from the fit in order to safely ensure the condition of rotational thermalization, see Section 2.4. The errors on rate coefficients reported in the Table 3 are twice the standard deviation returned by the fitting procedure.

The uncertainty on the collisional partner concentration is determined by the accuracy with which flows, temperature and pressure are known. For the flow, the nominal values given by the manufacturer have been used:

REPEATABILITY ERROR : accounting for casual errors by an amount equal to 0.3% of the set value, or 0.2% of the full scale value, depending on the flow-controller type;

ACCURACY : equal to 1% and accounting for the systematic error.

Both the linearity and the absence of noticeable hysteresis effects – that can indicate stagnation in the cell – have been experimentally verified. A further source of error is the gas correction factor (GFC) of the He flux measurement. Typically, for thermal mass flow controllers, the GFC of He is not constant over the whole range of operation. As shown in [38], the GFC of He increases up to 7% when the flow rises to 50% of the full scale (f.s.). On the contrary, it remains almost constant and equal to the nominal value at low flows, namely within about 15% of the f.s. Given these limitations, the carrier flow of He, equal to 700 sccm, has been regulated by a 7250 sccm f.s. device. This precaution is taken to operate the flow controller safely within its nominal GFC region. Nevertheless, an additional 2% uncertainty has been introduced to account for inaccuracy in the determination of the He GFC. Errors in the measurement of pressure and temperature are set to a nominal 0.5% of the value read by the capacitive gauge and to 1% of the measured room temperature, respectively.

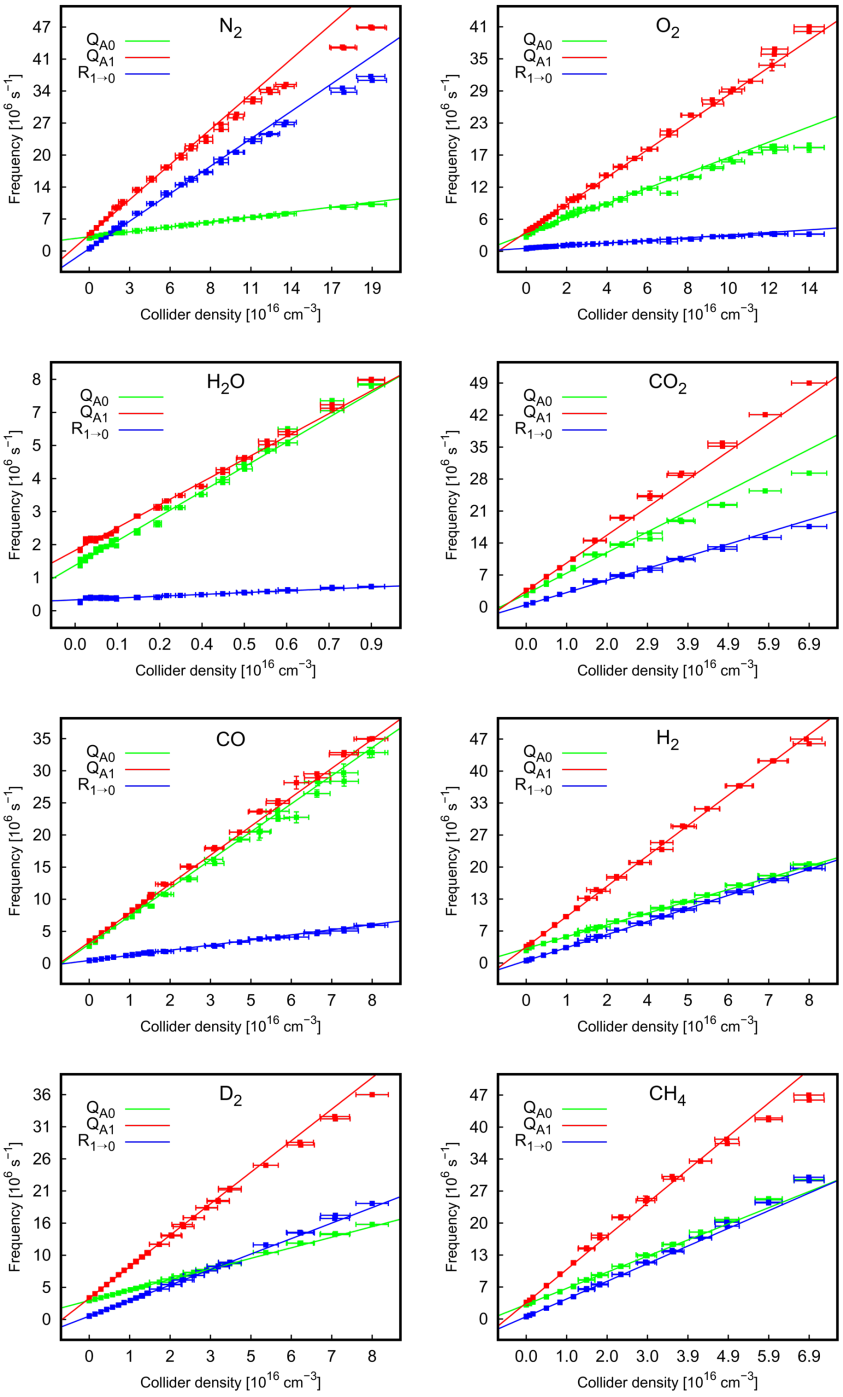
N2
O2
H2O
CO2
CO
H2
D2
CH4
QA0
QA1
R1→0
Frequency [10^6 s^-1]
Collider density [10^16 cm^-3]

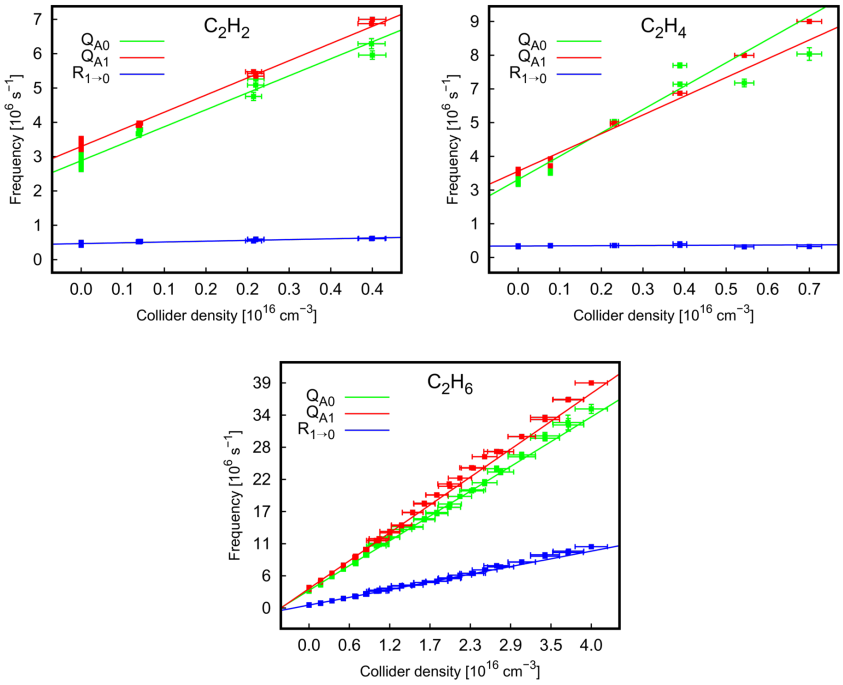

Figure 11: Stern–Volmer plots for the investigated collisional partners. Each plot contains the data and the fitting of the three parameters Q_{A1} (red), Q_{A0} (blue) and $R_{1\to0}$ (green).

2.7 RESULTS AND LITERATURE COMPARISON

Rate coefficients obtained from the fitting of the Stern–Volmer plots, shown in Figure 11, are reported in Table 3. The comparison with the available literature is made with reference to five publications. The data is presented in Table 4 to Table 11.

Copeland [16], Wysong [119] and Tamura [107] performed their investigations by pumping the $v' = 0$ vibrational level. Consequently, neither quenching of the $v' = 1$ vibrational level nor vibrational relaxation could be measured. In that case, the only relevant parameter is the quenching of the $v' = 0$ vibrational level. In those works, a direct measurement of the Q_{A0} rate coefficient was performed by fitting an exponential function to the time resolved fluorescence signal. On the contrary, values of k_{Q0} obtained in this work by means of a three parameters fit. It is worth bearing in mind that such a fit is performed in condition of non–negligible Q_{A1} and $R_{1\to0}$. Therefore, convergence of this data to that reported in [16, 107, 119] can be considered as a robustness test for the method presented in this thesis.

Copeland [17] and Williams [118] performed studies with excitation of the $v' = 1$ vibrational level. LIF spectra were measured with vibrational resolution. Additionally, (0,0) and (1,1) bands were spectrally isolated to directly measure their temporal evolution. Specifically, the (0,0) and (1,1) time resolved signals were fitted with single

Collisional partner	k_{Q0} $[10^{-11}\,cm^3\,s^{-1}]$	k_{Q1} $[10^{-11}\,cm^3\,s^{-1}]$	$k_{1\to0}$ $[10^{-11}\,cm^3\,s^{-1}]$
N_2	3.78 ± 0.08	27.0 ± 0.7	21.09 ± 0.26
O_2	13.50 ± 0.27	24.15 ± 0.48	2.32 ± 0.07
H_2O	65.6 ± 1.3	60.6 ± 2.2	4.81 ± 0.28
CO_2	45.5 ± 1.1	61.4 ± 3.5	26.7 ± 0.7
CO	38.9 ± 0.6	40.1 ± 1.5	7.09 ± 0.11
H_2	20.8 ± 0.5	53.5 ± 1.8	23.05 ± 0.33
D_2	14.89 ± 0.11	44.5 ± 1.2	21.88 ± 0.40
CH_4	34.6 ± 0.5	71.3 ± 2.4	37.8 ± 0.6
C_2H_2	82.7 ± 4.1	84 ± 10	3.90 ± 0.46
C_2H_4	96 ± 6	77 ± 7	0.68 ± 0.49
C_2H_6	74.9 ± 0.9	84.3 ± 3.5	23.30 ± 0.31

Table 3: Rate coefficients of total quenching k_{Q0} and k_{Q1} of the two vibrational states $(A, v = 0)$ and $(A, v = 1)$, respectively, and vibrational relaxation $k_{1\to0}$. Data corresponds the slope of the Stern–Volmer plots shown in Figure 11.

and double exponentials, respectively, to obtain the values of Q_{A0} and Q_{A1}. $R_{1\to0}$ was calculated by means of Equation 15.

Issues related to the isolation of the partially overlapping vibrational bands were evidenced. The ambiguous choice of the spectral domains introduces errors in the calculation of the band integrals in Equation 15. Consequently, the obtained results depend on the definition of the spectral domains. Additionally, a double exponential function with similar decay constants was fitted to the (0,0) band. This is an extra weakness in the estimation of Q_{A0} and Q_{A1}.

Concerning the condition of rotational thermalization, the investigations of Copeland [16, 17] were performed in conditions of negligible rotational relaxation. This was required in order to study the dependence of the collisional rates on the rotational quantum numbers. Specifically, the He background pressure was intentionally kept at 30 mTorr and the collisional partner partial pressure did not exceed 200 mTorr. These precautions were necessary to reduce the rotational relaxation and then measure the rates of isolated N' levels. Conversely, Williams did not performed such a rotational investigation and single excitation of the $Q_1(2)$ rotational line was reported in [118]. However, poor rotational thermalization was achieved due to the low partial pressure of He equal to 1 Torr. Consequently, indications that the OH rotational distribution was not thermal are frequently found in the paper.

It is worth mentioning that in the work of Tamura [107], both the rotational state selected for excitation and the conditions of rotational thermalization are not specified.

2.7.1 k_{Q0}

In [16], Copeland investigated the rotational level dependence of the quenching rates. He selectively excited rotational levels with quantum numbers N' varying from 0 to 7. Given the goal of the investigation, measurements were performed at low pressure in condition of negligible rotational energy transfer. Consequently, this data is difficult to compare with the results presented in this thesis that are obtained in condition of complete rotational thermalization. Nevertheless, some conclusions can still be drawn by looking at the comparative tables, from Table 4 to Table 11.

There is satisfactory agreement for the case of diatomic molecules, CO, N_2, O_2, H_2, D_2, especially when low rotational levels are excited. This is consistent with the qualitative picture that a rotational distribution, thermalized at room temperature, would decay with a rate defined by the low rotational states. By comparison with data reported by Copeland [17], the indication that the k_{Q0} obtained in condition of rotational thermalization is an average value over the low N' values is found. For the case of O_2, for example, value reported in this thesis, and that of Wysong [119], are about 20% lower than the $N' = 0 - 2$ values measured by Copeland. Conversely, a better match is found when the $N' = 3$ rotaional level is excited.

The specific case of CO_2 shows a strong dependence on the rotational quantum number so comparison to data obtained for a thermalized distribution is not feasible.

For H_2O, the value reported by Copeland is larger than that obtained in this work. In this thesis, the concentration of H_2O in the cell was indirectly estimated from thermodynamic properties of the H_2O/H_2O_2 mixtures, see Section 2.5.1. Wysong performed direct measurement of the humidity of the Ar carrier flowing through a H_2O bubbler [119]. Data reported in this work is in good agreement with the results of Wysong. Consequently, there are indications that the value reported by Copeland might suffer of errors in the estimation of the H_2O concentration.

A noticeable mismatch is found for values obtained for the light hydrocarbons. In this case, the data reported in this thesis is generally larger by 20–25% than the largest value measured by Copeland [17] – corresponding to excitation of $N' = 0$. It is worth noting that, due to the slow vibrational relaxation, Q_{A0} is deduced from a weak (0,0) band for the cases of C_2H_2 and C_2H_4. Moreover, because of the fast Q_{A0} and Q_{A1}, the investigation is limited to small concentration of collisional partner. Consequently, Stern–Volmer plots are composed

of a limited number of data points, see Figure 11. As a result, there is a large uncertainty in the determination of k_{Q0}.

The agreement is good with the data obtained by Wysong [119], available for O_2, H_2O, CO_2, although the 5 Torr Ar bath appears not to be sufficient to ensure complete rotational thermalization.

In the end, the agreement of the k_{Q0} values with literature data is generally satisfactory, confirming the validity of the procedure presented in this thesis.

2.7.2 k_{Q1}

The comparison with literature of values of k_{Q1} is performed with reference to [118], for a partially relaxed rotational distribution, and to [17], for individual low N' levels. Considerations are analogous to those drawn for k_{Q0}. However, literature data for k_{Q1} is scarce, being available for N_2, O_2, H_2O and CO_2 only. The agreement with the results reported in Table 3 is generally good and always within the experimental error. Values reported in this work are usually larger than those found in literature for conditions of partial rotational thermalization.

2.7.3 $k_{1\to0}$

Concerning vibrational relaxation, the data presented in this work is generally in good agreement with the literature. This is true except for the case of H_2O. In this case, the value obtained in this work is about 35% lower than the only one available in literature. It is worth remembering that values obtained for H_2O suffer from additional uncertainties in the calculation of its concentration. This point was recognised and addressed by Wysong in [119] via direct measurement of the relative humidity. However, because excitation of $v' = 0$ level, no vibrational relaxation was measured in [118]. Williams did not mention in [118] how H_2O concentration was estimated. He obtained a value of $k_{1\to0}$ definitely larger than the one presented in this thesis. However, it is reasonable to accept the latter as the more precise. This conclusion can be made by noting the good agreement for the case of k_{Q0} between the value reported in this thesis and the one calculated by Williams – who performed direct measurement of H_2O concentration. Consequently, it is reasonable to consider the indirect estimation of the H_2O performed in this work as reliable. Hence, this argument can be extrapolated to validate the value of $k_{1\to0}$ reported in this work.

2.8 CONCLUSIONS AND OUTLOOK

Results obtained in this work are reliable, since satisfactory agreement is found with the relevant literature. However, it is worth remembering how the majority of the data found in literature was obtained in condition of poor or absent rotational thermalization. Therefore, the condition of complete rotational thermalization – achieved by using a conspicuous amount of He as gas bath – makes the data reported in this data valuable. This is especially true when this dataset is used for the investigation of atmospheric pressure discharges where rotational thermalization is often found.

However, there are cases where complete thermalization is not achieved even in atmospheric pressure discharges. For example, partial rotational relaxation can be encountered at the borders of an APPJ, where the air content is significant in comparison with the noble gas used in the jet. Another example is found in molecular gas discharges such as those obtained in air or in CO_2/CH_4 mixtures – where $K_{AR}/Q_{A0,A1} \ll 1$ because of the fast quenching due to the abundant molecular species. In these cases, a critical reading of the literature indicates that the effective rate constants might be slightly lower than the values reported in this thesis. Variations are found to be of the order of 10–20%, This should be taken into account as a possible source of error when data obtained in condition of complete thermalization is used for the investigation of systems showing partial thermalization.

2.8.1 *Use of collisional rate coefficients*

In the work presented in this chapter, the knowledge of the collisional partner concentration allowed the measurement of the collisional rate coefficients. Once the rate coefficients are known, they can be used to solve two different problems:

OH QUANTIFICATION : in this case, two additional pieces are required to solve the puzzle. First, the collisional partner concentrations has to be determined. Second, the diagnostic apparatus need to be calibrated. The first point is necessary to determine the loss in fluorescence light caused by quenching. The second, as any calibration, correlates the measured signal with the concentration of the target species. If only one of the two requirements is not met, the absolute quantification cannot be performed.

MEASUREMENT OF COLLISIONAL PARTNER CONCENTRATION : in this case the knowledge of the collisional rate coefficients is used to quantify the concentration of the collisional partners. The problem can be solved only if the collisional partners com-

posing the mixture are known. If such collisional partners are independent, i.e. their concentrations are not related, the problem can be solved analytically only if they are not more than three, see system of Equation 21. On the other hand, if the kinetics and the stoichiometry are known, the problem can be solved analytically for more than three collisional partners also. An example is a mixture of $CO_2/CO/O_2/H_2O$ where the stoichiometry of the system can be assumed from the scheme $CO_2 \rightarrow CO + \frac{1}{2}O_2$.

The second way of using the rate coefficient is particularly interesting. In that case, the information is obtained from the temporal decay of the pulses and from the band ratio of the fluorescence spectrum. Consequently, a calibration of the system is not required. This is markedly relevant when the calibration has to be performed on transient species, as it is the case for OH. Such a calibration is a though task, since it requires the use of source with well known characteristics. For example, the setup used in this thesis has been calibrated on a source of OH molecules based on the dissociation of H_2O_2 in a DBD. The apparatus was carefully calibrated by using a broadband absorption spectroscopy technique [58, 62]. It is worth bearing in mind that absorption coefficients are generally known with uncertainties of the order of 20%. Hence, such calibration introduces systematic errors when used for absolute quantification. However, if the apparatus is calibrated, both the target molecule and the collisional partners can be quantified simultaneously.

2.8.2 *Quantification of the collisional partners*

The combination of rate coefficients (k_{Q0}, k_{Q1}, $k_{1\rightarrow0}$) is a fingerprint unique to each collisional partner, see Table 3. Therefore, when LIF is applied to a mixture containing OH and a set of collisional partners, it is possible to appreciate variations in the collisional partner concentrations. The problem can be solved for mixtures containing not more than three different species. The system of equations to be solved is:

$$\begin{cases} Q_{A0} &= k^X_{Q0} n_X + k^Y_{Q0} n_Y + k^Z_{Q0} n_Z \\ Q_{A1} &= k^X_{Q1} n_X + k^Y_{Q1} n_Y + k^Z_{Q1} n_Z \\ R_{1\rightarrow0} &= k^X_{1\rightarrow0} n_X + k^Y_{1\rightarrow0} n_Y + k^Z_{1\rightarrow0} n_Z \end{cases} \tag{21}$$

where X, Y and Z are the three collisional partners, n is the unknown concentration of each of them and the LHS terms of the equations are the measured rates. Such a procedure was demonstrated in [20] for $He/air/H_2O$ and $Ar/air/H_2O$ mixtures. Additionally, the technique was also applied for measuring the penetration of air and H_2O in the effluent of an APPJ for plasma medicine applications [22, 63, 87]. In

this section a general remark on the applicability of such a method is given.

Figure 12 shows histogram representations of the nominal data reported in Table 3. With this representation it is possible to appreciate how k_{Q0}, k_{Q1} and $k_{1\to0}$ vary among the investigated collisional partners. It is clear that the distributions of k_{Q0} and k_{Q1} are noticeably different than that of $k_{1\to0}$. For the mixture $CO/CO_2/O_2$, $k_{1\to0}$ is the best candidate to look at when it comes to measure variations in the collisional partner concentrations. In fact, when comparing CO_2 with CO, the relative variations of k_{Q0}, k_{Q1} and $k_{1\to0}$ are 17%, 53% and 376%, respectively. Clearly, the variation in the rate of vibrational energy transfer is the largest.

There is an important caveat on the applicability of the spectroscopic method presented in this section. The system of equations shown in Equation 21 can be solved only if Q_{A0}, Q_{A1} and $R_{1\to0}$ can be measured. As presented in this chapter, the measurement of Q_{A0} and Q_{A1} is intrinsically different than the measurement of $R_{1\to0}$. Specifically, Q_{A0} and Q_{A1} are calculated from the time decay of the fluorescence pulse, see Equation 14, while $R_{1\to0}$ is obtained from the band ratio, see Equation 15. Consequently, the conditions for which the two measurements can be performed are different.

The calculation of $R_{1\to0}$ requires the measurement of the (0,0) and (1,1) bands with sufficient confidence, together with the measurement of Q_{A0}. A reliable measurement of the two bands can be performed provided the collisional partner is characterized by a sufficiently fast VET. Conversely, the way Q_{A0} is measured from the LIF pulse requires the time decay of such a pulse to be much longer than that of the excitation one. Therefore, a strict condition is posed to this last measurement. If this condition were not met, the temporal decay of the fluorescence would be dominated by the decay of the laser pulse. Consequently, the measurement of both Q_{A0} and Q_{A1} cannot be performed if such rates are comparable with the characteristic decay frequency of the excitation pulse. This point poses important constraints to the applicability of the technique.

For example, CO_2 is characterized by a very fast $k_{Q1} = 61.4\,cm^3\,s^{-1}$. As a result, it is found that the measurement could be performed only with the addition of up to $\simeq 4$ Torr of CO_2. This constraint clearly depends upon the width of the excitation pulse. Hence, shorter pulses of the order of few ps would definitely extend the range of applicability of the technique. Nevertheless, information can be obtained also when the only measurable quantity is the band ratio.

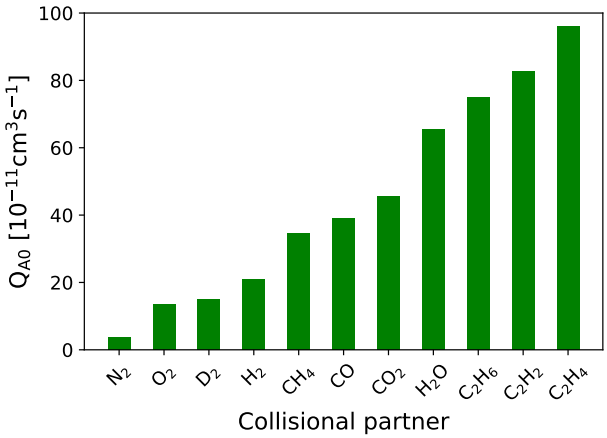

(a) Histogram representation of the total quenching rate coefficients k_{Q0}.

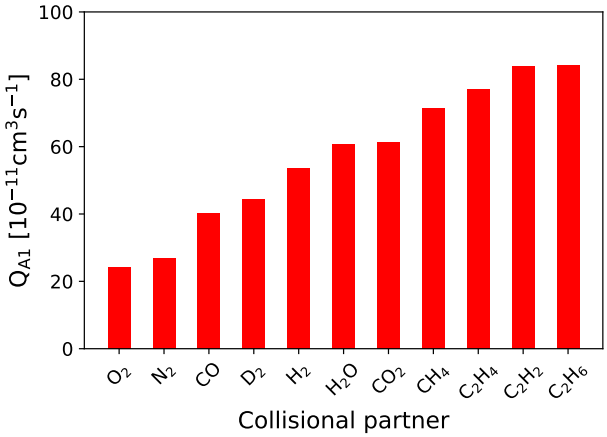

(b) Histogram representation of the total quenching rate coefficients k_{Q1}.

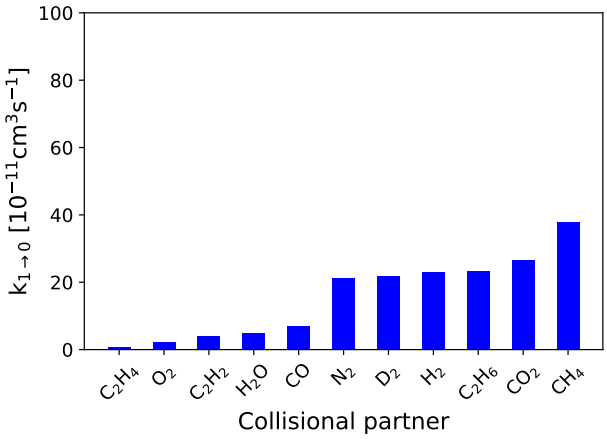

(c) Histogram representation of the vibrational relaxation coefficient $k_{1\to0}$.

Figure 12: Histogram representations calculated by using the nominal data for k_{Q0}, k_{Q1} and $k_{1\to0}$ reported in Table 3. Collisional partners are order for increasing rate coefficient. A two step behaviour distinguishes the $k_{1\to0}$

In that case, Q is too fast to be measured, but the two (0,0) and (1,1) can still be appreciated in the fluorescence spectrum. Therefore, their ratio can be calculated to yield values of $k_{1\to0}/k_{Q0}$. Such information is relevant if the collisional partners show different values of $k_{1\to0}/k_{Q0}$. For example, for the mixture $CO/CO_2/O_2$

$$\left(\frac{k_{1\to0}}{k_{Q0}}\right)_{CO_2} \simeq 0.59 \quad \text{and} \quad \left(\frac{k_{1\to0}}{k_{Q0}}\right)_{CO} \simeq \left(\frac{k_{1\to0}}{k_{Q0}}\right)_{O_2} \simeq 0.18. \quad (22)$$

Hence, a variation in the band ratio can be unambiguously associated to the variation of the CO_2 concentration. Such a method is demonstrated in Chapter 3.

2.8.3 *Temperature dependence*

This investigation was performed at room temperature. Consequently, the use of this data at higher temperatures requires the application of correction factors. Unfortunately, there is poor knowledge on the temperature dependence of both Q and VET.

Both Q and VET exhibit large cross sections and substantial dependence upon temperature and rotational level. These characteristics indicate that both processes are the result of the formation of a transitory complex governed by attractive forces [18]. Different models involving attractive forces have therefore been developed [104]. However, their experimental verification is limited to temperatures from 200 K to 400 K and from 1000 K to 2000 K only [77]. Generally, the temperature dependence of the cross section – of both Q and VET – can be described by the empirical expression

$$\sigma[T] = \sigma[\infty] \exp\left[\frac{\epsilon}{k_b T}\right], \quad (23)$$

where $\sigma[\infty]$ is the value of the cross section at very high temperature, k_b is the Boltzmann constant and ϵ is a quantity related to the well–depth of the attractive potential [77, 104, 107].

In [107], the validity of Equation 23 has been tested for N_2, O_2, H_2O, H_2, CO_2, CO, CH_4, H and OH for temperature from 200 K to 3000 K. However, data is available for k_{Q0} only. Moreover, there are some caveats. In fact, 1) Tamura does not indicate which rotational level was excited and 2) all the measurements at high temperature were performed in flames – with the associate issue of not having complete control over the mixture composition.

In [104], values for k_{Q0}, k_{Q1} and $k_{1\to0}$ are reported for N_2, O_2 and CO_2 only. Moreover, the dataset was obtained at low temperature, from 195 K to 294 K.

In [77], measurements are performed from 300 K to 1200 K for N_2O, NO, CH_4, C_2H_2, C_2H_4 and C_2H_6. The obtained values of k_{Q0} are

found to be in agreement with predictions based on an harpooned model.

In conclusion, the general understanding is that the cross section for the electronic quenching of $OH(A, v' = 0)$ does not vary significantly for temperature from 1900 K to 2300 K [76, 77]. There are theoretical indications [104], but yet no experimental verification, that Q and VET share the same temperature behaviour. If this were the case, the ratios

$$\frac{k_{1\to0}[T]}{k_{Q0}[T]}, \quad \frac{k_{1\to0}[T]}{k_{Q1}[T]}, \quad \frac{k_{Q0}[T]}{k_{Q1}[T]}, \tag{24}$$

would be constant as a function of temperature. Consequently, data obtained in this work at room temperature could be used to calculate ratios shown in Equation 24 at temperatures higher than 1900 K without introducing unbearable errors.

However, a thorough investigation of the temperature variation of k_Q, k_{Q1} and $k_{1\to0}$ in condition of complete rotational thermalization, and for a large set of collisional partners, is missing to date. This experimental data would be especially relevant in the context of applying LIF to the investigation of fast and important energy depositions occurring in nanosecond discharges. Indications that this is the case are reported in Chapter 3. For these reasons, a similar study as the one presented in this chapter will be performed at high temperature.

Ref.	k_{Q0} $[10^{-11} cm^3 s^{-1}]$	k_{Q1} $[10^{-11} cm^3 s^{-1}]$	$k_{1\to0}$ $[10^{-11} cm^3 s^{-1}]$	pumped level (v', N')	gas bath
this work	3.78 ± 0.08	27.0 ± 0.7	21.09 ± 0.26	(1, 1)	He 100 Torr
[118]	2.8 ± 1.2	23.6 ± 1.5	23.3 ± 2.2	(1, 2)	He 1 Torr
[107]	2.47			-	-
[17]		25 ± 4	28 ± 6	(1, 0)	no
[17]		12 ± 3	20 ± 6	(1, 4)	no
[16]	5.2 ± 1.1			(0, 0)	no
[16]	3.7 ± 0.4			(0, 1)	no
[16]	2.5 ± 0.4			(0, 2)	no
[16]	1.9 ± 0.4			(0, 3)	no

Table 4: Comparison of present results with literature data: N_2

Ref.	k_{Q0} $[10^{-11}\,cm^3\,s^{-1}]$	k_{Q1} $[10^{-11}\,cm^3\,s^{-1}]$	$k_{1\to0}$ $[10^{-11}\,cm^3\,s^{-1}]$	pumped level (v', N')	gas bath
this work	13.50 ± 0.27	24.15 ± 0.48	2.32 ± 0.07	(1, 1)	He 100 Torr
[118]	9.6 ± 1.2	20.6 ± 1.5	2.1 ± 0.2	(1, 2)	He 1 Torr
[119]	13.5 ± 0.9			(0, 2)	Ar 5 Torr
[16]	15.6 ± 0.6			(0, 0)	no
[16]	15.8 ± 1.9			(0, 1)	no
[16]	15.5 ± 0.4			(0, 2)	no
[16]	12.5 ± 0.5			(0, 3)	no

Table 5: Comparison of present results with literature data: O_2

Ref.	k_{Q0} $[10^{-11}\,cm^3\,s^{-1}]$	k_{Q1} $[10^{-11}\,cm^3\,s^{-1}]$	$k_{1\to0}$ $[10^{-11}\,cm^3\,s^{-1}]$	pumped level (v', N')	gas bath
this work	65.6 ± 1.3	60.6 ± 2.2	4.81 ± 0.28	(1, 1)	He 100 Torr
[118]			7.3 ± 0.7	(1, 2)	He 1 Torr
[119]	68.0 ± 6.1			(0, 2)	Ar 5 Torr
[17]		69 ± 3	-	(1, 0)	no
[17]		66 ± 7	-	(1, 2)	no
[17]		62 ± 8	<1.2	(1, 5)	no
[16]	79.0 ± 2.0			(0, 0)	no
[16]	78.9 ± 2.5			(0, 3)	no
[16]	69.8 ± 2.0			(0, 5)	no

Table 6: Comparison of present results with literature data: H_2O

Ref.	k_{Q0} $[10^{-11}\,cm^3\,s^{-1}]$	k_{Q1} $[10^{-11}\,cm^3\,s^{-1}]$	$k_{1\to0}$ $[10^{-11}\,cm^3\,s^{-1}]$	pumped level (v', N')	gas bath
this work	45.5 ± 1.1	61.4 ± 3.5	26.7 ± 0.7	(1, 1)	He 100 Torr
[119]	40.3 ± 2.8			(0, 2)	Ar 5 Torr
[17]		61 ± 2	31 ± 6	(1, 0)	no
[17]		38 ± 2	31 ± 9	(1, 4)	no
[16]	49.5 ± 1.9			(0, 0)	no
[16]	36.9 ± 1.2			(0, 3)	no
[16]	21.1 ± 1.2			(0, 5)	no

Table 7: Comparison of present results with literature data: CO_2

Ref.	k_{Q0} $\left[10^{-11}\,cm^3\,s^{-1}\right]$	k_{Q1} $\left[10^{-11}\,cm^3\,s^{-1}\right]$	$k_{1\to0}$ $\left[10^{-11}\,cm^3\,s^{-1}\right]$	pumped level (v', N')	gas bath
this work	38.9 ± 0.6	40.1 ± 1.5	7.09 ± 0.11	(1, 1)	He 100 Torr
[107]	34.92			-	-
[16]	38.3 ± 1.5			(0, 0)	no
[16]	21.3 ± 1.5			(0, 5)	no

Table 8: Comparison of present results with literature data: CO

coll	Ref.	k_{Q0} $[10^{-11}\,cm^3\,s^{-1}]$	k_{Q1} $[10^{-11}\,cm^3\,s^{-1}]$	$k_{1\to0}$ $[10^{-11}\,cm^3\,s^{-1}]$	pumped level (v', N')	gas bath
H_2	this work	20.8 ± 0.5	53.5 ± 1.8	23.05 ± 0.33	(1, 1)	He 100 Torr
	[107]	17.90			-	-
	[16]	21.9 ± 0.5			(0, 0)	no
	[16]	21.3 ± 0.9			(0, 1)	no
	[16]	17.0 ± 1.3			(0, 3)	no
	[16]	15.4 ± 0.9			(0, 4)	no
D_2	this work	14.89 ± 0.11	44.5 ± 1.2	21.88 ± 0.40	(1, 1)	He 100 Torr
	[16]	15.4 ± 1.2			(0, 0)	no
	[16]	8.3 ± 0.5			(0, 5)	no

Table 9: Comparison of present results with literature data: H_2 and D_2

Ref.	k_{Q0} $[10^{-11}\,cm^3\,s^{-1}]$	k_{Q1} $[10^{-11}\,cm^3\,s^{-1}]$	$k_{1\to0}$ $[10^{-11}\,cm^3\,s^{-1}]$	pumped level (v', N')	gas bath
this work	34.6 ± 0.5	71.3 ± 2.4	37.8 ± 0.6	(1, 1)	He 100 Torr
[107]	28.1			-	-
[17]		68 ± 7	44 ± 1.3	(1, 0)	no
[16]	31.0 ± 1.0			(0, 0)	no
[16]	25.0 ± 1.0			(0, 3)	no
[16]	23.0 ± 1.2			(0, 5)	no

Table 10: Comparison of present results with literature data: CH_4

coll	Ref.	k_{Q0}	k_{Q1}	$k_{1\to0}$	pumped level	gas bath
	$[10^{-11}\,cm^3\,s^{-1}]$	$[10^{-11}\,cm^3\,s^{-1}]$	$[10^{-11}\,cm^3\,s^{-1}]$	(v', N')		
C_2H_2	this work	82.7 ± 4.1	84 ± 10	3.90 ± 0.46	(1, 1)	He 100 Torr
	[16]	71.9 ± 1.5			(0, 0)	no
	[16]	64.2 ± 1.9			(0, 3)	no
	[16]	56.5 ± 1.3			(0, 5)	no
C_2H_4	this work	96 ± 6	77 ± 7	0.68 ± 0.49	(1, 1)	He 100 Torr
	[16]	69.1 ± 1.6			(0, 0)	no
	[16]	69.0 ± 1.1			(0, 3)	no
	[16]	67.6 ± 2.2			(0, 5)	no
C_2H_6	this work	74.9 ± 0.9	84.3 ± 3.5	23.30 ± 0.31	(1, 1)	He 100 Torr
	[16]	61.2 ± 1.8			(0, 0)	no
	[16]	58.8 ± 1.1			(0, 3)	no
	[16]	58.6 ± 0.7			(0, 5)	no

Table 11: Comparison of present results with literature data: C_2H_2, C_2H_4 and C_2H_6

3

INVESTIGATION OF NANOSECOND PULSED DISCHARGES BY LIF

ABSTRACT

Nanosecond repetitively pulsed (NRP) discharges used to dissociate CO_2 are harsh environments for the application of LIF. In fact, such systems are characterized by fast variations of gas composition, pressure and temperature. Additionally, when the discharge is operated with a fully molecular mixture, i.e. without the use of a noble gas bath, quenching rates are so fast to limit the use of LIF.

The use of LIF becomes challenging when rotational distributions are not thermalized and quenching rates can be faster than the characteristic decay frequency of the laser pulse. In this context, this chapter presents the main caveats to the use of LIF for the diagnostics of systems characterized by a overwhelming collisionality. A spectroscopic framework is provided to highlight how LIF measurable quantities are changed by the collisional environment.

The application of LIF to two different NRP discharge configurations is shown. Firstly, a CO_2/H_2O mixture is diluted in He to create a more favourable environment and demonstrate the absolute quantification of OH. Secondly, He is removed from the mixture and the discharge is run in a configuration relevant for practical applications. In the second case, the OH density cannot be measured anymore with laser pulses and detector time resolution in the ns time scale. Nevertheless, it is shown that, provided a proper knowledge of the collisional rate coefficients, a Collisional Energy Transfer LIF (CET–LIF) methodology is still applicable to deduce the gas composition from the analysis of LIF spectra.

3.1 INTRODUCTION

The conversion of CO_2 by non–thermal plasmas is gaining increasing interest due to a number of potential advantages:

- the possibility of driving endothermic reactions at room temperature is a big step towards high energy efficiency;
- the virtually absent switch–on inertia permits to follow the availability of electric energy from renewable sources;
- when a source of hydrogen is added, it is possible to perform the direct conversion of CO_2 to obtain light hydrocarbons. For example, common sources of hydrogen are H_2O [14], H_2 [23, 30, 43, 122], CH_4 [60, 93, 99, 111] or other hydrocarbons [123] as well.

These characteristics make non–thermal plasma a promising technology for the storage of electrical energy in chemical form. This is especially relevant when the intermittency of the availability of electric energy from renewable sources is to be mitigated. However, this technology is not mature enough and its utilization in the industry is still limited. A great deal of research is required to develop non–thermal plasma reactors that are attractive for industrial application on a large scale. In particular, research efforts are required to substantially increase the energy efficiency and to shift the selectivity towards the synthesis of value–added products.

A plethora of different reactor concepts, mostly working at atmospheric pressure, have been tested so far: dielectric barrier discharge [23, 60, 93, 99, 122], microwave flowing reactor [8, 14, 30, 35, 89], gliding arc [111] and corona [51, 123]. Not to mention the nanosecond pulsed discharges that are gaining increasing interest in the community. In fact, they permit fast and intense energy depositions, usually of the order of $10\,mJ\,pulse^{-1}$ for pulses of the duration of about $6\,ns$. Additionally, thanks to the construction geometry, the discharge region can be easily accessed by optical diagnostics.

Recently, a nanosecond repetitively pulsed discharge (NRP) has been tested for the processing of CO_2/CH_4 mixtures [91]. The investigation showed encouraging energy efficiency and selectivity towards syngas formation. The reactor was a first pilot and the discharge design was not optimized. Specifically, the discharge geometry was not designed so as to process the largest portion of the gas flow. Nevertheless, the obtained conversion efficiencies are among the highest found in the literature for any kind of discharge. Consequently, there are strong indications that the NRP might be a good candidate for the processing of CO_2 and CH_4 in the context of the electrification of the chemical industry.

The current approach for the investigation of non–thermal plasma reactors is multidisciplinary and includes:

- technological efforts devoted to discharge design and, eventually, to the development of heterogeneous catalysis systems;
- measurement of stable products in the effluent is performed by chemical analytical techniques such as chromatography, mass spectrometry and FTIR spectroscopy [79];
- reactor modelling including the set of reactions belonging to plasma–chemistry [101];
- critical comparison of experimental results to model predictions to improve the reactor design [99].

In order to investigate the chemical kinetics of the discharge, the experimental investigation needs to be performed by using time–resolved diagnostics. Such diagnostics allow the study of both transient and stable species. For the case of transient species, time–resolved diagnostics are essential because of the very short lifetime of the molecule, usually of the order of few µs. The study of stable species by means of time–resolved diagnostics is also relevant in the context of monitoring their kinetics. Such a knowledge is useful to understand the mechanism itself but also to optimize the discharge energy expenditure. In fact, build up effects can also be studied and tailored to maximize the overall efficiency of the process.

Nanosecond repetitively pulsed (NRP) discharges have been the subject of several investigations in the context of plasma assisted combustion during the last two decades. However, they have only been recently applied to the conversion of CO_2. The most recent investigations of a pin–to–pin NRP at atmospheric pressure [12, 52] depict a hostile environment for the use of LIF. When streamer like discharges are formed between the two electrodes, hot cores where the gas temperature can be higher than 2000 K have been observed. Very high temperature gradients induce extremely fast expansions in the tens of µs time scale. Fast cooling obtained though gas recirculation is also observed.

In the discharge, the gaseous mixture is subject to dramatic change of its physical characteristics like density and temperature. Additionally, the composition of the mixture changes rapidly. At first, dissociation is the result of the large amount of energy loaded in the system by the electric discharge. Afterwards, fast chemical reactions take place among the components of the original mixture, stable products of dissociation and a number of radicals.

In this inhomogeneous and fast changing scenario, it is not possible to determine a priori the effective Q and VET rates. However, an alternative way is represented by the determination of Q and VET rates by fitting the fluorescence spectrum and pulse [22], as shown in Chapter 2. The species composing the mixture need to be known, as well as their rate coefficients. With this information it is possible

to measure – with high temporal and spatial resolution – the concentration of each component of the mixture. Such a procedure was demonstrated in [20] for $He/air/H_2O$ and $Ar/air/H_2O$ mixtures. Additionally, the technique was also applied for measuring the penetration of air and H_2O in the effluent of an APPJ for plasma medicine applications [22, 63, 87]. As highlighted in Section 2.8, this method is efficient provided sharp variations in VET and Q exist among the different species composing the mixture. Section 3.3 discusses the applicability of this procedure to the specific case of $He/CO_2/H_2O$ and CO_2/H_2O mixtures treated by NRP.

A kinetic study of the gas composition is especially relevant when back reactions consume the desired products. For example, this is expected to be the case when CO_2 is dissociated in the presence of an hydrogen source for the direct synthesis of light hydrocarbons. In fact, if OH is formed in the discharge, it can react with the product of dissociation CO through the following reaction $CO + OH \rightarrow CO_2 + H$ with rate $k(400\,K) = 1.57 \times 10^{-13}\,cm^3\,s^{-1}$ [6]. It is clear how such reaction will lower the dissociation efficiency by consuming CO. Therefore, in order to maximize the efficiency of the process, the understanding of the kinetic of these mechanisms is required. Consequently, it is of a paramount importance to monitor the temporal evolution of both CO and its partners of reaction, as for example OH.

CO can be monitored in a time–resolved fashion by means of Two–photon Absorption Laser Induced Fluorescence (TALIF) [68]. However, a complete set of collisional rate constants that suffices for the quantification of CO by TALIF in a NRP is not available in the literature. An alternative way is to perform LIF on OH that is embedded in a mixture where CO plays the role of the collisional partner. The main advantage of using this approach is that both the OH and the CO concentrations can be measured simultaneously with the same diagnostics, see Section 2.8.

This chapter reports the experimental investigation of a NRP used for the dissociation of CO_2 when H_2O is used as hydrogen source. The experimental application of the rate coefficients presented in Chapter 2 is displayed. An incremental approach to the investigation is taken in order to demonstrate how the collisionality of the system defines the measurement. The two following scenarios are investigated:

- a mild NRP discharge is run in a mixture containing CO_2/H_2O in a He gas bath. Because of the large amount of He, all the three rates Q_{A0}, Q_{A1} and $R_{1\rightarrow0}$ can be measured. In this conditions LIF can be applied to quantify both OH and CO;
- the same reactor is used to process a mixture of CO_2/H_2O. Because of the high quenching frequency, only the ratio between the (0,0) and (1,1) bands of OH can be measured and LIF cannot be used for its quantification. Nevertheless, the CO concentration can be measured by using a Collision Energy Transfer

Laser Induced Fluorescence (CET–LIF) methodology. CET–LIF is conceptually different from the classical LIF since the molecule excited by the laser becomes the probe rather than the target.

3.2 EXPERIMENTAL SETUP

The LIF setup used for the study of collisional processes described in Chapter 2 is also used for the investigation of the NRP discharges, see Figure 13.

An oval quartz chamber with major dimensions of about 50 mm × 30 mm constitutes the reactor. Two parallel arms allows to shine the laser beam through the center of the reactor. The two arms are equipped with sapphire windows mounted at the Brewster angle for maximum transmittance of the UV beam. Similarly, LIF signals are collected from an orthogonal arm.

1 mm in diameter tapered tungsten rods constitute high voltage and ground electrodes. The high voltage electrode is covered by a quartz cylinder with 2 mm inner diameter. The use of the quartz cylinder helps in confining the gas flow around the electrode. A dielectric layer is also used in some configuration to obtain a more diffused discharge, more on this in the next Section 3.3. When that is the case, the grounded electrode is covered with 8 mm diameter Macor rod with a thickness of 1.5 mm.

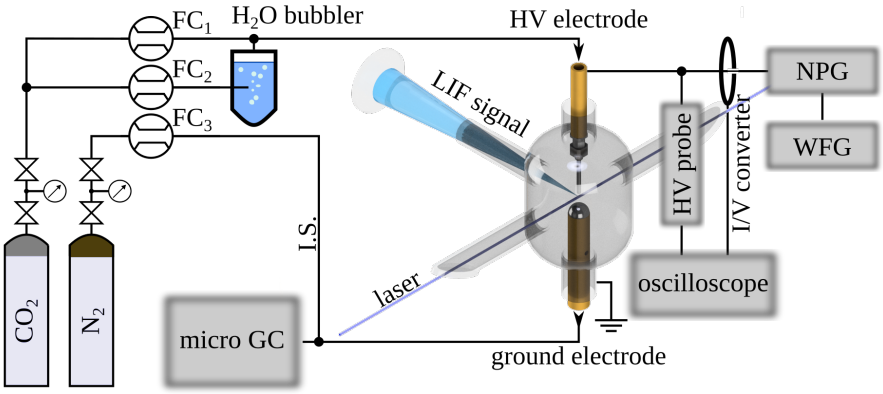

Figure 13: Schematics of the experimental setup. The laser and the gas system are the same as those described in Chapter 2. The reactor is an egg–shaped quartz cell with three perpendicular arms. LIF signal is collected perpendicularly to the laser beam. The nanosecond pulse generator (NPG) generate the discharge between the two electrodes. A waveform generator (WFG) is used to trigger the NRP. Voltage and current are measured at the high voltage electrode by means of the HV probe and the I/V converter, respectively. The gas chromatographer (micro GC) is used for the effluent analysis (data are not reported in this work).

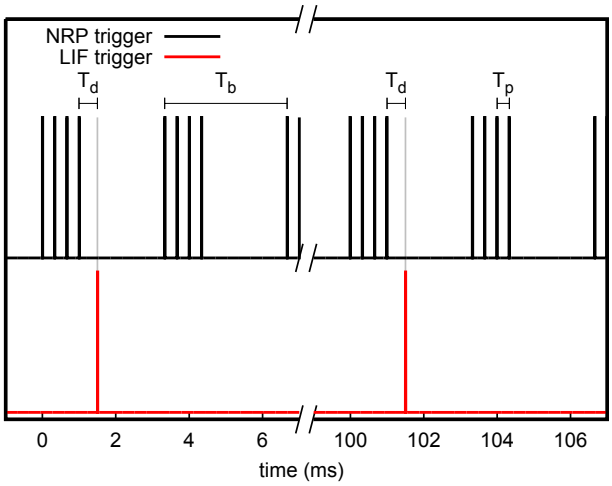

Figure 14: Temporal pattern of the signal driving the high voltage generator. Each pulse has a voltage of about 2×10^4 V and temporal width of 6 ns. The discharge is ignited at the first pulse of each burst and sustained within the burst. The LIF trigger can be conveniently shifted in time to probe the discharge at different times after the burst.

The discharge is driven by a Megaimpulse NPG 18/3500 high voltage (HV) pulse generator. The HV pulse generator is triggered by a waveform generator. A particular voltage pattern is chosen, see Figure 14. It contains bursts repeated at a frequency of 10 Hz and each burst is composed by 10 pulses repeated at a frequency of 3 kHz. This is the fastest repetition rate achievable with the HV generator. Bursts are repeated at a frequency of 10 Hz that is the maximum operating frequency of the laser. A continuous 3 kHz pattern would not give any advantage from a spectroscopic point of view. Moreover, the electrodes would be damaged at a higher pace. It is worth remembering that the goal of this study is to show the applicability of LIF on a NRP discharge and not to assess the reactor overall performance. Consequently, the discharge repetition rate is lowered to the laser frequency.

The laser is triggered by the waveform generator and the laser pulse can be conveniently delayed to probe the discharge at different times. This is necessary for the assessment of possible build–up effects between subsequent pulses. Specifically, this means that subsequent discharge events would increase the local dissociation rate by interacting with the same volume of gas. However, such an effect has not been observed. All the data presented in this chapter has been obtained by probing the discharge at the end of the burst.

Discharge current (I) and voltage (V) are measured by a Magnelab CT-D-1.0 I/V converter (Band width = 500 MHz) and a Tektronics P6015A probe (Band width = 75 MHz), respectively. V/I traces are

recorded by a LeCroy HDO9104 digital oscilloscope to calculate the energy deposited by the discharge.

3.3 QUANTIFICATION OF OH BY LIF

This section illustrates the use of LIF in a nanosecond repetitively pulsed discharge. The challenges posed by such a collisional environment are demanding. Therefore, the reactor is operated in three different configurations of increasing severity:

- the NRP is first run with a $He/CO_2/H_2O$ mixture. The dielectric cap is used to cover the ground electrode. In this configuration the discharge volume is large and fills a cone extending from the HV electrode to the dielectric layer. Such a large and homogeneous discharge region can be easily probed by LIF. Moreover, the large amount of He lowers the total quenching rate of the mixture allowing for the measurement of both LIF pulses and spectra.
- the NRP is run on the same $He/CO_2/H_2O$ mixture but now with naked electrodes. A cylindrical discharge is formed in between of the HV electrode and the ground one. The discharge region is large and homogeneous enough to be probed by LIF. Still, the large amount of He allows for the measurement of both LIF pulses and spectra.
- the NRP is run on a CO_2/H_2O mixture with naked electrodes. The removal of He dramatically influences the characteristics of the discharge that becomes filamentary. In this configuration, the effective quenching rate is so large that only LIF spectra can be measured.

These three discharge configurations are conveniently chosen to have different collisionality and used as testbench for LIF and CET–LIF. Pictures are shown in Figure 15 to highlight the striking differences between the three discharge configurations. He is introduced in the mixture to mitigate the strong quenching of both CO_2 and H_2O on the OH excited state. It is worth remembering that the major molecular species found in a CO_2/H_2O discharge have very large rate coefficients, see Table 12. From a kinetic point of view, the benefits of using He as gas bath are two:

- the rate coefficient for electronic quenching by He is about $4 \times 10^{-14}\,cm^3\,s^{-1}$ [22]. It is at least three orders of magnitude lower that of the molecules present in the mixture. Consequently, the effective quenching coefficient of the mixture is strongly decreased by the use of He. This is necessary to fulfil the condition of Equation 31. In the end, if such condition is met, Q_{A0}, Q_{A1} and $R_{1\to0}$ can be measured and therefore OH can be quantified;

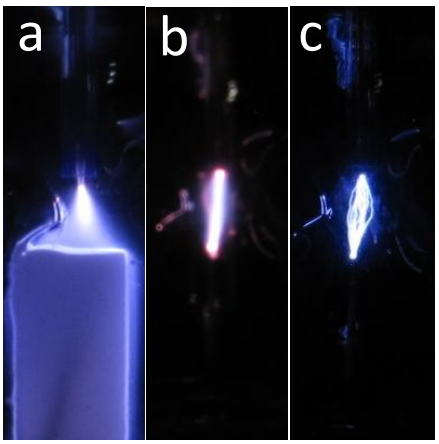

Figure 15: Pictures of a) NRP–DBD in $He/CO_2/H_2O$ with the dielectric cap mounted on the ground electrode, b) NRP in $He/CO_2/H_2O$ and c) NRP in CO_2/H_2O. The camera exposure is set so as to capture an entire burst.

- He has very fast RET coefficient, therefore it is an effective medium to thermalize the rotational population, see Section 2.4.1. Consequently, the use of He ensures rotational thermalization of both A_0 and A_1. As a result, data obtained in condition of complete thermalization can be unambiguously used for the investigation of the discharge.

Collisional partner	k_{Q0} $[10^{-11}cm^3\,s^{-1}]$	k_{Q1} $[10^{-11}cm^3\,s^{-1}]$	$k_{1\to0}$ $[10^{-11}cm^3\,s^{-1}]$
O_2	13.50 ± 0.27	24.15 ± 0.48	2.32 ± 0.07
H_2O	65.6 ± 1.3	60.6 ± 2.2	4.81 ± 0.28
CO_2	45.5 ± 1.1	61.4 ± 3.5	26.7 ± 0.7
CO	38.9 ± 0.6	40.1 ± 1.5	7.09 ± 0.11

Table 12: Rate coefficients of total quenching k_{Q0} and k_{Q1} of the two vibrational states A_0 and A_1, respectively, and vibrational relaxation $k_{1\to0}$. Data relevant for a CO_2/H_{20} discharge are taken from the results of Chapter 2

The fact that He decreases the quenching rate of the mixture is of paramount importance. Indeed, the effective quenching rate of the mixture defines whether the condition of Equation 31 is met or not. If the condition is met, LIF pulses can be measured and fitted to yield

values of Q_{A0} and Q_{A1}. The effective quenching rates and vibrational energy transfer of the mixture are defined as:

$$Q_{A0}^{eff} = n_{tot} \sum_i k_{Q0}^i \chi_i = n_{tot} k_{Q0}^{eff}, \tag{25}$$

$$Q_{A1}^{eff} = n_{tot} \sum_i k_{Q1}^i \chi_i = n_{tot} k_{Q1}^{eff}, \tag{26}$$

$$R_{1\to0}^{eff} = n_{tot} \sum_i k_{1\to0}^i \chi_i = n_{tot} k_{1\to0}^{eff}. \tag{27}$$

where n_{tot} is the total number density, the sum runs over the collisional partners composing the mixture, k_{Q0}^i, k_{Q1}^i and $k_{1\to0}^i$ are the rate coefficients of each species and χ_i is the molar fraction of the i–esim species.

For the case of pure CO_2 at atmospheric pressure, the quenching rate is calculated to be $1.5 \times 10^{10}\,s^{-1}$ by using values reported in Table 12. Consequently, in those conditions, a LIF measurement based on the analysis of the time–resolved signals requires the temporal width of the laser pulse to be in the ps domain. To this aim, ps tunable lasers and fast detectors would have to be used. Conversely, if $Q_{A1}^{eff}, Q_{A0}^{eff}$ are slow enough as compared τ_l^{-1}, the 5–level model can be fitted to the data. When the discharge is run on the He containing mixtures, the partial pressure of CO_2 is kept low enough to permit the use of a laser with ns long pulses.

3.3.1 *He/CO_2/H_2O discharges*

The reactor is operated with the following gas mixture:

$$\text{He} + 4\,\text{Torr}\ CO_2 + 0.75\,\text{Torr}\ H_2O,$$

with the total pressure set to 760 Torr, He is by far the largest component in the mixture.

Fluorescence spectra obtained with the discharge operated either with and without the dielectric cap are shown in Figure 16. Both (0,0) and (1,1) bands can be fitted by using thermalized rotational distribution at $T_r = 330\,K$. Spectra obtained with the naked electrodes (NRP discharge) and with the ground electrode covered in Macor (NRP–DBD discharge) cannot be distinguished. This suggests that the conspicuous He bath defines the shape of the spectra by assuring complete rotational thermalization of both A_0 and A_1 states.

In addition to the fluorescence spectra, LIF time–resolved pulses can be measured as well for both discharge configurations. Consequently, the 5–level model presented in Chapter 2 can be fitted to LIF spectra and pulses. Since the apparatus is calibrated, and the rate coefficients for CO_2, CO and H_2O are known, the concentration of OH can be measured quantitatively.

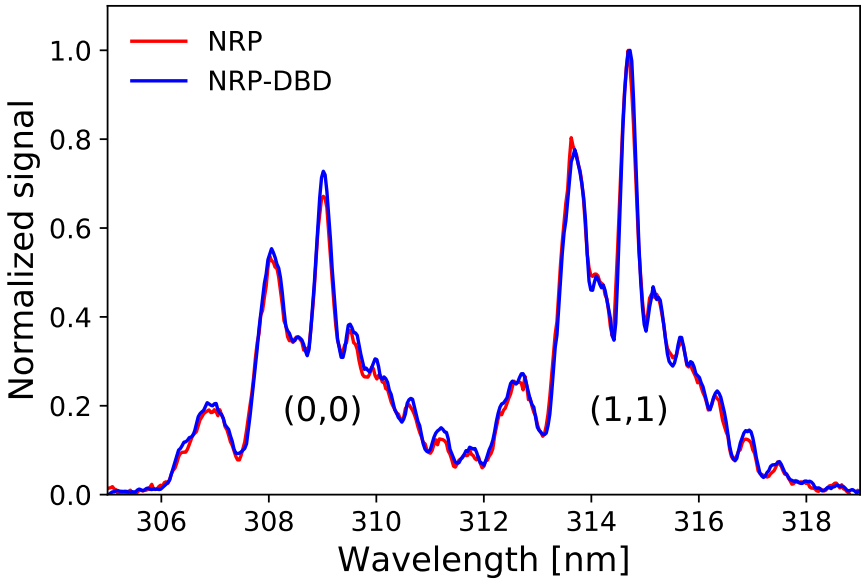

Figure 16: Fluorescence spectra obtained in the mixture He + 4 Torr CO_2 + 0.75 Torr H_2O. Both the discharges are operated at 5.7 mJ pulse^{-1} Spectra are measured after the first voltage pulse in the burst, see Figure 14. Rotational distribution can be fitted to a Boltzmann distribution with $T_r = 330$ K.

The temporal evolution of the OH concentration is reported in Figure 17 for both NRP and NRP–DBD discharges. The traces could be fitted by using a double exponential function. At this stage of research, there is no strong understanding of the mechanisms behind this temporal decay. A more thorough investigation is planned to cast light on the causes of such OH consumption – may they be related to chemical reactions or fluid dynamics. Nevertheless, a preliminary fit with a double exponential function allows at least to obtain the time constant of the decay. These time constants will prove to be useful to discriminate among the possible reactions involving OH and CO.

Time constants for the discharged operated either with or without the dielectric cap are 14 µs and 5 µs, respectively. Therefore, the removal of the dielectric cap changes the kinetics of the discharge.

The CO_2 dissociation is indirectly measured from variations in the band ratio, as compared to a case with pure CO_2. More details about this methodology will be given in the next Section 3.5. Dissociation equal to 14% and 5% at 2 µs and 200 µs, respectively, are obtained for the NRP–DBD discharge. Similarly, when operated without the dielectric cap, the dissociation is about 10% at 2 µs. Because of the limited sensitivity of the diagnostics, see Figure 21, these values are close to the detection limit and they should only be considered as indicative.

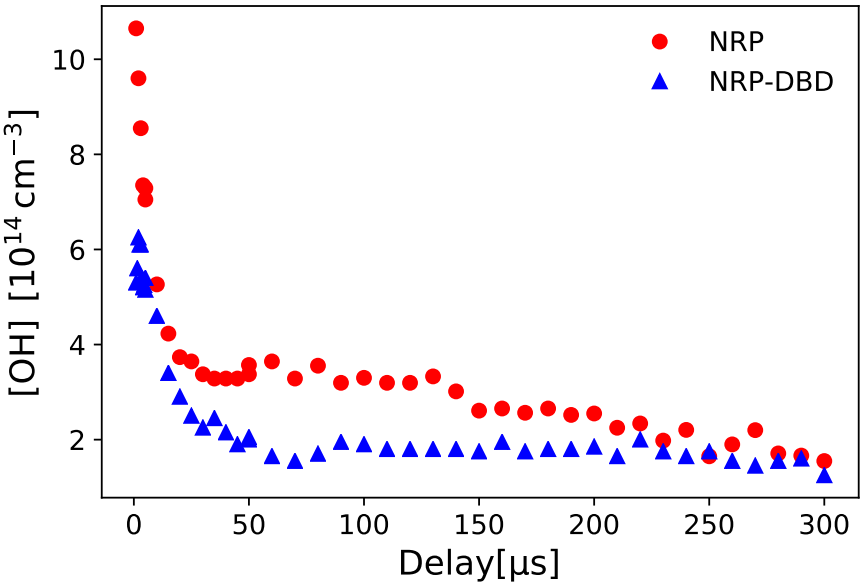

Figure 17: Temporal profiles of the OH concentration as measured at different delays after a discharge burst. For both cases the energy of the discharge is equal to 4.1 mJ $pulse^{-1}$. The mixture is composed by helium + 4 Torr CO_2 + 0.75 Torr H_2O at 760 Torr.

Having knowledge of the amount of CO present in the discharge is of interest to describe the OH kinetics. In fact, the major reactions involving OH, and relevant for this system, are:

$$OH + OH \rightarrow H_2O + O \quad k(300\,K) = 2.5 \times 10^{-12}\,cm^3\,s^{-1} \tag{28}$$

$$OH + CO \rightarrow COOH \quad k(300\,K) = 1.5 \times 10^{-12}\,cm^3\,s^{-1} \tag{29}$$

$$OH + CO \rightarrow CO_2 + H \quad k(400\,K) = 1.57 \times 10^{-13}\,cm^3\,s^{-1} \tag{30}$$

additional reactions involving atomic oxygen and hydrogen are at least three orders of magnitude slower. Moreover, the CO_2 dissociation after 2 µs is about 14%. Consequently, the CO concentration is of the order of $2 \times 10^{16}\,cm^{-3}$, compared to a OH concentration that is about 20 times smaller, see Figure 17. It would therefore be the reaction shown in Equation 29 that dominates. However, the corresponding time constant for the OH decay would be 37 µs, definitely larger than the measured 14 µs. This simple argument clearly does not suffice in describing the complicated chemistry of OH. Nevertheless, it shows that the aforementioned set of reactions – involving the major species in the discharge – are not sufficient to describe such a fast decay. Given the small OH concentration, these preliminary results do not support an important role of OH in CO back reactions at these experimental conditions.

3.4 LIF IN CONDITION OF PARTIAL ROTATIONAL THERMALIZATION

The previous section showed the investigation of discharges with CO_2/H_2O mixture diluted in He. That investigation is particularly relevant for the experimental testing of models because the He kinetic is well known. Additionally, since both dissociation products and OH can be quantified, general predictions about OH influence in the CO_2 dissociation can be tested [100]. However, the use of noble gas mixtures is not appealing from an industrial point of view. Consequently, in order to assess the performance of the NRP discharge for an industrially relevant scenario, a pure CO_2 – with small addition of H_2O – discharge has been investigated.

When the discharge is run without He as gas bath, Q^{eff}_{A0} and Q^{eff}_{A1} are faster than τ_l^{-1}. Hence, LIF pulses do no yield any meaningful information about the physics of the system. However, LIF spectra are still valuable. In fact, LIF spectra are time–integrated on the iCCD and therefore no demanding time resolution is required in this case, neither concerning the laser nor the detector. At these conditions, CET–LIF is applicable to measure the CO_2 dissociation.

It is found that spectra measured either with or without the discharge, but on a molecular mixture with the same composition, can be described by very similar rotational distributions. Consequently, a preliminary investigation on a gas cell is performed so as to simulate the non–thermal conditions found in the discharge.

At this point, it is worth remembering that the CET–LIF methodology is based upon the calculation of the ratio between the populations of the A_0 and A_1 states. Such quantity is proportional to the ratio between $k_{1\to0}$ and k_{Q0}. It does not depend upon the total pressure of the mixture, but only on its composition. For this reason, it is possible to compare measurements performed in the cell at 8 Torr with those performed in the discharge at 760 Torr. Moreover, this asset is extremely important when the methodology is applied to the investigation of the CO temporal profile in the discharge. In fact, such profile can be calculated although the temperature, and therefore the local density, varies in time after the discharge event.

This section presents measurements performed in the quartz cell with the goal of investigating:

- the effect that different collisional partners have in defining the rotational distributions of A_0 and A_1;
- the effect of exciting different rotational states.

Figure 18 shows spectra obtained with 8 Torr of CO or CH_4 as collisional partners. In both cases the laser was tuned to the $P_1(4)$ excitation line at 283.945 nm. As highlighted by the histograms, the rotational distribution of the A_1 level is highly non–thermal. It has

memory of the nascent population obtained after excitation of the $J' = 3.5$ level. The population of the A_1 state varies as a function of the collisional partner, has already reported in [17]. By comparing the effect of CH_4 and CO in shaping the population of the A_1, it can be noticed that the former tends to populate J higher than the excited one, while the latter does the vice versa.

Surprisingly enough, as a first approximation the Boltzmann distribution suffices to describe the population of the A_0 for both CH_4 and CO. However, the rotational temperatures of such distributions are much higher than that of the gas: 600 K for the case of CH_4 and 1500 K for CO. Similar behaviour has been observed by Copeland with N_2 as collisional partner [17]. Rotational equilibrium is not achieved between the the A_0 state and the gas bath, for both collisional partners. Additionally, it can be also noticed how the A_0 state is much more populated when CH_4 is used as collisional partner. This can be explained by looking at the values of $k_{1\to0}$ and k_{Q0}. Indeed, the ratio $k_{1\to0}/k_{Q0}$ is equal to 0.18 and 1.09 for CO and CH_4, respectively.

Figure 19 shows details of the rotational distribution of OH $A^2\Sigma^+$ $(v' = 1)$ when CH_4 is the collisional partner. Experimental and simulated spectra are displayed in Figure 19a. It is noticeable that the experimental spectrum is a mix between a thermal one obtained at 300 K and a nascent spectrum. This indicates that rotational relaxation occurs only partially during the average lifetime of the excited state, i.e. $k_{AR} \simeq k_{Q1}$. The memory effect in the rotational population can be appreciated by looking at Figure 19b. Such histogram shows the difference between the rotational population used to describe the experimental spectrum reported in Figure 19a and a thermal distribution simulated at 300 K. Rotational levels lower than the excited one are underpopulated. Conversely, from the pumped $J' = 3.5$ level further, rotational levels are overpopulated.

The possible J dependence of the vibrational energy transfer has been investigated by exciting rotational levels from $J = 0.5$ to $J = 4.5$. CO is used as collisional partner and the two sample spectra are shown in Figure 18a. By analysing the spectra it is possible to conclude that the excitation of different rotational states:

- varies appreciably the non–thermal distribution of A_1;
- does not influence the shape of the (0,0) – at this spectral resolution;
- does not appreciably change the band ratio.

The fact that the A_1 rotational distribution changes accordingly with the excitation of different lines is expected. Given the fast Q_{A1} – Q_{A1} in 8 Torr of CO is equal to $10^8\ s^{-1}$ – the system has no time to undergo complete relaxation to the thermal distribution. These spectra can be considered as snapshots of a rotational distribution that

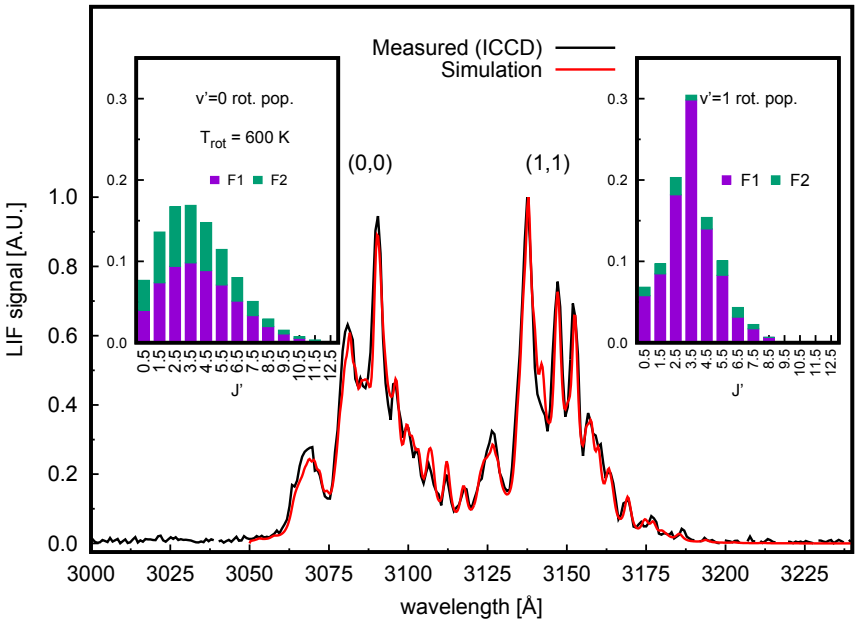

(a) Spectrum obtained in 8 Torr of CH_4 and about 0.1 Torr of H_2O+H_2O_2.

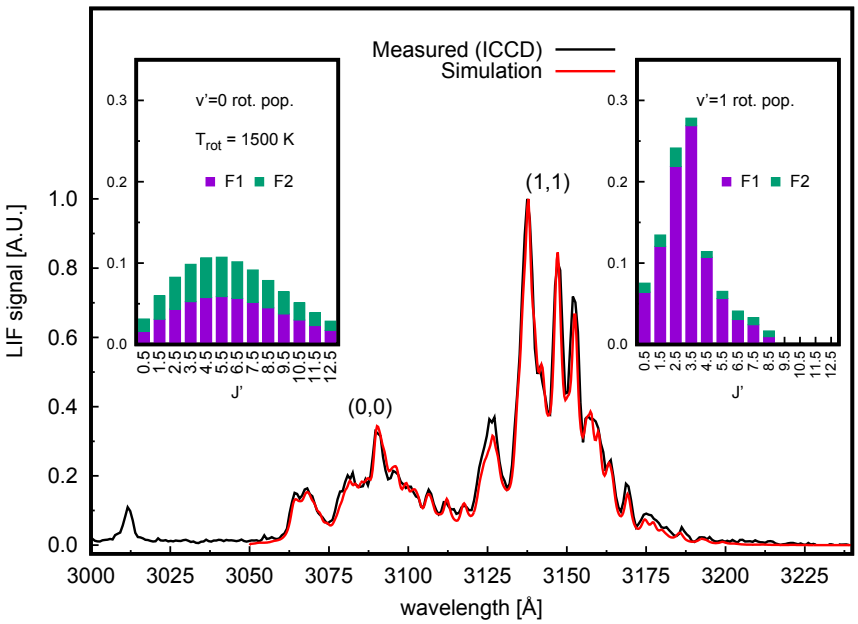

(b) Spectrum obtained in 8 Torr of CO and about 0.1 Torr of H_2O+H_2O_2.

Figure 18: Fluorescence spectra of OH after excitation of the $P_1(4)$ rotational line at 283.465 nm. Measurements are performed in a quartz cell at $T_{gas} \simeq 300$ K with no discharge. Simulations are performed by using LIFBASE Spectroscopy Tool [55] with an experimental resolution set to 0.2 nm. Histograms show the rotational distributions of both A_0 and A_1. The distribution of A_0 can be described by a Boltzmann distribution with $T_r \gg T_{gas}$. The distribution of A_1 is highly non–thermal and has memory of the excited line.

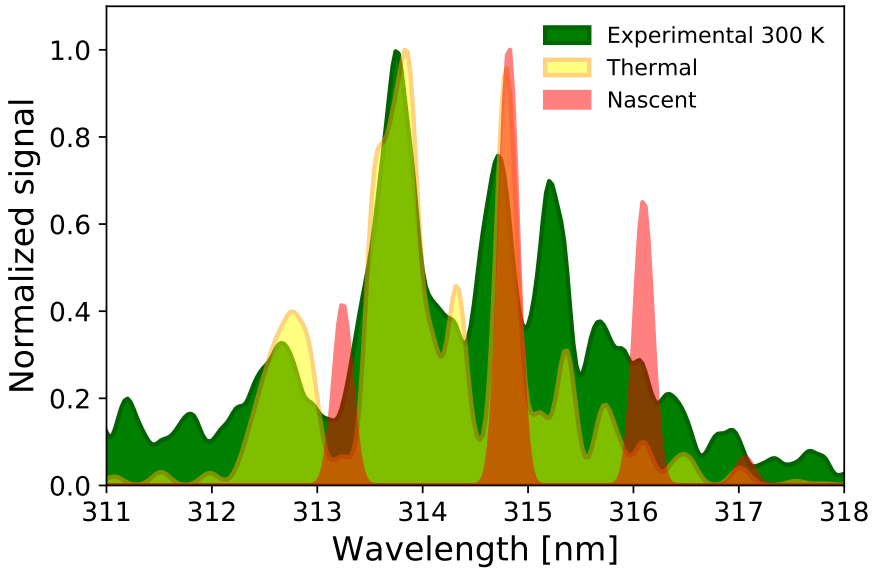

(a) Spectra of the (1,1) vibrational band. Nascent spectrum is simulated in condition of absent rotational relaxation. The thermal spectrum is simulated at 300 K.

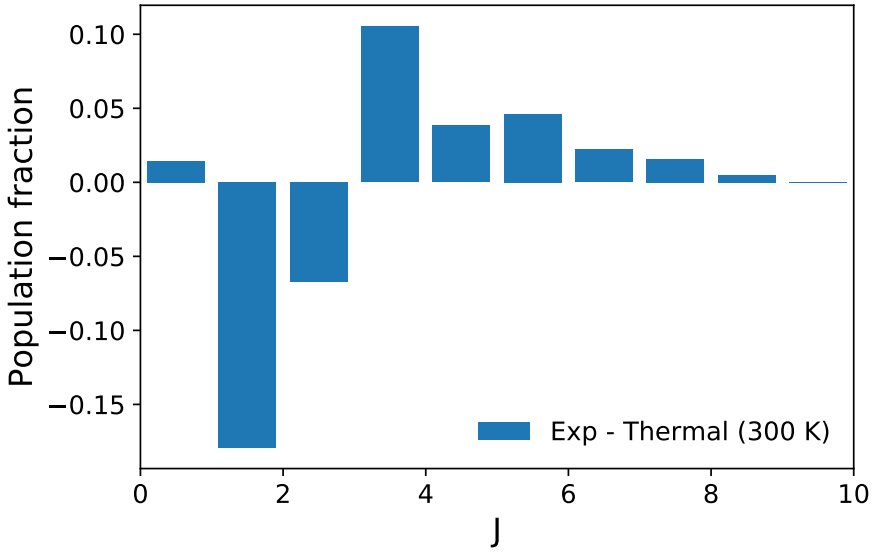

(b) Difference between the population distribution used to fit the experimental spectrum and the thermal one.

Figure 19: Fluorescence spectra and population distribution to compare the experimental results with simulations. The experimental data is obtained in 8 Torr of CH_4 and about 0.1 Torr of H_2O+H_2O_2 at 300 K in the cell. Both experimental and nascent spectra are obtained after excitation of the $P_1(4)$ line.

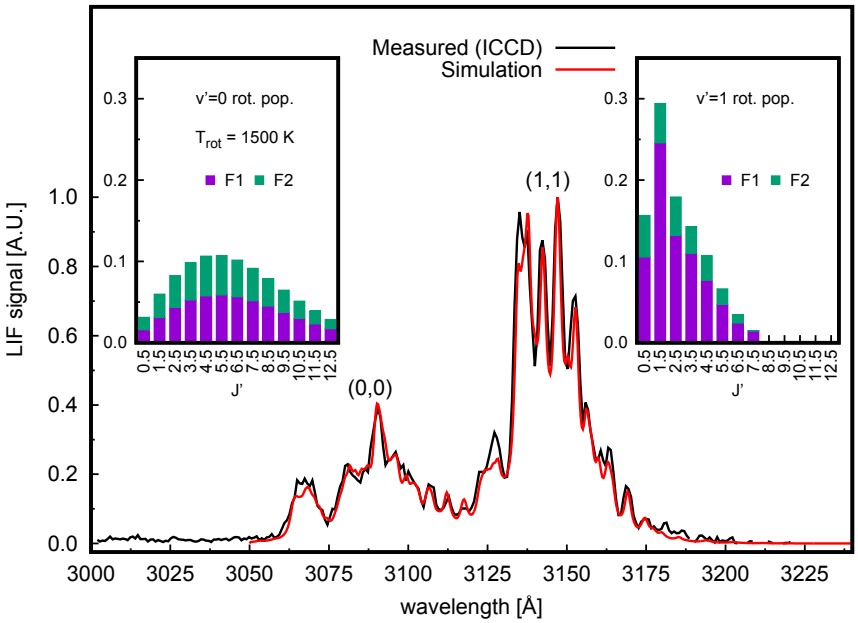

(a) Spectrum obtained after excitation of the $P_1(2)$ line at 282.580 nm.

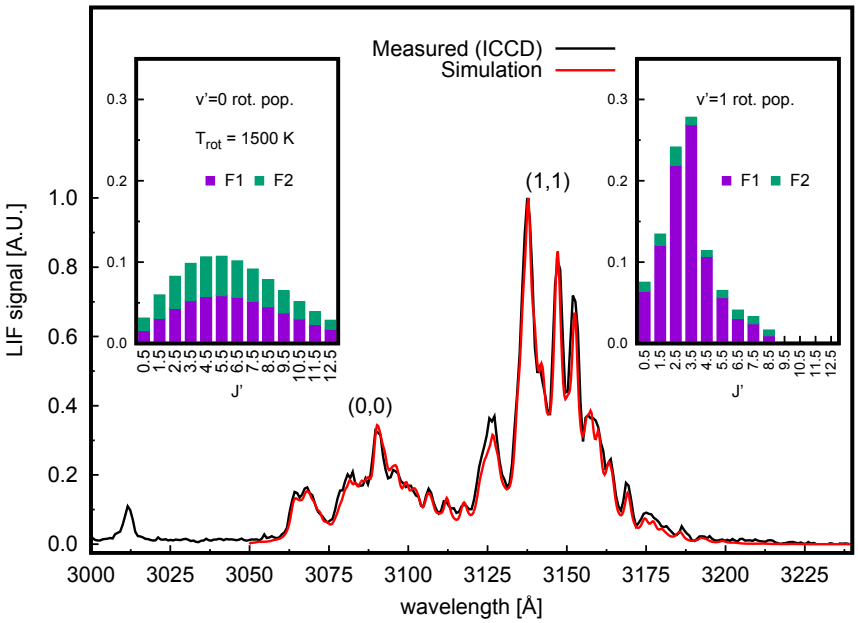

(b) Spectrum obtained after excitation of the $P_1(4)$ line at 283.463 nm.

Figure 20: Fluorescence spectra obtained in 8 Torr of CO and about 0.1 Torr of H_2O+H_2O_2 by excitation of the $P_1(2)$ and $P_1(4)$ lines. Measurements are performed in a quartz cell at $T_{gas} \simeq 300$ K with no discharge. Spectra are fitted by using spectroscopic data taken from LIFBASE Spectroscopy Tool [55] with an experimental resolution set to 0.2 nm. Histograms show the rotational distributions of both A_0 and A_1. The distribution of A_0 can be described by a Boltzmann–like distribution with $T_r \gg T_{gas}$. The distribution of A_1 is highly non–thermal and has memory of the excited line.

is undergoing thermalization. Therefore, such spectra show features characteristic of the nascent population. Conversely, with this experimental resolution, the shape of the (0,0) band does not appear to change appreciable when different rotational levels are excited.

At this stage of investigation, the following statements can be made:

i) $Q_{A0} = Q_{A0}(N')$. This has been experimentally verified in [16] by selective line excitation of the A_0 state;

ii) $R_{1\to0}/Q_{A0}$ does not change appreciably when different N' are excited in A_1;

iii) the A_1 rotational distribution is non–thermal and has memory of the excited N';

iv) the A_0 rotational distribution looks Boltzmann–like, as a first approximation, no matter which N' is excited in A_1;

v) the rotational population of A_0 extends beyond that of A_1.

Chapter 2 showed how to solve the simplified system of equations – valid after the excitation pulse has ceased to exist – to obtain the populations of both the A_0 and A_1 states. It is to remember that the simplified system of two equations is meaningful only provided laser excitation and fluorescence decay can be separated in time. If that is not the case, the system cannot be simplified and the full set of five differential equations is to be solved. The boundary is defined by the characteristic decay frequency of the laser pulse τ_l^{-1} – for this specific laser equal to $1.7 \times 10^8\ s^{-1}$ – and the quenching frequency due to the collisional partner. Hence, collisional partner concentration should be low enough to ensure

$$\tau_l^{-1} \gg Q_{A0}, Q_{A1}. \tag{31}$$

When applicable, the simplified system of two equations can be analytically solved to obtain an expression for the time–integrated populations of the A_0 and A_1 states. These quantities, apart from constants accounting for the collection efficiency of the system and the Einstein emission coefficients, correspond to the area of the spectra measured by the iCCD. Since in this case the condition of rotational thermalization cannot be given for granted, each spectroscopic quantity should now be regarded as J dependent. The population of a J level in the A_0 state should then be written as:

$$N^J_{A0} \propto \left.\frac{k_{1\to0}}{k_{Q0}k_{Q1}}\right|_J. \tag{32}$$

Although the data reported in this section appears to be reliable, this study should be considered as preliminary. In order to verify the conclusions drawn upon this data, a more thorough investigation

will be performed at a higher spectral resolution and for a larger set of collisional partners.

3.5 MONITORING CO BY CET-LIF IN A COLLISIONAL ENVIRONMENT

The analysis of LIF spectra is based upon the theory highlighted in Section 2.4.1. Upon their acquisition on the camera, spectra can be fitted with a convenient rotational population and the band ratio can be calculated. It is worth noting that the simplified system of two differential equations is not applicable in this regime. Hence, it is not possible to equate the band ratio with the ratio between $R_{1\to0}$ and Q_{A0}. However, the band ratio is still function of the ratio between $R^{eff}_{1\to0}$ and Q^{eff}_{A0} since these are the processes that populate and depopulate the A_0 state, see Equation 32,

$$\left.\frac{N_{A0}[t]}{N_{A1}[t]}\right|_{\tau_l^{-1}\leqslant Q^{eff}_{A0},Q^{eff}_{A1}} = \mathcal{F}\left[\frac{k^{eff}_{1\to0}}{k^{eff}_{Q0}}\right]. \tag{33}$$

In this regime the exact relation between the population ratio and $k^{eff}_{1\to0}$ and k^{eff}_{Q0} is not known. However, the the 5–level model can still be numerically solved. The following procedure has been followed:

- a synthetic spectrum is fitted to the experimental one by multiplying each line for the specific Einstein emission coefficient and the rotational population fraction. Line shapes take into account pressure, Doppler and instrumental broadening. The rotational distributions of the (0,0) band is imposed to be Boltzmann while that of the (1,1) one is left unrestricted. Fixing one distribution to be Boltzmann is necessary to deconvolve the signal in the central region where the two bands overlap;
- the 5–level model is run with the synthetic spectra and the rate coefficients measured in condition of complete thermalization. The output is the gas composition and therefore the CO_2 dissociation.

By fitting the A_0 and A_1 populations to the experimental spectrum it is possible to appreciate variation in the composition of the mixture, provided $k^i_{1\to0}$ and k^i_{Q0} change among the different species. To this end, it is worth investigating the case of CO_2 dissociation.

For the specific case of a CO_2/H_2O mixture treated in a NRP discharge, the following simplified reaction for CO_2 dissociation [105] is considered:

$$CO_2 \to CO + \frac{1}{2}O_2 \tag{34}$$

Consequently, after a discharge event, the collisional partners present in the mixture are CO_2, CO, O_2 and H_2O. For this specific mixture, an expression for the ratio between $k^{eff}_{1\to0}$ and k^{eff}_{Q0} can be written as:

$$\frac{k^{eff}_{1\to0}}{k^{eff}_{Q0}} = \frac{\left(k^{CO_2}_{1\to0}(1-\alpha)+k^{CO}_{1\to0}\alpha+k^{O_2}_{1\to0}\alpha/2\right)\chi_{CO_2}+k^{H2O}_{1\to0}(1-\chi_{CO_2})}{\left(Q^{CO_2}_{A0}(1-\alpha)+Q^{CO}_{A0}\alpha+Q^{O_2}_{A0}\alpha/2\right)\chi_{CO_2}+Q^{H2O}_{A0}(1-\chi_{CO_2})} \quad (35)$$

where χ_{CO_2} is the CO_2 molar fraction of the initial mixture and α is the dissociation rate defined from the following formula:

$$CO_2 \to (1-\alpha)CO_2 + \alpha CO + O_2\alpha/2. \quad (36)$$

Since CO_2 has the largest $k_{1\to0}/k_{Q0}$ ratio among the four species composing the mixture:

$$\left.\frac{k_{1\to0}}{k_{Q0}}\right|_{CO_2} > \left.\frac{k_{1\to0}}{k_{Q0}}\right|_{CO,O_2,H_2O}. \quad (37)$$

Hence, $k^{eff}_{1\to0}/k^{eff}_{Q0}$ in Equation 35 decreases as the dissociation increases. It is calculated for two mixtures, either with or without H_2O, and plotted in Figure 21. The relation between the measured band ratio and the dissociation α is monotonous. Therefore, the dissociation α can be unambiguously calculated from a measurement of $R^{eff}_{1\to0}/Q^{eff}_{A0}$, provided the rate of the collisional partners are known.

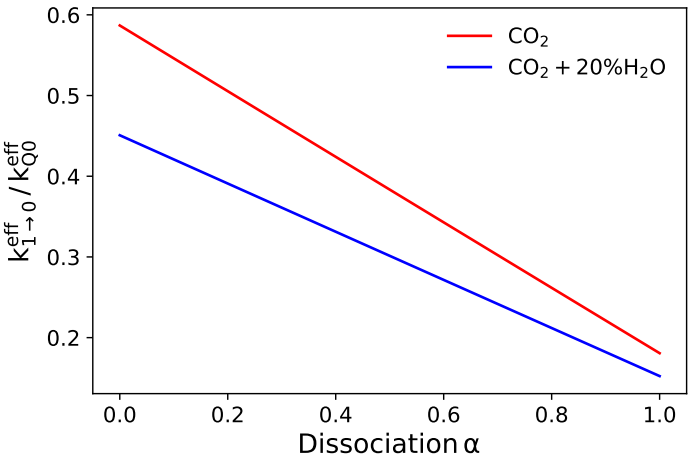

Figure 21: Plots showing how $k^{eff}_{1\to0}/k^{eff}_{Q0}$, calculated by means of Equation 35, varies as a function of the CO_2 dissociation. Two curves are plotted for a mixture of pure CO_2 and one containing 20% of H_2O, as to show the contribution of H_2O in lowering the sensitivity of the diagnostics. The contribution of He to k_{Q0} and $k_{1\to0}$ is neglected.

The main disadvantage of using this methodology is the low sensitivity. In fact, the ratio $R^{eff}_{1\to0}/Q^{eff}_{A0}$ changes slightly as a function of the dissociation rate. Therefore, small variations in the dissociation

are difficult to appreciate in the spectra. For example, when the dissociation varies from 5% to 20% the variation in the band ratio changes only by 10%. Hence, spectra need to be reliably measured and fitted if small variations in α are to be measured.

3.5.1 *CO_2/H_2O discharge*

This section presents the CET–LIF study of a CO_2 discharge with the addition of 1% H_2O. The discharge is operated at 735 Torr. At this CO_2 concentration, LIF pulses cannot be acquired since Q_{A0}, $Q_{A1} \gg \tau_l^{-1}$. Hence, the only observable is the fluorescence spectrum, from which, by applying Equation 35, it possible to calculate the conversion.

Two sample spectra are shown in Figure 22 as measured at different delay after the last pulse composing a discharge burst. The main observable feature is the increase in the band ratio as the delay increases. Because of Equation 37, the increase in the band ratio can be directly related to an increase in the CO_2 concentration.

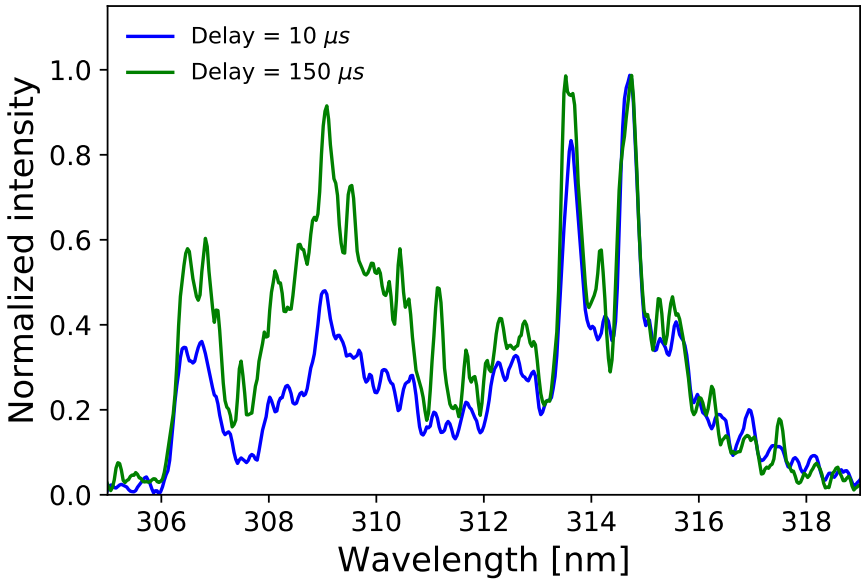

Figure 22: Fluorescence spectra in the CO_2 NRP, at two delays after the discharge burst. The mixture is CO_2 + 1%H_2O at 735 Torr. The energy of the discharge is equal to 2.9 $mJ\,pulse^{-1}$. Spectra are obtained after excitation of the $Q_2(3)$ line.

The procedure explained in the previous section, based upon the use of the 5–level model in conjunction with the fit of the fluorescence spectra, is applied to calculation of the conversion. Values are shown in Figure 23. Measurements performed at few µs after the discharge event show remarkable conversion of about 80%. A steady decay of the conversion is observed, with final values close to 20% measured at about 150 µs.

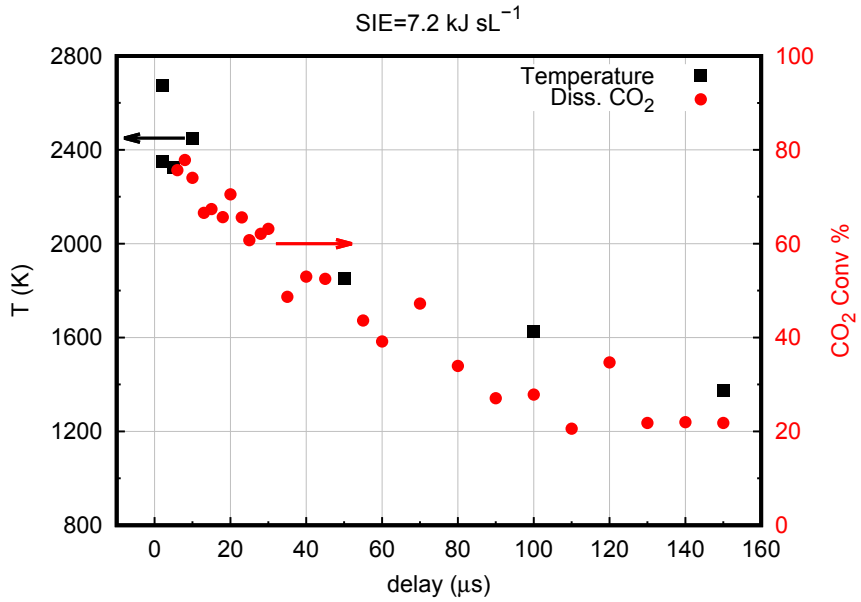

Figure 23: CO_2 conversion as measured by fitting LIF spectra and applying Equation 35. The discharge is operated at 735 Torr on a mixture containing CO_2 and 1% H_2O. Gas temperature is measured from OH excitation spectra.

It is worth remembering that these values are obtained by using the rate coefficients measured in condition of complete rotational thermalization. Consequently, the measurements might be affected by a systematic error. Nevertheless, the obtained values are indicative of the true ones from which they are not expected to vary by more than few points in percentage. In fact, the band ratio calculated from a non–thermal spectrum in pure CO_2 and without the discharge, is very similar to the ratio $k_{1\to0}/k_{Q_{A0}}$ – where the two rate coefficients are those measured in condition of complete thermalization. The same (0,0) and (1,1) rotational distributions can be fitted to spectra measured either with or without discharge. This allows to compare ratios obtained in the two conditions.

Moreover, the same rate coefficients were measured at room temperature, while the temperature in the discharge is found to vary from about 1200 K to 2600 K. Local density variations along the temporal decay do not influence the CO quantification because the $k_{1\to0}/k_{Q0}$ ratio does not depend on pressure. Conversely, the temperature variation can be a source of error because both VET and Q scattering cross sections vary with temperature. However, as shown in Section 2.8.3, such cross sections should share the same temperature behaviour [104], and therefore the $k_{1\to0}/k_{Q0}$ ratio is expected to be constant as function of temperature. The use of rate coefficients measured at room temperature might introduce a systematic error when used at higher temperatures, nonetheless. Additionally, it is worth noticing that predicted curves, only partially verified by the experiments, are

characterized by a flat region extending from 1200 K to 2500 K. This indicates that the $k_{1\to0}/k_{Q0}$ ratio should be constant in the range of temperature relevant for the measurement, hence providing reliability to the temporal profile.

An additional error might be introduced by the fact that, at this experimental resolution, spectra are not perfectly reproduced by the fit.

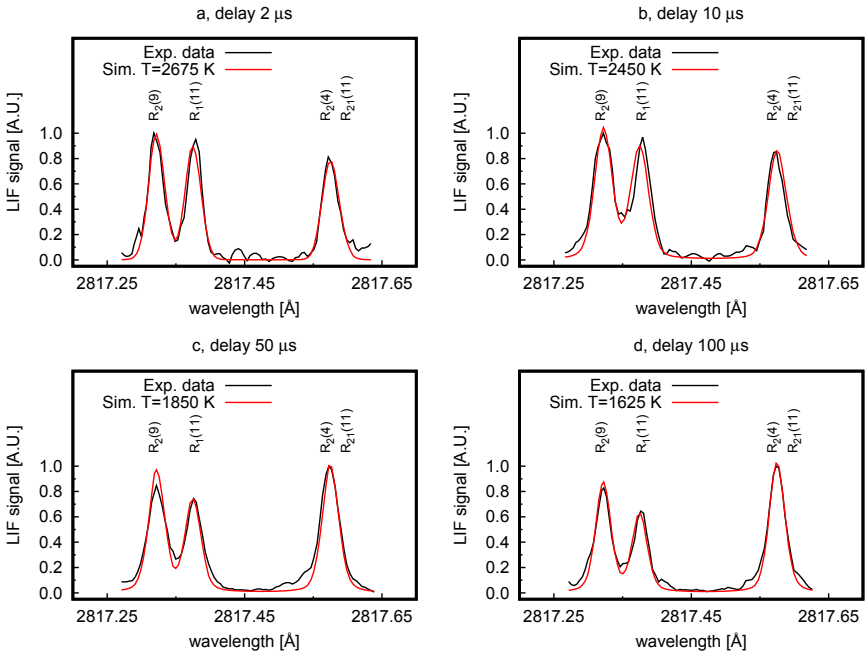

Figure 24: OH excitation spectra at different delays after the discharge burst. The mixture is CO_2 + 1%H_2O at 735 Torr. The energy of the discharge is equal to 2.9 $mJ\,pulse^{-1}$.

Figure 23 shows that the relative amount of CO_2 increases as the delay increases, with a time scale that is compatible with gas fluid dynamic. In fact, it is known that remixing of the gas treated by the discharge with the untreated portion occurs [12]. Of course other chemical routes including back reactions cannot be excluded. With the limited information at our disposal it is not possible to be more precise about the processes causing the CO loss.

Local gas temperature are measured by LIF excitation spectra as in [22]. Spectra are obtained by resonant excitation of the $R_2(4)$, $R_2(9)$, $R_1(11)$ and $R_{21}(11)$ lines. Sample spectra are displayed in Figure 24. Measured temperatures range from about 2500 K close to discharge and to about 1400 K at a delay of 150 µs. Such a quick cooling is probably due to the gas expansion and recirculation described in [12].

3.6 CONCLUSIONS AND OUTLOOK

The goal of this chapter was to present the application of LIF in a collisional environment. Difficulties arise when the collisional partner density is so high to strongly limit the measurement. In fact, high collisional partner density directly reflects into fast quenching frequency. Consequently, the quantum yield of the LIF process is strongly reduced.

Additionally, when quenching is faster than the characteristic decay time of the laser pulse, the fluorescence time decay cannot be measured. In these conditions, the only measurable quantity is the fluorescence spectrum and the quantification of OH is not possible anymore. However, the band ratio, as obtained from the fitting of the fluorescence spectra, can still be successfully used to measure variations in the stoichiometry of the mixture. In this case the focus has moved from the target molecule to the surrounding – OH becomes a molecular probe. The application of LIF and CET–LIF has been demonstrated in severe collisional environments represented by the NRP.

When the mixture contains a conspicuous He concentration:

- rotational thermalization of the excited OH state is complete since $R_{ret} \gg Q_{A0}, Q_{A1}$. Hence, rate coefficients presented in Chapter 2 and published in [61] can be safely used;
- the small molecular gas content keeps the quenching rate low, such that $\tau_l^{-1} \gg Q_{A0}, Q_{A1}$ and the fluorescence pulses can be measured.

Two discharge configurations have been presented, either with or without the use of a dielectric layer. In both cases the CO_2 dissociation rate does not exceed 10%. However, the temporal evolution of the OH concentration has been successfully obtained. Such results are of major interest to test kinetic models for CO_2 dissociation in the presence of noble gas bath.

If on one hand the use of He allows the application of LIF as a whole – with both quantification of the target molecule and of the collisional partner molar fractions – on the other one it makes the discharge less attractive from an industrial point of view. Therefore, the NRP is also investigated for the processing of CO_2 mixtures with small addition of H_2O. H_2O is not only essential to produce OH itself, but also serves as a hydrogen source for the direct synthesis of light hydrocarbons. In this scenario of a fully molecular mixture, quenching rates are so fast that the fluorescence pulse cannot be measured. Hence, the quantum yield of the LIF process is unknown and OH cannot be quantified. CET–LIF is then applied as an indirect measurement of the collisional partners molar fractions. Results show remarkable CO_2 dissociation rate with maximum values of about 80% few

µs after the discharge event. From a spectroscopic point of view, rotational relaxation of the excited state is far from being complete, and this has to be taken into account. In the light of the lacking rotational relaxation at discharge working conditions, a survey on the analysis of such non–thermal fluorescence spectra is given. In conclusion, indications are found that the rate coefficients obtained in condition of complete rotational thermalization as still applicable also to the study of NRP. However, such a usage is not ideal and is the main source of error in the measurement of the dissociation rate. Consequently, future investigations will be performed at higher spectral resolution with the goal of measuring rate coefficients when the condition of rotational thermalization is not satisfied.

4

VIBRATIONAL NON–EQUILIBRIUM

ABSTRACT

This chapter shows how vibrational non–equilibrium can activate endothermic chemical reactions leading to efficient low–temperature chemistry. A general discussion is provided on the concept of non–equilibrium and few relevant examples are given.

Afterwards, attention is devoted to present the vibrational non–equilibrium as occurring in low–temperature molecular plasmas. Theoretical basis are given in the context of understanding what are the conditions that make vibrational non–equilibrium dominant in a molecular plasma. Finally, the cases of vibrational non–equilibrium in CO_2 and N_2 plasmas are presented.

4.1 INTRODUCTION

The non–equilibrium is a vibrant state, a state in which movements and exchange of energy happen. It is the state of life and, being alive, is then tantamount to being in non–equilibrium. The non–equilibrium is everywhere and, every day, each living system struggles to keep itself out of equilibrium. When the forces keeping a system out of equilibrium cease to exist, "the whole system fades away into a dead, inert lump of matter. A permanent state is reached, in which no observable events occur", as Erwin Schrödinger writes in his book "What is Life" [96]. The state of equilibrium – the state of maximum entropy – is the state which every system gravitates around, to finally fall into. But if this is the case, "how does the living organism avoid decay?", Schrödinger asks himself, "the obvious answer is: by eating, drinking, breathing [...] and assimilating". To keep a system out of equilibrium, to prevent it to die, energy needs to flow.

The non–equilibrium is naturally everywhere and the living cell is its most noticeable manifestation. Additionally, mankind has been able to learn how to manipulate systems that can possibly deviate from thermodynamic equilibrium. When energy is proficiently made to flow through such a systems, unprecedented behaviours can be triggered. One of such a systems is the laser.

For the scope of this thesis, especially the case of the CO_2 laser is a pertinent example. Laser systems intrinsically rely on non–equilibrium distribution of energy among the levels involved in the lasing transition. In order for stimulated emission to occur, high energy levels need to be overpopulated as compared to low energy ones. However, this requirement goes against what an equilibrium distribution of molecules, as described by the Boltzmann distribution, would predict. Since a system naturally tends to reach equilibrium, effort is needed in order to drive it *out* of equilibrium. In the case of the CO_2 laser, this is accomplished by promoting energy flow from a system where no inversion of population is observed, to the one where it is required. Specifically, a mixture of CO_2 and N_2 (plus other components not relevant for this discussion) serves the purpose. By using an electric discharge, N_2 is vibrationally excited and up to 50% [41] of the population is moved to the first vibrational level, see Figure 25.

The excitation of N_2 is very efficient because, by not having a permanent dipole moment, it cannot decay radiatively. The first vibrational level of N_2 ($v = 1$) and that of the asymmetric stretch of CO_2 (00^01) have similar energies. Therefore, they are in resonance and energy can flow very efficiently between the two states. Consequently, the energy loaded in the first vibrational state of N_2 can be transferred to CO_2 by means of molecular collisions. Inversion of population of the (00^01) state of CO_2 with respect to the (10^00) and (02^00) levels is achieved, therefore enabling lasing transitions. This is a successful

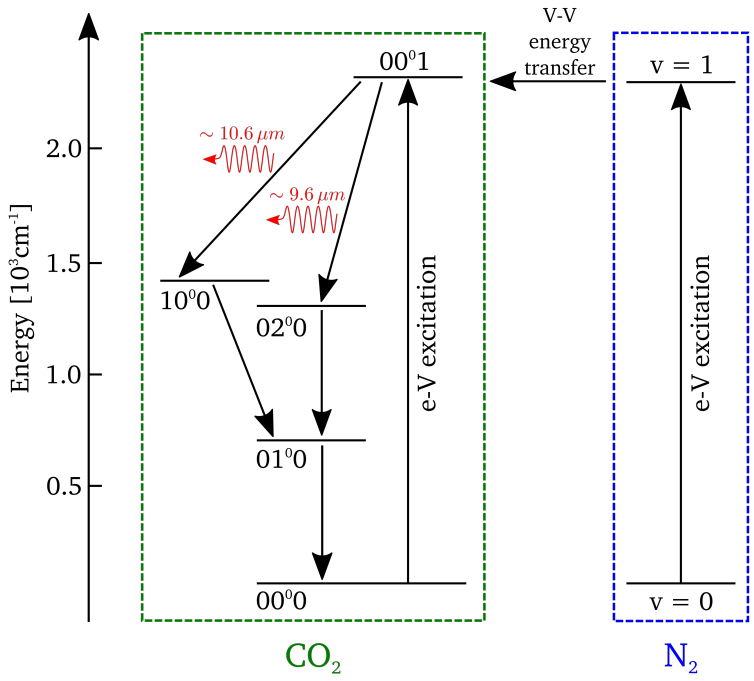

Figure 25: The CO_2 laser level system with vibrational levels of CO_2 and N_2 directly involved in the lasing transition. The first vibrational level of N_2 and the $(00^0 1)$ one of CO_2 are excited by means of an electric discharge.

example of how the vibrational non–equilibrium can promote characteristics of great interest, both from a scientific and a technological point of view.

4.2 ENHANCING CHEMICAL REACTIVITY

As already introduced in Chapter 1, vibrational excitation is recognized to play an important role in enhancing the reactivity of molecules undergoing endothermic reactions. In a seminal paper, Polanyi and Wong [80] have shown that, for the case of the simple reaction

$$A + BC \rightarrow AB + C, \tag{38}$$

the reactant vibrational energy helps in surmounting a late barrier, i.e. a barrier located in the product channel. On the contrary, translational energy helps in surmounting an early barrier, a barrier located in the reactant channel. This can be understood on a physical ground by noting that an early barrier is encountered while A and BC are approaching each other, thus translational energy is required to overcome it. Conversely, a late barrier is the barrier that must be surmounted to detach C from B, hence requiring vibrational energy.

The vibrationally adiabatic[1] synthesis of NO is an example that well suffices in showing how effective vibrational excitation can be. The synthesis of nitrogen oxides in air plasma is a well known process in plasma technology. The first attempt to produce nitrogen oxides from air by using plasma was done by Birkeland and Eyde in 1900. They developed thermal arc furnaces able to produce nitrogen oxides with a yield of about 2% and with a very low energy efficiency of about 4%. The reason for such a low performance in the thermal synthesis of NO is the remarkable strength of the N_2 triple bond, 10 eV. However, that bond can be very efficiently cleaved if nitrogen molecules are vibrationally excited:

$$O(^3P) + N_2^*(^1\Sigma_g^+, v) \rightarrow NO(^2\Pi) + N(^4S) \qquad \Delta H \simeq 3\, eV\, mol^{-1}. \quad (39)$$

Equation 39 is followed by a secondary reaction

$$N + O_2 \rightarrow NO + O \qquad \Delta H \simeq -1\, eV\, mol^{-1}, \quad (40)$$

that closes the cycle providing the atomic oxygen consumed by Equation 39.

Vibrationally excited N_2 molecules are obtained by collisions with low energetic electrons in a low–temperature discharge. The chain reaction composed by Equation 39 and Equation 40 is known as the Zeldovich mechanism. Synthesis of NO in non–equilibrium microwave discharge has been obtained with efficiency of about 30% with NO yield of about 80–90% [40].

Vibrational excitation can also substantially influence the way molecules interact with surfaces, i.e. with catalysts. Additionally, for the case of polyatomic molecules – for which more than one mode of vibration is present – excitation of different modes gives different results as well. For example, when CH_4 is vibrationally excited by two quanta of the asymmetric stretch, the sticking probability on Ni(100) surface can be up to three orders of magnitude higher than that of ground state molecules [25]. Moreover, symmetric stretch excitation appears to be ten times more efficient than antisymmetric excitation.

Overpopulation of high vibrational levels is achieved in the presence of active pumping of low vibrational levels due to anharmonicity of the potential. Reaction rates of vibrationally excited molecules result to be greatly enhanced. Few remarkable examples are worth mentioning. The cross section for the slightly endothermic reaction

$$K + HCl(v = 0) \rightarrow KCl + H \qquad \Delta H_0 = +4\, kJ\, mol^{-1} \quad (41)$$

1 Vibrationally adiabatic trajectories are those that follow the minimum energy pathway through the multidimensional potential energy surface (PES) [98]. Within this picture, trajectories of both vibrationally excited and not reactants will travel through the point of minimum energy in the PES. Consequently, the decrease in the energy barrier cannot exceed the reactant vibrational energy.

for the case of vibrationally excited HCl($v = 1$) is ten times larger than what would be obtained if the same amount of energy were provided in form of translational excitation [72]. According to calculations on potential energy surfaces [80], the beneficial effect of vibrational excitation is expected to increase as the reaction becomes more endothermic. Indeed, the rate of the reaction

$$Br + HCl(v = 0) \rightarrow HBr + Cl \qquad \Delta H_0 = 65.2\,kJ\,mol^{-1}, \qquad (42)$$

increases by a factor 10^{11} at room temperature if HCl is excited into $v = 2$ vibrational level [5].

Similar arguments apply to the case of CO_2. Efficient dissociation of the CO_2 molecule is expected to happen through excitation of the asymmetric vibrational mode [29]. Substantial overpopulation of the asymmetric mode up to $v = 9$ has been demonstrated in CO_2 laser discharges [19]. Moreover, dissociation rates of up to 50% were measured if H_2O was not added to the laser mixture [41]. From research carried in the seventies and eighties on CO_2 low–temperature plasma [90][9][29][10], it has been speculated that vibrational excitation can significantly enhance CO_2 dissociation.

The proposed mechanism is not a single step one, but rather a multi step process in which high levels of excitation in the asymmetric mode are obtained through molecular collisions. Dissociation is achieved by intersystem crossing from the electronic ground state to $^3B_2$ electronic state at 5.1 eV, see Figure 26. Molecules can undergo this transition as soon as they reach the 20^{th} vibrational level of the asymmetric mode, located at 5.1 eV.

A great body of research allegedly consider vibrational excitation of CO_2 non–thermal plasma the way to achieve high energy efficiencies. However, to date there is no experimental evidence that vibrational excitation in CO_2 leads to dissociation.

4.3 MOLECULAR VIBRATIONAL NON–EQUILIBRIUM

Section 4.2 shows the extent by which vibrational excitation can change the fate of endothermic reactions that would otherwise be very difficult to achieve in a thermal scenario. However, vibrational excitation does not happen naturally and needs to be induced in the system. In the context of enhancing the reactivity of stable molecules, this is usually achieved by means of low–temperature plasmas.

This section reports on the mechanisms leading to vibrational non–equilibrium. It starts with a definition of it with the aim of understanding how a system in non–equilibrium differs from one at the thermodynamic equilibrium.

When a gas is in thermal equilibrium, the distribution of energy within the accessible modes is described by the Boltzmann distribu-

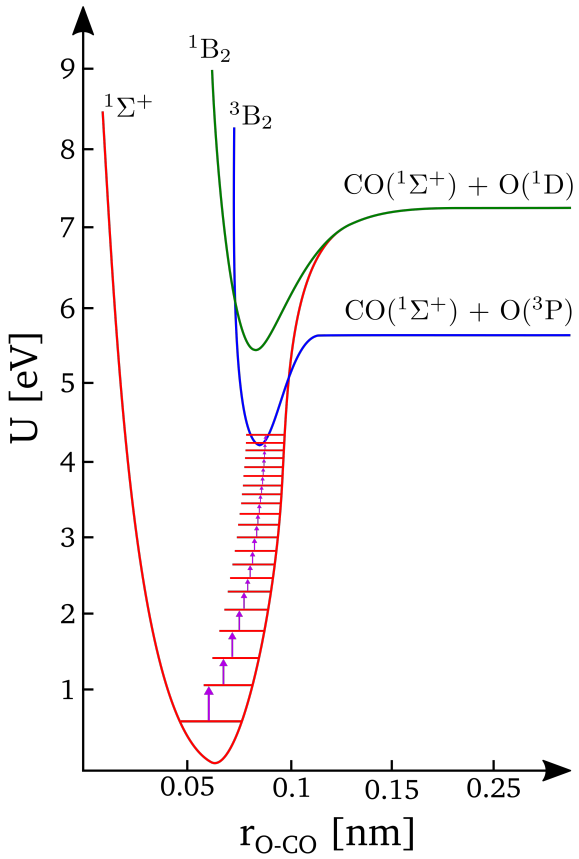

Figure 26: Schematic for electronic and vibrational energy levels of CO_2 involved in the efficient dissociation of CO_2 by vibrational excitation.

tion. According to this picture, the occupancy of a generic state i can be calculated as

$$\frac{n_i}{N} = \frac{g_i \exp\left(-\frac{E_i}{k_b T_{gas}}\right)}{\sum_i g_i \exp\left(-\frac{E_i}{k_b T_{gas}}\right)}, \tag{43}$$

where N is the total number of molecules, g_i is a statistical weight describing the degeneracy of the i^{th} state, k_b is the Boltzmann constant and T_{gas} is the gas temperature. In the context of vibrational non–equilibrium in low–temperature plasmas, two scenarios are possible:

1. the distribution of molecules over the accessible rotational and vibrational states are described by the same Equation 43 with two different temperatures T_r and T_v, respectively;

2. a unique T_v cannot be assigned to the distribution of vibrational states and Equation 43 cannot be used to describe such a distribution.

For the case where a unique T_v cannot be assigned to the distribution of vibrational states, an ad–hoc first level vibrational temperature

$T_{v(0,1)}$ [49][27] can still be used. It allows to describe the fractional distribution by using an alternative distribution function as, for example, the Treanor distribution [110]; the use of which permits to interpret the non–equilibrium character of the investigated gas.

The temperature is a quantity describing the average energy of a physical system. Being associated to the Boltzmann distribution of energy, it is meaningful only if the system is in thermodynamic equilibrium. When this condition ceases to be true, a single temperature does not suffices anymore in describing the energy content of all the modes in the system. Consequently, in the presence of non–equilibrium, the energy content of each mode is described by its specific temperature. In plasmas, these temperatures are: electron temperature (T_e), ion temperature (T_i), vibrational temperature (T_v), rotational temperature (T_r) and gas temperature (T_{gas}).

It is common to assume the rotational mode to be in equilibrium with the translational ones, $T_r \equiv T_{gas}$. This assumption is based on the fact that rotational–translational relaxation is a very fast process. Indeed, 10^0 to 10^1 collisions only, in a range of translational temperature from 10^2 K to 10^4 K, are sufficient to equilibrate the rotational distribution of N_2 to the translational temperature of the mixture [75]. Moreover, ions are much heavier than electrons and therefore they react slowly to the electric field present in the plasma. Hence, their kinetic energy is much lower and their temperature is in equilibrium with the gas one. In this work, the measured rotational temperature will be continuously confused with the translational one.

Conversely, the equilibration of the vibrational distribution to the translational temperature is slow and, for N_2, typically occurs after 10^3 to 10^6 collisions for translational temperature from 10^3 K to 10^4 K [75]. This is the reason why vibrational non–equilibrium is such a common condition to obtain in molecular gases.

In order for the vibrational non–equilibrium to be dominant in the plasma, the following hierarchy on characteristic temperatures has to be verified:

$$T_{gas} \simeq T_i \simeq T_r \quad \ll \quad T_v \quad < \quad T_e. \tag{44}$$

A lot has been written on this subject and an in–depth discussion on the theory and the modelling of vibrational non–equilibrium goes beyond the scope of this thesis. Detailed theoretical treatment is given in [11], additionally, extensive experimental investigation of the implications of such a non–equilibrium concept is given in [29].

As aforementioned, the concept of temperature is linked to the average energy of a physical system, in this case represented by an ensemble of diatomic molecules. The higher the temperature the more high energy levels are populated. The way these levels are spaced in energy defines the distribution of molecules at a given temperature. The energy state of a diatomic molecule can be described as the sum of electronic, vibrational and rotational states; with energies of the

order of $10^4\,cm^{-1}$, $10^3\,cm^{-1}$ and $10^0\,cm^{-1}$, respectively. Given the scope of this work, the treatment is restricted to vibrational levels of a molecule in its electronic ground state.

The vibrational manifold is usually described by a second order approximation of the anharmonic oscillator formula, that is

$$E_\nu = \omega_e\left(\nu+\frac{1}{2}\right) - \omega_e\chi_e\left(\nu+\frac{1}{2}\right)^2, \tag{45}$$

where E_ν is the energy of the vibrational level ν, ω_e is the fundamental vibrational frequency and χ_e is the second order anharmonicity factor. The anharmonicity factor χ_e is much smaller than unity, $\chi_e \ll 1$, and therefore the second term of RHS of Equation 45 becomes important only for large values of ν. Nevertheless, the anharmonicity of the potential is essential for the vibrational non–equilibrium to take place.

This can be understood by considering a vibration–vibration collision (VV) between a molecule in a state ν and one in a state ω, with $\nu < \omega$, as shown in [86]. VV is an inelastic process that conserves quanta [110], but not energy, within the vibrational manifold. Two possible processes occurring during the collision of two molecules M in the ν and ω vibrational states, respectively, are:

$$M_\nu + M_\omega \rightarrow M_{\nu-1} + M_{\omega+1} \quad \Delta E = 2\omega_e\chi_e(\nu-\omega+1), \tag{46}$$

$$M_\nu + M_\omega \rightarrow M_{\nu+1} + M_{\omega-1} \quad \Delta E = -2\omega_e\chi_e(\nu-\omega+1). \tag{47}$$

For the process described by Equation 46, the amount of energy $\Delta E < 1$ is released from the vibrational manifold to the thermal bath in form of molecular rotation and translation. Since rotations and translations form together an energy continuum, there is no energy threshold for this process that is always permitted. On the other hand, $\Delta E > 1$ in Equation 47, so energy needs to be provided by the thermal bath. In this case, a well defined amount of energy needs to be absorbed by the colliding molecules in order to overcome the energy barrier of the vibrational transition, and from statistics argument only a fraction $\exp\left(-\frac{\Delta E}{kT_{gas}}\right)$ of the molecules in the thermal bath has this amount of energy. In the end, collisions such that high vibrational states are populated at the expense of the lower ones are favoured. According to this picture, low T_{gas} reduces the fraction $\exp\left(-\frac{\Delta E}{kT_{gas}}\right)$ thus increasing the bias towards pumping of higher vibrational states. This process is usually referred to as vibrational–vibrational up–pumping (VV up–pumping) or vibrational ladder climbing.

Such exponential temperature dependence would suggest extreme overpopulation of the high vibrational states, as predicted by the Treanor distribution [110]

$$\frac{N_\nu}{N_0} = \exp\left(-\frac{\nu E_1}{k_b T_{\nu(0,1)}} + \frac{\nu E_1 - E_\nu}{k_b T_r}\right), \tag{48}$$

where N_ν is the number of molecules in the vibrational state ν, N_0 the number of molecules in the vibrational ground state, k_b is the Boltzmann constant, E_1 is the difference between the (vibrational) energy of the first vibrational state and that of the ground state, $E_1 = E(\nu = 1) - E(\nu = 0)$, similarly $E_\nu = E(\nu) - E(\nu = 0)$, T_r is the gas temperature and $T_{\nu(0,1)}$ is the so called *first level vibrational temperature* [49],

$$T_{\nu(0,1)} = \frac{\theta_{(0,1)}}{\log\left(\frac{N_0}{N_1}\right)}, \tag{49}$$

where θ is a parameter, with the units of a temperature, proportional to the energy difference between the ground and the first vibrational level. In Equation 49, N_0 and N_1 are the populations of the ground and first vibrational level, respectively. At this stage, due to deviation from the Boltzmann distribution, the concept of temperature loses its ability to represent the energy content of the system. A vibrational temperature defined in this way should be regarded as a mere parameter useful to describe, with the help of a dedicated formula, the occupancy of the vibrational states when the Boltzmann distribution ceases to be applicable.

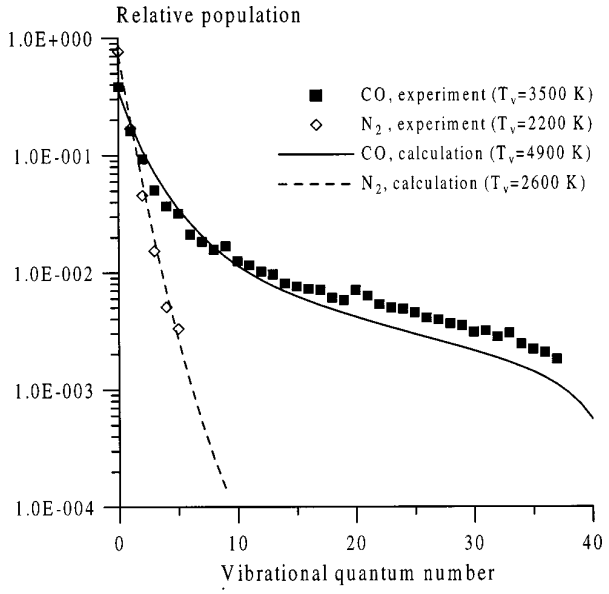

Figure 27: Experimental (symbols) and calculated (solid lines) centerline VDFs of N_2 and CO. Reproduced from [49], with the permission of AIP Publishing.

The Treanor distribution is derived by considering vibrational to translational relaxation (VT) negligible as compared to VV. Neglecting VT processes leads to fairly low T_τ, exponentially increasing the population of high vibrational states, see Equation 48. However, VT rates exponentially increases as a function of the vibrational quantum number [11], even at low T_τ, preventing the extreme overpopulation predicted by the Treanor distribution to occur experimentally. More realistic models, as the one developed by Gordiets and Mamedov [33], include both VV and VT terms to describe the vibrational distribution when VT rates are not negligible.

The introduction of VT rates usually leads to the appearance of three different sections in the vibrational distribution function (VDF) [106], see Figure 27 for an example. For low quanta, the VDF is very similar to a Treanor distribution with a slope defined by the excitation rate. The second part is usually referred to as the "Treanor plateau" [85], a region where VV and VT rates balance stabilizing the vibrational distribution. Finally, at high quanta, VT rates exceed VV ones and fast decay of high vibrational levels is observed.

Vibrational energy transfer has been extensively investigated, both theoretically and experimentally. Figure 27 shows vibrational distribution in a N_2/CO mixture. In this specific case energy is loaded into the CO vibrational mode by optical pumping of its first two vibrational levels by means of a mid-IR CO laser. Subsequently, VV up–pumping redistributes the energy among higher vibrational states through molecular collisions.

4.4 VIBRATIONAL EXCITATION IN LOW–TEMPERATURE PLASMAS

Since any system naturally tends to *equilibrate* at a state of minimal energy, an *equilibrium* state, an active pumping mechanism is necessary to maintain the system *out* of equilibrium. Two means of excitation can be used to selectively load energy in the vibrational mode: optical pumping [49][113] and electron collisions [67]. The excitation by electron collisions is typical of the realm of plasma.

Vibrational distribution functions are usually calculated by solving a master equation – a differential equation including kinetic terms of the competing processes. Extensive literature [86][106][11] is available on the subject. The goal of this section is to briefly present what are the competing processes defining the extent of vibrational non–equilibrium in a low–temperature plasma.

In the system represented by a low–temperature molecular plasma, the equation describing the conservation of the population of each vibrational state can be written as

$$\frac{dN_v}{dt} = VV + PUMP - VT - VE - SRD - CHM. \tag{50}$$

The RHS of Equation 50 includes all those processes that can change the vibrational population of a diatomic molecule. VV represents all the processes that change the vibrational distribution through molecular collisions. It is worth noticing that the anharmonicity of the potential, see Equation 45, is essential for this specific process to take place. Indeed, if the vibrational mode were harmonic, the associated quantum states would be equally spaced in energy. Consequently, the processes described in Equation 46 and Equation 47 had the same probability of occurring and no preferential population of high vibrational states would be observed. The PUMP term is a source of vibrationally excited molecules, in this case obtained by electron impact. VT and VE describes the loss of energy from the vibrational mode to translational and electronic ones, respectively. SRD represents the change of vibrational state by means of spontaneous radiative emission – accessible by molecules that have a permanent dipole moment. CHM include the losses of vibrational energy through chemical reactions, especially important when vibrational kinetics is exploited to enhance chemical reactivity, as for the case of CO_2 dissociation.

It is known that low energetic electrons, obtained at low E/N, are efficient at selectively couple energy into molecular vibrations [11]. Additionally, energy deposition into the vibrational mode occurs preferentially through low vibrational quanta. Plasma becomes then an effective medium of vibrational excitation provided the electron temperature (T_e) is on the right range where the cross section of electron–vibration transition is maximum. On this regard, microwave plasma are known to be suitable to establish the right conditions for vibrational excitation: $T_e = 1\,eV$ to $2\,eV$ [29]. The reason relies on the possibility of sustaining a plasma, in steady state, in a radio frequency cavity. Not having to apply voltage to any electrode permits the plasma to exist even at very low values of electric field. Conversely, in the case of dielectric barrier discharges (DBDs), the discharge is operated in a completely different regime. The presence of electrodes and associated dielectric coatings requires pulsed operation. Ultimately, the discharge characteristics is ruled by the Paschen's law, and high electric fields need to be applied to initiate ionization.

In order for vibrational non–equilibrium to become dominant, it is necessary to maximize the energy loading in the desired vibrational mode and minimize at the same time the de-excitation processes. On this regard, the VT term in Equation 50 plays an important role. VT relaxation rates increases linearly with pressure – due to a linear increase in the collision frequency – and exponentially with gas temperature, see Figure 28. Such an exponential behaviour was first described by Landau and Teller [48] by modelling the relaxation of

harmonic oscillators by collisions with atoms [70]. They obtained the well known Landau–Teller formula,

$$k_{VT}^{1\to 0} \propto \exp\left(-\frac{B}{\sqrt[3]{T_{gas}}}\right), \tag{51}$$

which describes the VT relaxation rate of the first vibrational level of a diatomic molecule as a function of gas temperature. Rapid decrease in the number of collisions necessary to establish vibrational equilibrium in an ensemble of classical oscillators was also described by Parker [75].

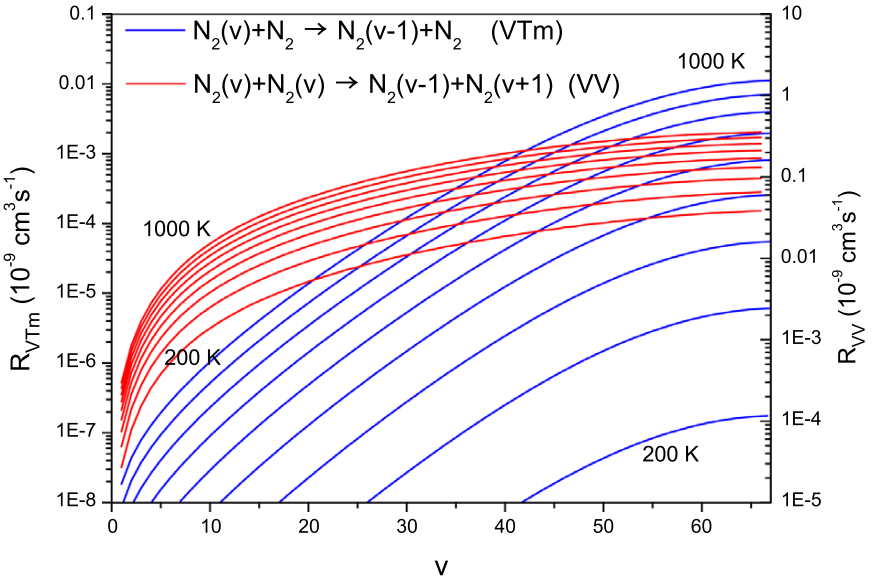

Figure 28: Rate coefficients for one–quantum de–excitation in $N_2(v)$–N_2 by VT [7], in blue, and quasi–resonant VV, in red, as function of vibrational quanta for different gas temperature from 200 K to 1000 K [57]. The data is obtained by fitting formulas [32] and is normalized to the whole vibrational ladder [4]. Reproduced with permission from [106].

In the end, the successful establishment of vibrational non equilibrium is defined by two counteracting processes:

- energy has to be efficiently loaded into the vibrational mode by collision with low energetic electrons. This can be achieved and controlled by tuning E/N;
- gas temperature and pressure negatively influence the build–up of vibrational non-equilibrium by increasing VT transfer rates.

Given this scenario, it is then clear that the right combination of T_e, T_v and T_r is essential for the non–equilibrium to be established. Specif-

ically, if the following hierarchy of the characteristic temperatures is met

$$T_r \ll T_v \simeq 2 \times 10^3\,K < T_e = (1to3) \times 10^4\,K, \quad (52)$$

the non–equilibrium is maximum and the vibrationally excited molecules will undergo chemical reactions with high energy efficiency [28].

Extensive literature is available on the study of vibrational non–equilibrium in low–pressure plasma, where suitable conditions can be more easily met. However, in the context of the electrification of the chemical industry, low–pressure reactors are not as attractive as high–pressure ones, because they require the use of costly vacuum systems. This is the reason why a great body of research is now investigating non–equilibrium processes in high–pressure discharges [89][8][35].

4.4.1 *CO_2 and N_2 non–equilibrium plasmas*

Energy coupling efficiency of vibrational excitation by electron collisions for CO_2 and N_2 are shown in Figure 29. These graphs are obtained by using the Bolsig[2] software and the IST-Lisbon database from LXCat[3] [3]. They show the fraction of energy coupled to the vibrational modes normalized to the energy absorbed by the electrons. Since the CO_2 vibrational structure is much more complicated than the N_2 one, CO_2 is expected to behave differently when excited by electron collisions. Indeed, by looking at Figure 29 it is possible to appreciate the differences between the vibrational excitation patterns of the two molecules.

For N_2, almost 100% of the electron energy from 10^0 Td to 10^1 Td is coupled to the first vibrational level. In the region from 10^1 Td to 10^2 Td higher vibrational levels starts to be populated at the expense of the fundamental one. Overall, the energy carried by the electrons is almost entirely transferred to the single mode of vibration in the range of E/N from 10^0 Td to 10^2 Td.

Conversely, the situation is fairly different for CO_2. Being a linear triatomic (number of atoms N = 3) molecule, CO_2 possesses 3N - 5 = 4 normal modes of vibration. They can be divided in symmetric and antisymmetric modes. The symmetric ones can be further dived in symmetric stretch ($v_1$00) and two degenerate bending modes (0$v_2$0). The antisymmetric mode is called antisymmetric stretch (00v_3).

When a molecule has more than one mode of vibration, it can happen that levels belonging to two different modes have almost the same energy. They are described as to be in accidental degeneracy. In CO_2, this occurs for the (020) and (100) levels (CO_2 Fermi resonance), and for higher orders as well. Consequently, populations of the symmetric stretch and of the bending mode equilibrate very fast. For this

2 To be found online at: https://www.bolsig.laplace.univ-tlse.fr/
3 To be found online at: https://fr.lxcat.net/data/set_specB.php

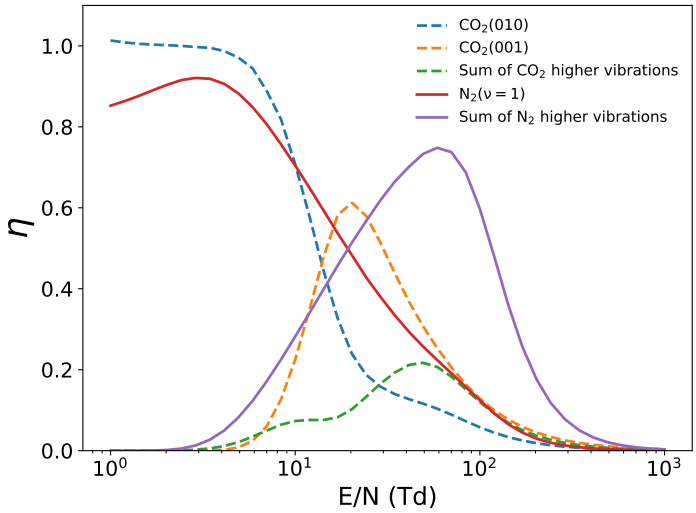

Figure 29: Fraction of electron energy transferred to different vibrational excitation channels in pure CO_2 an pure N_2, as a function of the reduced electric field (E/n). They are calculated from the corresponding cross sections of the electron impact reactions from the IST-Lisbon database on LXCat [3] by using the Bolsig solver for DC field.

reason, only two temperature are necessary to describe the distribution of energy within the CO_2 vibrational system: T_{12} for symmetric stretch and bending mode and T_3 for the asymmetric stretch.

A comparison of CO_2 and N_2 behaviours for low values of E/N shown in Figure 29 highlights the physical characteristics of the two plasmas. In the case of CO_2, most of the energy is coupled to the bending mode for values of E/N lower than 10^1 Td. This is detrimental for the establishment of vibrational non–equilibrium. The reason is the fine energy spacing of the bending mode that results in fast energy transfer to the translational mode via VT relaxation. Hence, $T_{12} \simeq T_{gas}$. Therefore, it happens to be very challenging to vibrational excite CO_2 without increasing the gas temperature.

In the context of enhancing CO_2 dissociation through vibrational excitation, energy loading into the asymmetric stretch is preferred over the others because:

- it has the highest cross section for excitation through electron collisions in the range of reduced electric field (E/N) from 10 Td to 100 Td [100];
- VT rates are the lowest due to its large energy spacing [47].

The only region where electron collisions can be efficient in driving non–equilibrium is for values of E/N from 10^1 Td to 10^2 Td. In this region, an appreciable amount of energy can be loaded into the asymmetric stretch that, thanks to the low VT rate, can drive the VV up–pumping.

5

ASSESSING THE VIBRATIONAL NON–EQUILIBRIUM IN N_2 MICROWAVE DISCHARGES.

ABSTRACT

In the context of utilising electrical energy for chemical conversion, this chapter shows the investigation of vibrational activation of N_2 molecules in a flowing microwave plasma. As presented in Chapter 4, the characteristic quantities defining the degree of vibrational non–equilibrium are the rotational (T_r) and vibrational ($T_{v(0,1)}$) temperatures. Consequently, those are the primary targets of this investigation. Measurements are performed by means of Raman scattering in order to measure such temperatures together with the energy distribution over the vibrational states.

Firstly, a brief introduction about the theory of Raman scattering is provided, with special attention devoted to the role that T_r and $T_{v(0,1)}$ have in shaping the spectra. Afterwards, the experimental setup is presented before going into details of the experimental investigation.

Since microwave plasmas are spatially inhomogeneous, a spatially resolved study is required. Hence, the plasma is mapped both radially and axially. Maximum values of T_r = 3500 K and $T_{v(0,1)}$ = 7000 K are observed in the radial centre of the plasma with the discharge operated at 50 mbar. The ratio $T_r/T_{v(0,1)}$ is then chosen as a good parameter to visualize the degree of non–equilibrium. Values of $T_r/T_{v(0,1)}$ as high as four are measured in the low pressure discharge.

Additionally, a detailed quantification of the local energy content is made to cast light on the distribution of internal energy of N_2. To this end, rotational–translational and vibrational energy densities are defined and calculated in order to make a comparison with the energy delivered by the source. Ultimately, measurements performed downstream of the plasma display the ability of the microwave flowing reactor to deliver up to 48% of the specific energy input (SEI) into internal degrees of freedom of the gas molecules. If the calculation is contended to vibrational energy only, it is found that the loading efficiency is equal to 23%.

5.1 INTRODUCTION

Among the existing plasma reactors, microwave ones are attractive for modular chemical plants in view of their low inertia, low investment cost and high energy density. Additionally, they are suitable to sustain plasma with low reduced electric fields and, for this reason, they are expected to be efficient sources of excitation of the vibrational modes of molecular gases [89]. Moreover, plasma reactors can be directly powered with electricity from renewable energy sources making them suitable for the processing of stable molecules in the context of a circular economy. Some key chemical industrial processes where microwave plasmas can be used are the production of nitrogen based fertilisers (for example NH_4NO_3) by nitrogen fixation [15], methane conversion [92][50] and CO_2 dissociation for the synthesis of synthetic fuels [89][35][8].

Since microwave plasmas are, in principle, capable to selectively load energy into molecular vibrations, they are gaining attention for plasma–chemistry applications. Especially vibrational excitation is recognised to enhance chemical reactivity of stable molecules like N_2. Favourable conditions are expected to be achieved in microwave plasma if free electrons driven by the electric field transfer energy preferentially into vibrational degrees of freedom of N_2 molecules. This is particularly achievable for microwave discharges since these are characterised by a relatively low ionisation degree ranging from 10^{-5} to 10^{-4} and, since the vibration–to–vibration energy transfer rate (k_{VV}) is larger than the electron impact dissociation rate (k_{eD}) [11], the dissociation can predominantly proceed via vibrational excitation rather than by electron impact dissociative excitation [9].

For the case of endothermic reactions, vibrational excitation is considered to be essential to obtain the intermediate state that leads to product formation [31]. Consequently, vibrational energy of reactants becomes the control knob for endothermic reactions as that energy is required to overcome the energy barrier and assist in achieving high energy efficiency [28]. However, the detailed understanding on how to make vibrational excitation dominant in the reactor and to achieve the maximum possible energy efficiency is still lacking, preventing microwave plasma technology to penetrate into the chemical industry.

A proficient knowledge of the thermodynamic state of the process gas is indispensable to master the loading of vibrational energy. Ultimately, experimental evidence of the desired deviation from thermal equilibrium has to be quantified by measuring markers like temperatures and distribution of molecules over the accessible states.

5.2 RAMAN SCATTERING IN NON–EQUILIBRIUM PLASMAS

This section deals with the basics of the theory underlying the Raman process. The vast majority of the information found in this chapter is adapted from the books of Long [53], and Herzberg [37][36]. The goal of this section is not to mirror that vast mole of information, to which the reader is invited to refer to for a more detailed treatment, but rather summarize the key concepts considered to be necessary for the understanding of the following sections.

Special attention is devoted to the influence of experimental parameters of interest for this study, like temperature and vibrational distribution, in defining the shape of a Raman spectrum. Calculations are made by using available spectroscopic data as to provide a model to fit to the measured spectra.

5.2.1 *The Raman Effect*

Raman scattering is an inelastic process in which the incident and scattered radiation have different energies. The energy shift is due to the interaction with molecules whose polarizability is modified by the electric field of the incident radiation. Hence, in order for Raman to occur the basic selection rule requires a change in the polarizability during the molecular vibration, or rotation, probed by the laser.

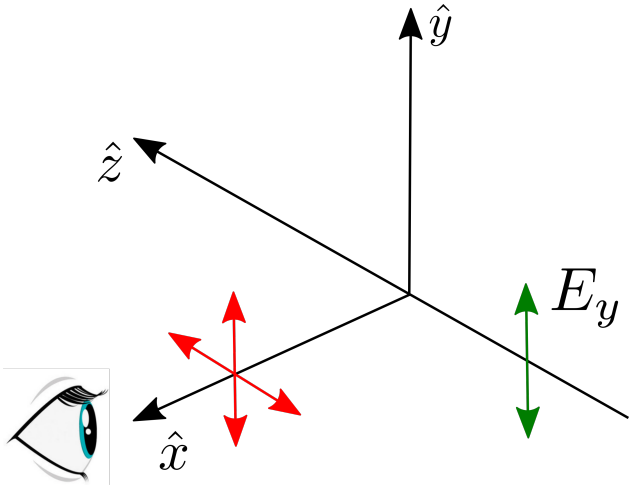

Figure 30: Coordinate system showing the configuration at which the Raman signal is detected. The incoming laser beam propagates along the z axis. It is monochromatic and linearly polarized on the $x\hat{y}$ plane. Scattered light is detected on the $z\hat{y}$ plane, on the direction x. No polarizing elements are employed and both polarizations are then detected.

The interaction of the incoming laser photons with the probed molecule is usually described via a virtual state. A virtual state is a state with a well defined energy, that can take any value, but that is not

associated with any physical state of the molecule. Therefore, no resonant absorption of energy occurs upon interaction with this state, that can be regarded as a state that allows transitions other than resonant absorption to occur. Such a interaction with a virtual state is called *virtual absorption*.

Upon interaction with the molecules, the resulting scattered light can either gain or loose a discrete amount of energy proportional to the change in the vibrational (ν) and/or rotational (J) quantum number induced in the non–resonant Raman transition. In this work, ro–vibrational Raman is used only, so the following discussion is limited to transitions characterized by a change in the vibrational quantum number, $\Delta\nu \neq 0$.

The intensity of the scattered radiation is not homogeneous over the solid angle. It is function of the angles, azimuthal and longitudinal, at which it is detected. By referring to Figure 30, it is advantageous to collect the scattered radiation in the $z\hat{y}$ plane where 1) the cross section is the largest and 2) there is the least chance of collecting stray light. The geometrical configuration depicted in Figure 30 is the one used in this work. Hence, the following discussion on the intensity of the Raman signal is contended to this specific geometrical configuration.

5.2.2 *Ro–vibrational Raman in linear molecules*

For the particular case displayed in Figure 30, the intensity of a rotational–vibrational Raman line can be written as

$$I_i = N\left(\frac{\pi}{\epsilon_0}\right)^2 (\nu_l \pm |\Delta\nu(\nu, J)|_i)^4\, \Phi(\nu', J)_i \frac{g_i \exp\left(-\frac{hcB_i J(J+1)}{k_b T_r}\right)}{\sum_i g_i \exp\left(-\frac{hcB_i J(J+1)}{k_b T_r}\right)}, \quad (53)$$

where, i labels S, Q, and O branches, N is the local number density of molecules and ν_l is the wavenumber of the incoming laser radiation.

S, Q and O are the branches that form a rotational–vibrational Raman spectra. They are characterized by the same $\Delta\nu = \pm 1$, but different ΔJ. Explicitly, O ($\Delta J = +2$), Q ($\Delta J = 0$) and S ($\Delta J = -2$).

$|\Delta\nu(\nu, J)|$ is the Raman shift induced in the transition. For S, Q and O branches it is equal to[1]

$$|\Delta\nu(\nu, J)|_S \simeq \nu_{vib}(\nu) + 6B' + (5B' - B'')J + (B' - B'')J^2, \quad (54)$$

$$|\Delta\nu(\nu, J)|_Q \simeq \nu_{vib}(\nu) + (B' - B'')J(J+1), \quad (55)$$

$$|\Delta\nu(\nu, J)|_O \simeq \nu_{vib}(\nu) + 2B' - (3B' - B'')J + (B' - B'')J^2, \quad (56)$$

1 Neglecting higher order terms for the rotational constant D, since $\frac{D}{B} \simeq 10^{-6}$, for the cases of CO and N_2.

where ν_{vib} is the wavenumber of the considered vibration, B' and B'' are the rotational constants of the upper and lower state, respectively.

The $\pm$ sign in the quartic term of Equation 53 discerns between Stokes (-) and anti–Stokes (+) bands. Specifically, the Stokes (anti–Stokes) band consists of the amount of light that is red (blue) shifted with respect to the incoming radiation. Their intensities depend on 1) the gas temperatures – that defines the distribution of molecules over the vibrational mode – and 2) on the wavenumber of the incoming radiation. As shown in Equation 53, there is a fourth power dependence on the wavenumber of the incoming radiation. This dependence is considerable, and short–wavelength lasers should be considered if signal intensity is an issue. The ratio between Stokes and anti–Stokes lines for the same vibrational transition, $\nu_i^{as} = \nu_i^s$ and $\nu_f^{as} = \nu_f^s$, is equal to

$$\frac{I_S}{I_{AS}} = \left(\frac{\nu_l - |\Delta\nu(\nu_{vib}, J)|}{\nu_l + |\Delta\nu(\nu_{vib}, J)|}\right)^4 \exp\left(\frac{hc\Delta E_\nu}{k_b T_{gas}}\right). \tag{57}$$

From Equation 57 it is clear how, especially at low gas temperature, it is more convenient to look at the more intense Stokes band. For this very reason, all the data reported in this thesis has been obtained by measuring Stokes bands. However, the ratio decreases exponentially with temperature and, for temperature of the order of 10^3 K it approaches unity. For N_2:

$$\left(\frac{I_S}{I_{AS}}\right)_{T_{gas}=300\,K} \simeq 3\times10^4 \quad \text{and} \quad \left(\frac{I_S}{I_{AS}}\right)_{T_{gas}=3000\,K} \simeq 1.$$

From now on, the discussion will be restricted to Stokes rotational–vibrational Raman only.

In Equation 53, $\Phi(\nu', J)$ is a factor including the two invariants of the vibrational transition polarizability tensor, α and γ, and the Placzek–Teller coefficients. For S, Q and O branches it is equal to

$$\Phi(\nu', J)_S = \frac{7(J+1)(J+2)}{30(2J+1)(2J+3)}\gamma^2(\nu'), \tag{58}$$

$$\Phi(\nu', J)_Q = \alpha^2(\nu') + \frac{11J(J+1)}{45(2J-1)(2J+3)}\gamma^2(\nu'), \tag{59}$$

$$\Phi(\nu', J)_O = \frac{7J(J-1)}{30(2J-1)(2J+1)}\gamma^2(\nu'). \tag{60}$$

These are the factor including the $(\nu+1)$ dependence of the Raman cross section on the vibrational quantum number since

$$\alpha^2, \gamma^2 \propto (\nu+1).$$

Due to anisotropy of the molecular polarizability tensor, for the common case of incoming linearly polarized radiation, the scattered radiation is depolarized by a factor

$$\rho = \frac{I_{\parallel}}{I_{\perp}} = \frac{3}{4}, \tag{61}$$

for linear diatomic molecules. The depolarization is due to the invariant γ of the vibrational transition polarizability tensor only. It is worth noting how it is the Q branch only to have a dependence on α, see Equation 58, Equation 59 and Equation 60. Moreover, by looking at Table 13, $\alpha \gg \gamma$. Consequently, Q branches are slightly depolarized. On the contrary, because of the missing dependence on α, S and O branches are depolarized by a $3/4$ factor.

Molecule	α $[m^4 kg^{-1}(4\pi\epsilon_0)^{-2}]$	γ $[m^4 kg^{-1}(4\pi\epsilon_0)^{-2}]$	α_e $[cm^{-1}]$	B_e $[cm^{-1}]$
N_2	2.62×10^{-14}[112]	4.23×10^{-14}[112]	0.017318[71]	1.99824[71]

Table 13: Spectroscopic constants used for the simulation of rotational–vibrational Raman.

Equation 58, Equation 59 and Equation 60 are applicable when scattered light with both polarizations is collected, as it is the case of this work. For a more detailed discussion on depolarization dependence of $\Phi(v, J)$ the reader is advised to refer to chapters 5 and 6 of [53].

For the sake of using Equation 53 to fit experimental spectra, spectroscopic constants reported in Table 13 are used to calculate ν_{vib} and B as

$$\nu_{vib} = \omega_e - 2\omega_e x_e \left(v + \frac{1}{2}\right), \tag{62}$$

$$B_v = B_e - \alpha_e \left(v + \frac{1}{2}\right). \tag{63}$$

5.2.3 *Ro–vibrational Raman in linear molecules*

Figure 31 shows simulations obtained after convolution of Equation 53 with a Gaussian function, as to mimic the experimental function of a spectrometer.

Spectra show S, Q, and O branches for the fundamental transition $(v^f = 1) \leftarrow (v^i = 0)$ of N_2 at gas temperature equal to 5000 K. S and O branches are a about two orders of magnitude less intense than the Q branch. Moreover, their profile is much broader so as to form a broad band signal, easy to be confused with a background in the presence of experimental noise. For those reasons, experimental spectra are fitted by using Q branches only. Simulations reported in Figure 31 show, for the sake of clarity, contributions coming from one transition only.

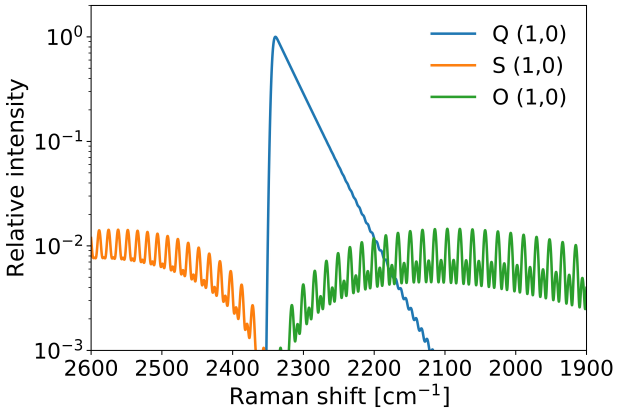

(a) Low resolution simulation of O, Q and S branches. The resolution is set to $6\,\mathrm{cm}^{-1}$.

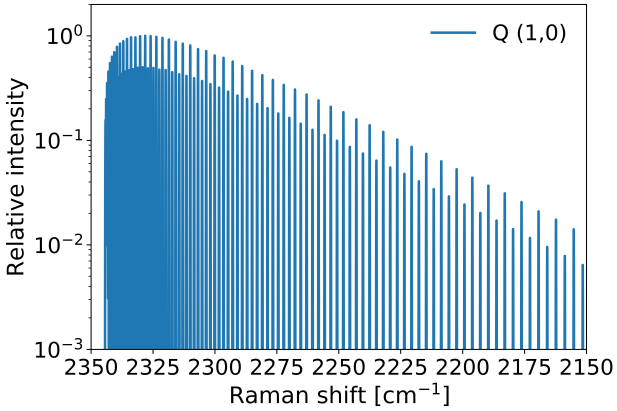

(b) High resolution simulation of the Q branch. The resolution is set to $0.1\,\mathrm{cm}^{-1}$.

Figure 31: Simulation of the rotational–vibrational Stokes Raman spectrum for the transition $(v^f = 1) \leftarrow (v^i = 0)$ of N_2 at gas temperature equal to 5000 K.

Experimentally, all the rotational–vibrational states are probed simultaneously, giving rise to more complex spectra. Major experimental parameters influencing the shape of such spectra are rotational temperature and the distribution of molecules over the vibration manifold. The higher the rotational temperature the broader the Q branch peaks – since more rotational states are populated and the Q branch broadens by the exponential factor in Equation 55. Notice that, due to anharmonicity of the potential, Equation 63 holds, and the broadening appears although $\Delta J = 0$. Conversely, the same does not occur in the case of Cabannes lines [66], for which $\Delta v = \Delta J = 0$, contributing to the Rayleigh scattering.

Figure 32 shows simulations for two relevant vibrational distributions with the aim of highlighting the primary effect of the vibrational distribution in defining a Raman spectrum. An experimental vibrational distribution, measured in a low pressure plasma, is used in

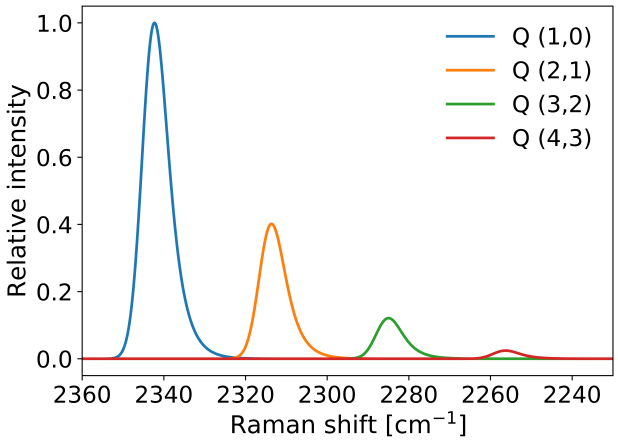

(a) Q branches obtained with a vibrational population equal to
$N_{(0\ to\ 3)}$ = (1., 0.2, 0.04, 0.006)
The resolution is set to 6 cm^{-1}.

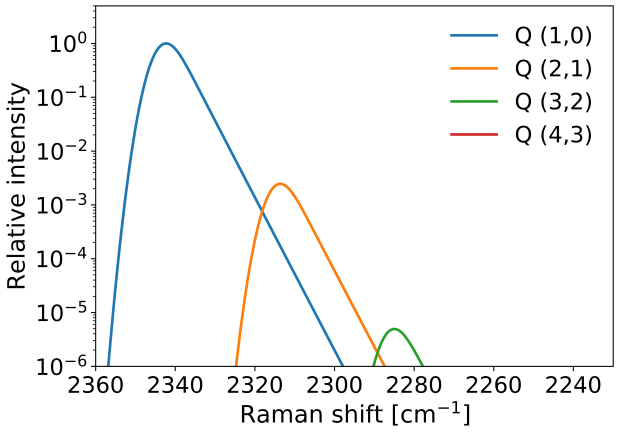

(b) Q branches obtained with vibrational population defined by a Boltzmann distribution at 500 K. The resolution is set to 6 cm^{-1}.

Figure 32: Simulation of the rotational–vibrational Stokes Raman spectrum with contribution of up to 4 vibrational levels of N_2 at gas temperature equal to 500 K.

Figure 32b to present a typical spectrum obtained in a N_2 microwave discharge. For comparison, Figure 32a is obtained by assuming thermal population of the vibrational states at $T_v = T_r = T_{gas} = 500$ K. Although obtained at the same T_{gas}, the difference between the two showcases is striking: vibrational states for which $v > 1$ are mildly populated when the system is in vibrational equilibrium. Selective excitation of the vibrational mode is essential to obtain relevant population of high vibrational states. The conditions for which the vibrational distribution can be so strongly decoupled from T_{gas} have been thoroughly discussed in Chapter 4.

5.3 EXPERIMENTAL SETUP AND DESIGN CONSIDERATIONS

The chief parts of the experimental setup are shown in Figure 34; they include 1) a microwave source, 2) a flowing reactor and 3) the laser scattering diagnostics.

5.3.1 *The plasma reactor*

Continuous wave microwave radiation is delivered by a cavity magnetron (2.45 GHz, power adjustable between 20 W and 1.6 kW). The microwave source is directly connected to a water cooled circulator that is used to absorb the reflected power in order to prevent damage of the source. The emitted microwave radiation is coupled to a rectangular WR–340 waveguide via a three stub tuner ensuring perfect matching to the plasma load. Reflected radiation is measured on the circulator by means of a diode. All the experiments are performed by manually controlling the power delivered by the magnetron and adjusting the three stub tuner to minimize the reflected power. In such conditions, about 100% of the power delivered by the magnetron is supposed to be absorbed by the plasma. The magnetron has been calibrated by measuring the delivered power by means of a calibrated probe connected to a spectrum analyzer. Results indicate that its figure is linear over the entire range of operation, see Figure 33.

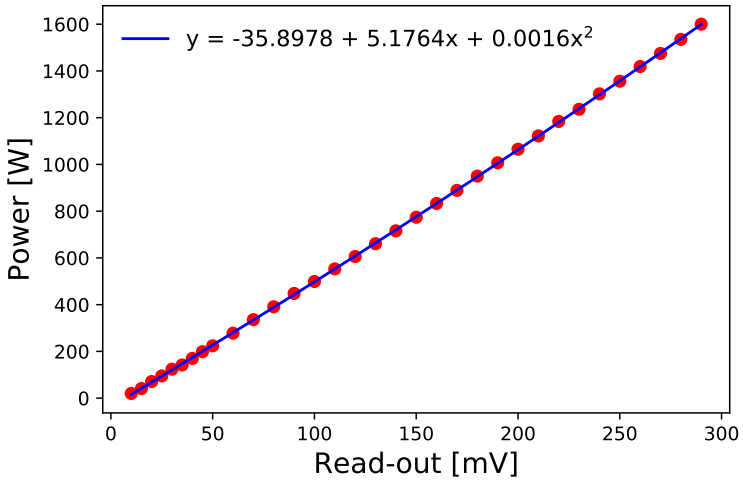

Figure 33: Magnetron calibration. Delivered power is measured by means of a calibrated probe connected to a spectrum analyzer. Values on the abscissa correspond to the read–out of the control knob.

The flowing reactor is composed by a quartz tube (30 mm diameter and 400 mm length) inserted perpendicularly to the waveguide. Such a significant length is necessary to position the downstream glass–to–metal connectors far away from the plasma. This is required to avoid over heating of the o–rings present in the glass–to–metal connectors.

Additional air cooling is used when the reactor is operated at high input power.

The waveguide is short circuited with a sliding short such that a standing wave is sustained in the resulting cavity. The sliding short is positioned at a quarter wavelength distance from the centre of the tube in order to maximize the TE_{10} guided mode at the centre of the tube. A hole of 1″ in diameter has been drilled in the centre of the movable plunger to allow for scattering light to be collected. The section of waveguide where the quartz tube is inserted is shielded by means of a Faraday cage with the goal of blocking any microwave leak and containing the broken pieces of glass in the unlikely event of failure.

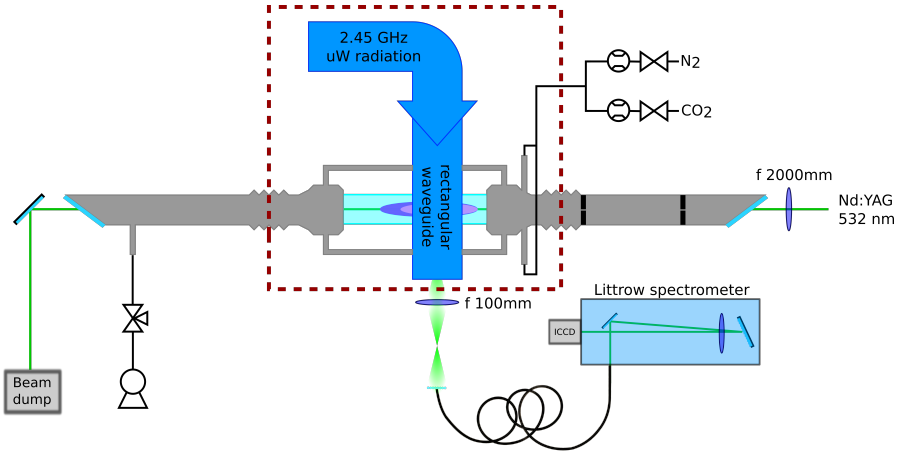

Figure 34: Schematic of the Raman scattering installed at a flowing microwave plasma reactor. The vacuum vessel is composed by two metallic pipes, two bellows, two glass–to–metal connectors connected to one quartz tube. Process gas is injected by means of two tangential injection nozzles connected to the upstream glass–to–metal connector. Exhaust gas is evacuated downstream by a rotary oil pump. The plasma is sustained in the quartz tube by providing microwave radiation through a rectangular WR-340 waveguide. The reactor is secured to the waveguide by means of four metallic poles. The use of flexible bellows allows the reactor and the microwave components, highlighted by the dashed red contour, to slide with respect to the rest of the setup. Axial optical access is provided by the two Brewster windows. A hole in the sliding short (not shown in the picture) permits scattered light to be collected and finally coupled to the spectrometer via a linear fiber bundle.

Process gas is injected 10 cm upstream of the waveguide by using two tangential injection nozzles (bore of 2 mm) to create rotation in the flow. The presence of a swirl flow and a localized energy deposition work synergistically to stabilize the plasma in the centre of the quartz tube. This allow a large amount of energy, that in turn increases the gas temperature, to be deposited in the molecular gas without deteriorating the quartz tube. As it will be shown in the fu-

ture sections, gas temperatures as high as 7000 K are found in the plasma core, with a jacket of colder gas, less than 1000 K, shielding the quartz tube. The reactor is typically operated with flows in the range from 1 slm to 10 slm and, by adjusting the effective pumping speed, pressures in the range from 10 mbar to 800 mbar are obtained.

The vacuum vessel is closed on its axis by input and output Brewster windows that permit the laser to be shined axially thorough the plasma. Such windows are placed as far as possible (about 1.5 m) from the probed region to reduce their contribution to stray light. Additionally, two stainless steel baffles are installed in vacuum to further suppress stray light.

The reactor is built in such a way that radial scans at any axial position are possible to obtain a 2D map of the plasma. The microwave source is then mounted on a linear stage such that it can be translated with respect to the probe laser. The glass–to–metal connectors are connected to the metallic waveguide by means of four metallic poles. As a result, the quartz tube, that is hold in place by the two glass-to–metal connectors, will move with the microwave source as one piece. The glass–to–metal connectors are connected to the two metallic arms by means of two flexible bellows. In the end, it is possible to move the plasma with respect to the laser beam without changing the plasma characteristics. In fact, the quartz tube does not move inside the waveguide. Axial scanning is more easily achievable because of using optical fibres to collect the scattered light. Optical fibres and collection lens are mounted on a ruler that is free to slide on the optical table parallel to the beam axis.

5.3.2 *The diagnostics apparatus*

A frequency doubled ($\lambda = 532\,nm$) Nd:YAG (Continuum Powerlite DLS 8000) laser operated at 4 W, 10 Hz is used to probe the plasma. The beam is guided by a set of dialectic mirrors (EKSMA 052-5306) and then mildly focused with an $f = 2\,m$ lens in the centre of the waveguide, see Figure 34. According to the laser's datasheet the beam full divergence is equal to 0.45 mrad. By recalling that the product between the image radius and the ray incident angle is a invariant for a system of lenses, the beam waist at the focal point can be calculated as $h_2 = 2\theta_1 f$, where θ_1 is the half divergence of the beam and f is the focal length. For this specific case the beam waist is equal to 900 µm. This value represent the spatial (radial) resolution of the apparatus.

The beam is shined axially in the reactor. Before encountering the plasma it travels thorough the two metallic apertures for stray light suppression. In the end, it exits the reactor through the exit Brewster window to be reflected by a mirror on a beam dump. The laser beam is polarized perpendicularly to the optical plane and so the scattered light has to be collected on the optical plane. In order to minimize

stray light, it is collected at 90° with respect to the laser beam axis. An achromatic doublet (f = 100 mm) is used to project a 1:1 image onto a linear fibre bundle. A substantial amount of scattered light is not coupled to the fibers since their diameter is about half of the beam waist. A further improvement on this side would be to expand the beam before the focusing lens such that its divergence decreases inversely with the magnification factor, therefore decreasing the beam waist. Such a fibre bundle is composed by $27 \times 400\,\mu m$ fibres linearly arranged.

The fibre bundle illuminates an in–home built Littrow spectrometer characterized by (f = 1 m, dispersion of $0.85\,nm\,mm^{-1}$, f# = 10) equipped with an iCCD. Another advantage of using fiber coupling is the possibility of avoiding the use of a input slit in the spectrometer. If on one hand this prevent any easy variation of the slit function, since it is fixed by the diameter of the fibers, on the other one it permits to build a more minimal spectrometer. In fact, no additional lenses are needed to couple the collected light to the spectrometer, provided the light is collected at the right f# by the collection lens.

Spectra are imaged on a PI-MAX4 emICCD equipped with a square $512 \times 24\,\mu m$ electronically cooled CCD. This allows 27 fibers to be simultaneously imaged on the CCD, therefore covering an axial range of about 12 mm. This relatively large axial covering allows one to either directly obtain an axial profile of the spectral information or, as in this case, bin the signals coming from all the fibres in order to increase the signal to noise ratio (SNR). Given the linear dispersion of the spectrometer ($0.85\,nm\,mm^{-1}$) the field of view is as large as 10 nm. This is sufficient to simultaneously detect up to eight vibrational bands in the case of N_2.

Rayleigh scattering constitutes the strongest source of scattered light. As compared to Raman, it is about three orders of magnitude more intense and it is found at the laser wavelength – no energy shift is induced in the Rayleigh process. For this reason, a long pass filter with cut–off wavelength of 550 nm (ThorLabs FGL550) is placed in front of the collection fibres to block scattered light at the laser wavelength. More sophisticated techniques would have to be implemented if rotational Raman scattering [46], or Thomson scattering [64], were the signals to measure.

The diagnostics is calibrated by varying the N_2 pressure in the reactor kept at room temperature. The expected linear behaviour as function of the number density is obtained, see Figure 35.

5.4 EXPERIMENTAL PROCEDURE AND DATA ANALYSIS

Experiments have been performed on the plasma in steady state conditions, stable for a period of time much larger than that needed for spectra acquisition, and with the laser operated in freerun mode. In

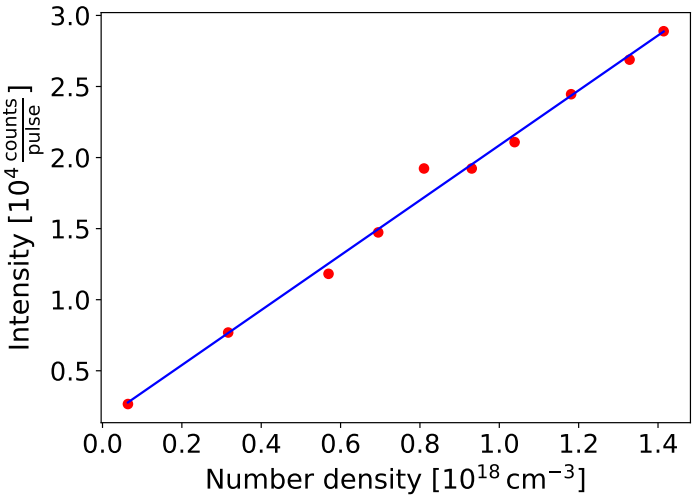

Figure 35: Calibration curve obtained by varying the (N_2) pressure in the reactor, kept at room temperature. The laser is operated at full power (4 *W*), the image intensifier at 90% of its maximum gain and 3000 accumulations are acuired for each spectra.

this configuration, the camera is triggered by the laser. Images are acquired with the camera in accumulation mode with the CCD always active and multiple scattering events being impressed on it. Working in accumulation mode limits the camera readout noise to the minimum.

From Equation 53 it can be noticed how the profile of a Raman Q branch is a function of the rotational temperature (T_r) and of the rotational constants (B_{v^i}) of the two vibrational levels involved in the scattering process. Note that T_r is considered to be constant regardless of the vibrational state. The instrumental broadening of the spectrometer (Gaussian, FWHM = 6.5 cm^{-1}) is determined by fitting a spectrum measured in neutral N_2 at room temperature.

Synthetic spectra are calculated by using Equation 53 for each detected peak. The fitting parameters are then the heights of the individual Q branches and the rotational temperature. Q branches, as calculated by using Equation 53 with the fitted heights and T_r, are integrated to obtain a value proportional to the population of each vibrational level and to the collection efficiency of the apparatus. The relative (to ground state) populations are then calculated as:

$$\frac{N_v}{N_0} = \frac{\int Q_v(\tilde{\nu})\,d\tilde{\nu}}{\int Q_0(\tilde{\nu})\,d\tilde{\nu}} \cdot \frac{1}{v+1}, \tag{64}$$

where N_0 and N_v are the populations of the ground and of a generic vibrational level, respectively, and the integrals are calculated over the fitted Q branches. In the formula, the $(v+1)$ factor corrects for the dependence of the Raman scattering cross section on the vibrational quantum number, as contained within the polarizability γ_{v^i} in

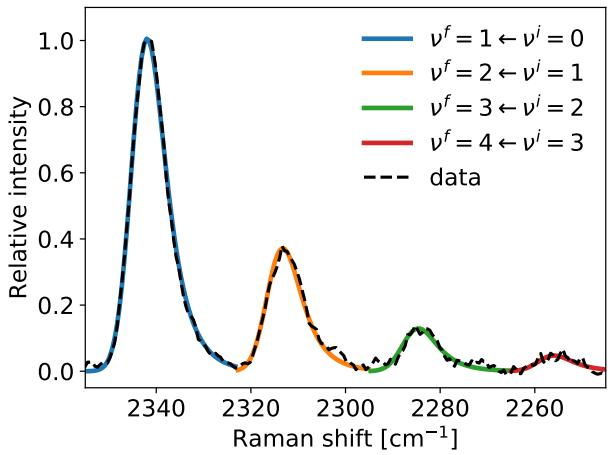

(a) Spectrum obtained in a 50 mbar, 130 W N_2 plasma. Fitted T_r = 550 K.

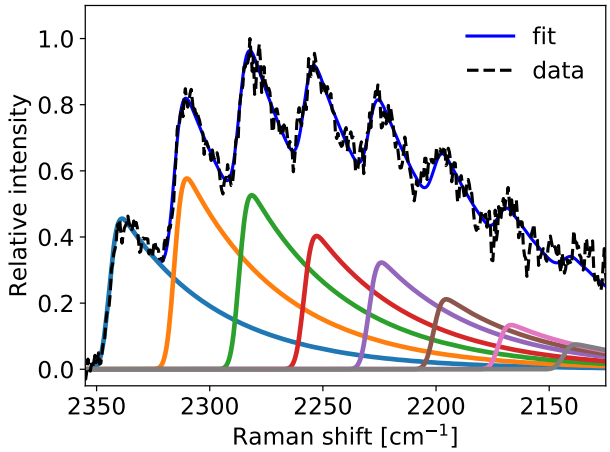

(b) Spectrum obtained in a 800 mbar, 330 W N_2 plasma. Fitted T_r = 7000 K.

Figure 36: Fit of vibrational Raman spectra measured at different reactor conditions. The effect of T_r is evident with Raman Q branches that broadens as T_r increases. The thin solid blue line is the experimental data the fit of which is reported as a dashed black line. Individual fitted Q branches, the sum of which gives the total fit, are depicted in colored solid lines.

Equation 53. In conclusion, the fit outcomes are 1) the rotational temperature T_r and 2) the relative (to ground state) populations of the vibrational levels. An example of experimental and fitted spectra is shown in Figure 36.

5.5 ASSESSING THE VIBRATIONAL NON–EQUILIBRIUM

This section presents the results obtained on the investigation of vibrational non–equilibrium in a N_2 microwave flowing reactor.

5.5.1 *Investigated plasma*

The investigation is carried out to study the effect of processing parameters, like pressure (P), flow (Φ) and input power (Q), on the extent by which the vibrational non–equilibrium is found in the microwave plasma.

P [mbar]	Φ [slm]	Q [W]	SEI [$eV\,molecule^{-1}$]
17	7.8	130	0.22
50	7.8	130	0.22
50	10	130	0.17
800	7.8	330	0.56

Table 14: Experimental conditions for the investigated plasma. Pressure is measured at the pump's mouth by means of a Edwards ASG21000 vacuum gauge.

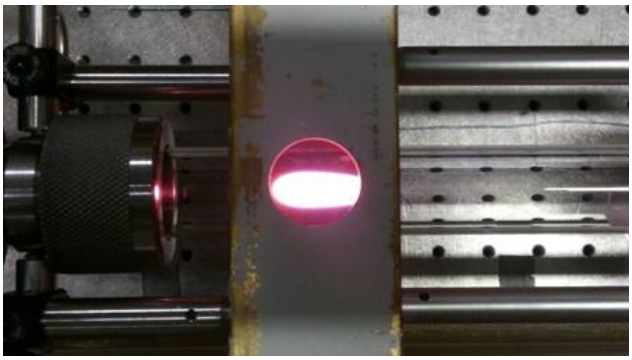

(a) Picture of a N_2 discharge operated at 50 mbar

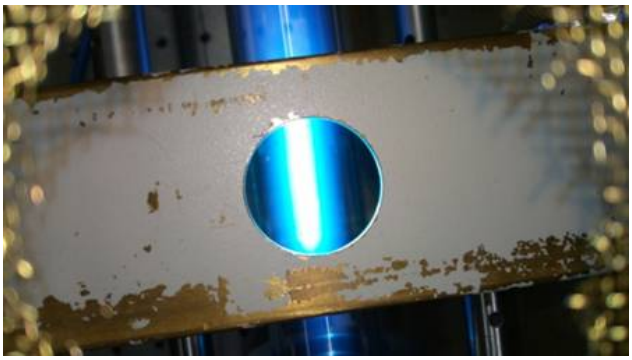

(b) Picture of a CO_2 discharge operated at 600 mbar

Figure 37: Pictures of the microwave plasma operated at low, 50 mbar, and high, 600 mbar, pressure. The two pictures illustrate the plasma when different process gases are used; similar effect would be obtained when pressure only is changed.

Parameters shown in Table 14 are chosen so as to cover all the regimes; namely high and low collisional rates, high and low energy density. Parameters for the first and second measurements are selected to keep the specific energy input (SEI) constant at $0.22\,eV\,mol^{-1}$. At this relatively low pressure the non–equilibrium is expected to be the highest, as collisionality linearly decreases with pressure. For a pressure of $50\,mbar$, a value low enough to see a noticeble non–equilibrium behaviour and high enough for the diagnostics to yield data with good SNR, two different mesurements are performed to investigate the effect of lowering the SEI to $0.17\,eV\,mol^{-1}$. Finally, the last aims to show a high pressure case that could be sustained with a higher SEI = $0.56\,eV\,mol^{-1}$.

Pressure changes the plasma appearance in a remarkable way, see Figure 37. At the lower pressures, the plasma is observed as diffuse, filling a large portion of the discharge tube. Conversely, when the reactor is operated at high pressure, the plasma is more confined in the centre of the tube – where the microwave standing wave is at its maximum. Both regimes were observed in CO_2 microwave plasmas [35] also.

5.5.2 *Radial measurements*

In this section, we firstly present the radial profiles of T_r and $T_{v(0,1)}$ as measured from the ro–vibrational spectra. The ratio $T_{v(0,1)}/T_r$ is then chosen as indicator of the vibrational non–equilibrium and radial profiles are calculated.

Afterwards, the investigation of energy loading into rotational, translational and vibrational modes of the molecules is presented. Concerning the vibrational mode, the occupancy of each vibrational level is inferred from the spectra. Subsequently, the anharmonic oscillator formula is used to calculate the energy stored in the vibrational mode. Finally, the measured energy densities are compared to the SEI to estimate the energy loading efficiency of the microwave flowing reactor.

Radial profile of T_r are reported in Figure 38. T_r is the outcome of fitting a set of Q branches, singularly described by Equation 53, to the measured spectra. It is obtained from the slope of the vibrational bands, as included within the exponential factor in Equation 53. T_r is assumed to be constant among different vibrational levels and the variation of the rotational constant B as a function of v is included in the fit.

T_r as defined by Equation 53 describes the distribution of energy among the rotational levels. Such a temperature is conceptually different from the gas temperature T_{gas}, that is associated to the energy of translations. However, the two temperatures can generally be considered in equilibrium. The reason is the very fast rotational–translational relaxation. It increases with pressures, as the number of

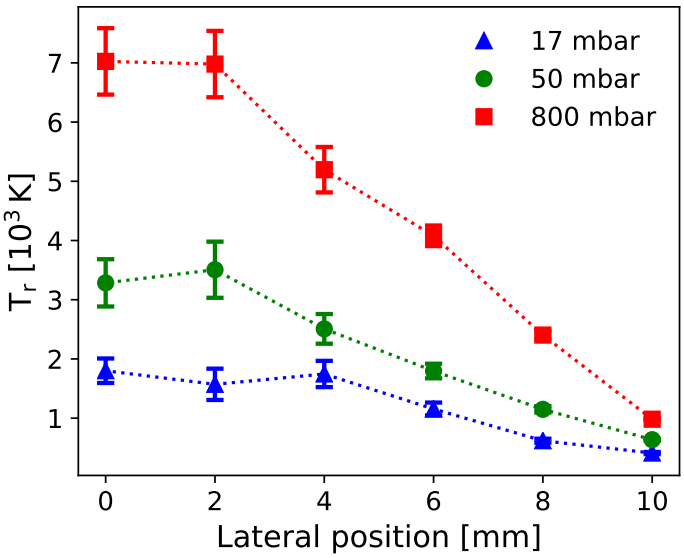

Figure 38: Radial profiles of rotational temperature T_r. T_r is calculated from the slope of the ro–vibrational Q branches fitted by using Equation 53.

collisions increases, and with T_{gas}, since such an inelastic process is favoured by high energy collisions. For the specific case of N_2, 10^0 to 10^1 collisions, in a range of T_{gas} from 10^2 K to 10^4 K, are sufficient to equilibrate the rotational distribution to the translational temperature [75]. T_r gradually declines from the centre to the wall for all the three measurements. Curves for the low pressure measurements show values that are about half of those of the high pressure data uniformly in all positions.

When vibrational levels are in Boltzmann equilibrium with each other, a single vibrational temperature suffices to describe the population density of all the vibrational levels. Conversely, if some active vibrational pumping mechanism is at play, for example energy transfer via electron collisions or vibrational energy transfer within the vibrational manifold, a single temperature does not suffice to describe the vibrational energy distribution. Although that is the case, a single temperature can still be useful to describe the energy distribution in the vibrational mode. Since microwave plasmas can be out of equilibrium, and regardless that up to 8 vibrational levels are measured, the definition of Equation 49 is nevertheless used for the calculation of the vibrational temperature $T_{v(0,1)}$.

The larger T_r the more rotational levels are populated. As a result, the measured Q branches broaden according to Equation 55. High T_r found in the core of the plasma acts by increasing the overlap of the vibrational bands and by decreasing the signal to noise ratio. For this reason, experimental errors generally increase for measurements taken in the central region of the reactor. However, with the devel-

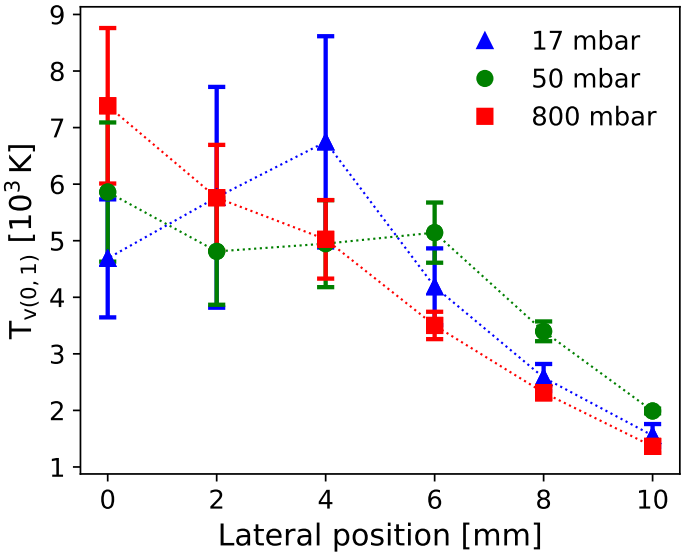

Figure 39: Radial profiles of vibrational temperature $T_{v(01)}$. Is is calculated from the relative populations of the ground and first vibrational levels by using Equation 49.

oped diagnostics, T_r spanning over more than an order of magnitude, from 500 K to 7000 K, and up to 8 vibrational levels, at pressures from 17 mbar to 800 mbar, could be successfully measured.

Similarly, vibrational temperature profiles are reported in Figure 39. From this figure it can be seen that values for the high pressure measurement increase steadily from the edge to the centre. Conversely, a different trend is observed for the low pressure measurements where $T_{v(0,1)}$ is almost flat from 0 mm to 6 mm.

A metric is introduced to summarize the non–equilibrium between $T_{v(01)}$ and T_r. The departure from equilibrium is investigated in terms of the ratio $T_{v(01)}/T_r$. Radial profiles shown in Figure 40 have a different behaviour for the high power high pressure plasma condition and two low power low pressure ones. In the former, $T_{v(01)}/T_r$ is always close to unity, identifying a thermal regime, for the entire range. Conversely, in the two other cases it is always larger than unity, increasing from 2 to 4 from the centre towards the edge of the plasma. A $T_{v(01)}/T_r = 4$ is considered to be a conservative threshold for a significant influence of the vibrational excitation [110]. Indeed, measurements reported in Figure 40 are very close to satisfy this requirement for the two low pressure cases. Consequently, a strong indication is found that vibrational non–equilibrium can be sustained – with significant influence of the vibrational excitation – close to the wall of the microwave flowing reactor, provided favourable plasma conditions.

By comparing T_r and $T_{v(0,1)}$ profiles in Figure 38 and Figure 39, respectively, it can be noticed that similar $T_{v(01)}$ values are obtained for both low and high pressure plasma, while T_r values are much higher

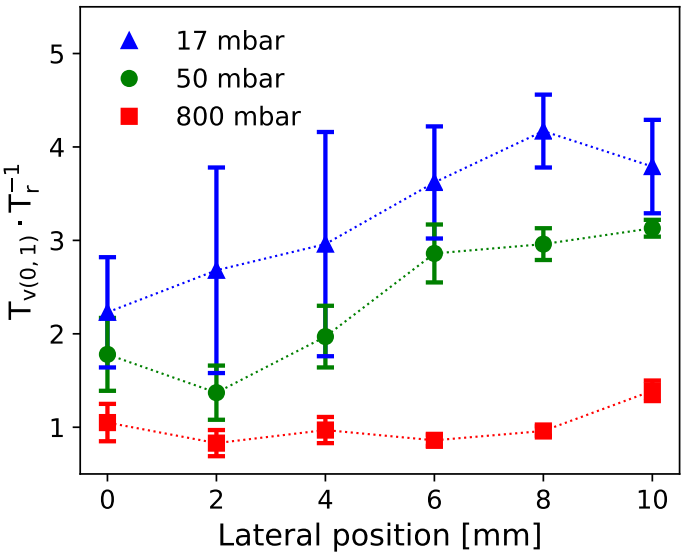

Figure 40: Radial profiles of $T_{v(01)}/T_r$, the chosen indicator of vibrational non–equilibrium.

at high pressure. This suggests that pressure is not the bottleneck for the microwave source to excite molecular vibrations. However, large VT rates at high pressure remarkably increase T_r. As a result, strong vibrational non–equilibrium can be found at sufficiently low pressure only, for values of T_r lower than about 10^3 K.

5.5.3 *Axial measurements*

Radial profiles showed in the previous Section 5.5.2 are good for understanding the behaviour of the plasma as the source of molecular excitation, but no information is provided concerning what happens after the gas leaves the active region. In the light of possible industrial implementation of the investigated plasma source, it is of a paramount importance to understand what are the dynamics in the downstream. The region in the effluents close to the waveguide is actually where the activated gas is more likely to interact with other substances, e.g. catalysts or additional molecular gas. For this reason, radial measurements are extended downstream to obtain axial profiles with the reactor operated as follows: 50 mbar, 10 slm and 120 W.

Figure 41 displays an axial profile with measurements taken in the radial centre of the tube. Up to three vibrational levels are shown in Figure 41 for a considerable distance of 160 mm. This is expected because at this gas temperature, 500 K, and pressure, 50 mbar, VT energy transfer rates from $v = 1 \rightarrow v = 0$ is very low of the order of 10^{-5} s^{-1} [7] while the residence time of a given molecule is only 6×10^{-2} s (assuming plug flow at 10 slm in a pipe with diameter of

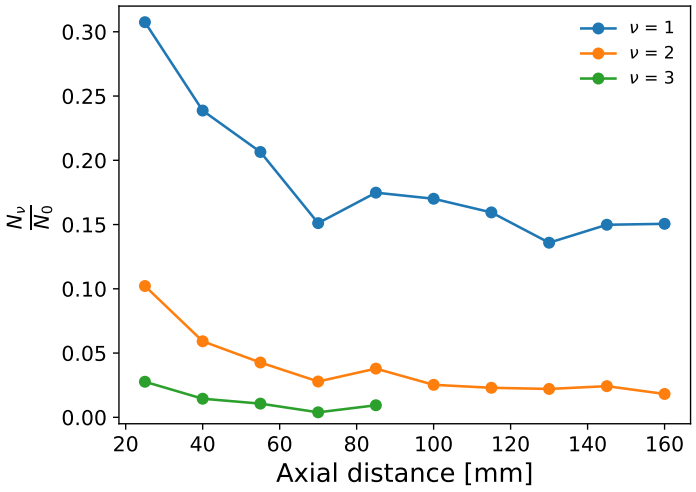

Figure 41: Axial position is measured as relative to the waveguide's plate facing the effluents and every point is the result of binning over a laser chord of 15 mm in length. Measurements are taken in the radial centre of the quartz tube. Up to four vibrational levels are detected in the first region close to the waveguide to then reduce to two as we move further downstream. Values are normalized to N_0, not shown in the graph.

300 mm and length 160 mm. As compared to the number of vibrational levels detected in the core of the plasma, see Figure 43, few are now detected. This observation suggests strong gas mixing to be at play.

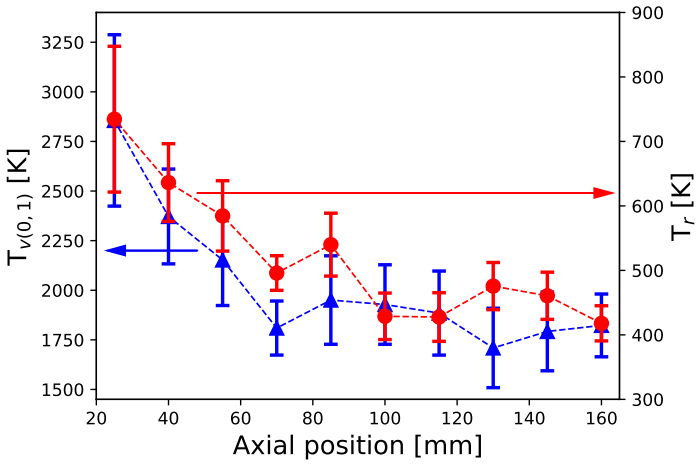

Figure 42: Axial profiles of vibrational and rotational temperatures as the reactor is operated as follows: 50 mbar, 10 slm and 120 W. Axial position is measured as relative to the waveguide's plate facing the effluents and every point is the result of binning over a laser chord of 15 mm in length.

Figure 42 shows the axial variation of T_r and $T_{v(0,1)}$. A closer look to it reveals a two step behaviour in the $T_{v(0,1)}$ axial profile, with a

steep decrease of approximately $20\,\mathrm{K\,mm^{-1}}$ from 20 to 70 mm followed by a (within experimental sensitivity) constant profile extending till 160 mm. This effect can be explained by the fact that VT relaxation rate exponentially increases with gas temperature as predicted by the Landau–Teller formula [48], see Chapter 4.

Decay profiles of T_r and $T_{v(0,1)}$ are alike, because gas mixing similarly cools down both distributions. It is interesting to notice how a region with favourable conditions is formed in the downstream where the vibrational temperature remains constant at about 1800 K while and the rotational temperature shows much smaller values of about 400 K – displaying a strong decoupling between vibrational and rotational dynamics.

5.5.4 *Local energy efficiency*

In order to quantify the efficiency by which the plasma loads energy into molecular vibrations, a detailed investigation that compares, locally and globally, the amount of energy stored in vibration with respect to the SEI, is needed. Data reported in Figure 40 is suitable to display the local degree of non–equilibrium, but it does not suffice to the quantification of the energy efficiency. From now on, we do not restrict ourselves on the relative populations of the first two vibrational levels only, but we go further by taking now into account also energy contribution for higher vibrational states.

In Figure 43, relative populations of up to $v = 7$ vibrational level are reported for a set of radial positions at three different plasma conditions. The information presented in this plot will be extensively used in the following to calculate $T_{v(0,1)}$ and energy distribution. Nevertheless, the spatial character of a plasma can already be appreciated. In the constricted mode case the slope of the distribution varies more gently from the edge to the centre, showing a gentle increase of the vibrational temperature. Conversely, lines obtained in the range 0 mm to 6 mm are clustered together in the low pressure measurements, which means they have a similar $T_{v(0,1)}$, and only two lines in the 8 mm to 10 mm region are clearly distinguishable from the others. This displays a larger region with a homogeneous vibrational temperature typical of a diffused plasma.

Population distributions obtained on the edges of low pressure microwave discharges goes even beyond what a Treanor distribution would predict by using the measured rotational and vibrational temperature (see dashed lines on Figure 43). This is most probably due to the presence of an electron pumping mechanism with a wide range of energy that simultaneously excites multiple vibrational states. In Figure 43(c) the data shows underpopulated high vibrational levels in the centre of the discharge as compared to the Treanor distribution calculated in that position; this can be attributed to dissociation.

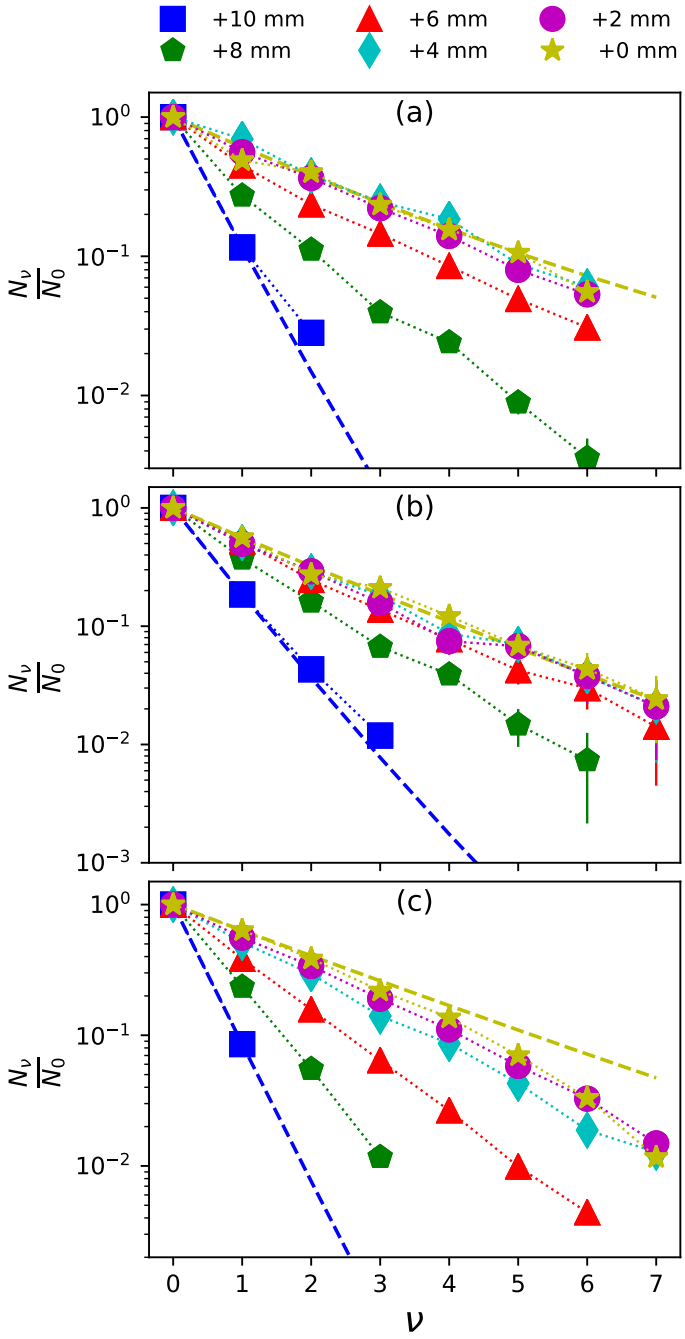

Figure 43: Plots of relative populations of the vibrational mode for three plasma conditions: panel (a) is for the the 17 mbar plasma, (b) 50 mbar and (c) 800 mbar. Each line represents a measurement taken at a different radial position, measured from the centre of the quartz tube (inner diameter = 27 mm). Dashed lines indicate Treanor distributions calculated at +10 mm and at +0 mm by using the measured T_r and $T_{v(0,1)}$.

In the following a quantification of the efficiency by which the microwave flowing reactor is able to transfer energy to the molecular gas is presented. For this purpose, the average energy present in vibrational and rotational–translational modes is firstly quantified. Afterwards, the average energy is corrected for the local number density at every radial position in the plasma. This allows to define an effective energy density that, when compared with the SEI, yields information on the vibrational and rotational–translational energy loading efficiencies.

The fractional vibrational energy is calculated as

$$E_v = n_v \cdot E(v), \tag{65}$$

where $n_v = \frac{N_v}{\sum_i N_i}$ is the fraction of molecules present in the vibrational state v and $E(v)$ is the energy of the vibrational state v calculated with a third order approximation of the anharmonic oscillator formula. Figure 44 displays the radial profile of the fractional vibrational energy. From this picture it is now clear the extend by which energy is present in vibrational levels higher than $v = 1$.

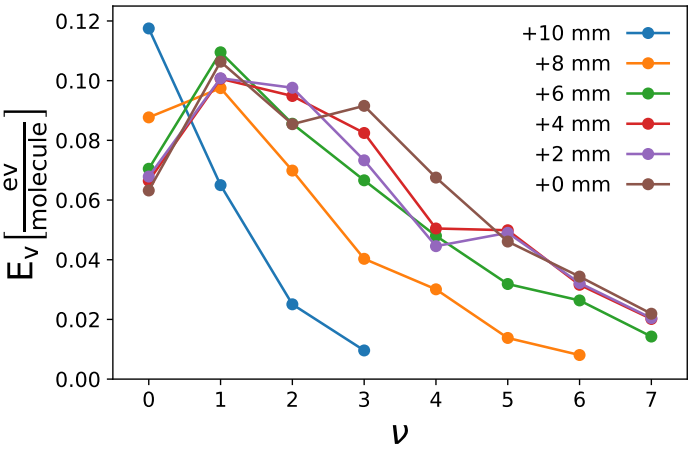

Figure 44: Fractional vibrational energy measured at different radial positions within the microwave plasma operate at: 50 mbar, 7.8 slm, 130 W, SEI = 0.22 $eV\,molecule^{-1}$. From left to right different lines compose a radial scan from the edge toward the centre.

Graphs as the one shown in Figure 44 are obtained for every plasma setting and the distribution of the fractional vibrational energy is presented as a function of radial position. Although Figure 43 shows that relative populations decrease by order of magnitudes, the energy content of each vibrational level increases steadily as predicted by energy spacing of the anharmonic oscillator. As a result, the energy stored in high vibrational states appears not to be negligible. This can be appreciated by calculating the contribution of high vibrational states to the total vibrational energy. Since vibrational distributions

do not follow a Treanor distribution, it has to be quantified from the measured spectra. Data shown in Equation 65 indicates that

$$\left(\frac{\sum_{v>1} E_v}{\sum_v E_v}\right)_{+10\text{ mm}} \simeq 0.15,$$
$$\left(\frac{\sum_{v>1} E_v}{\sum_v E_v}\right)_{+0\text{ mm}} \simeq 0.65,$$

In equilibrium conditions the average energy is the sum of rotational, translational and vibrational degrees, and each degree of freedom contributes $\frac{1}{2}k_b T$. However, in non–equilibrium conditions there is no unique temperature for all modes. Moreover, a unique vibrational temperature could not be assigned to any of the vibrational distributions measured. Hence we adopt the following procedure to calculate the average energy deposited by the plasma. The average deposited vibrational energy is directly obtained from the Raman spectra by including contributions from all the vibrational states. It is equal to:

$$\langle E_v(r)\rangle = \sum_i E_i(r) - E_v(T_{rt}), \tag{66}$$

where $E_i(r)$ (i is over all measured vibrational states) is calculated by using Equation 65 for each radial position r. The vibrational energy $E_v(T_{rt})$ of a gas in thermal equilibrium at room temperature $T_{rt} = 293\,K$ is subtracted from the measured vibrational energy to account for the vibrational energy of the gas at room temperature. This allows to directly quantify the energy deposited by the plasma.

A similar procedure is performed to obtain the deposited rotational–translational energy

$$\langle E_{r,t}(r)\rangle = \frac{5}{2}k_b(T_r(r) - T_{rt}), \tag{67}$$

calculated from the equipartition theorem, with three modes of translation and two modes of rotation accounting for the $\frac{5}{2}$ factor, by using the measured local rotational temperature $T_r(r)$.

The quantities $\langle E_v(r)\rangle$ and $\langle E_{r,t}(r)\rangle$ represent the average energy per molecule deposited by the plasma; they are not suitable, in this form, for a comparison with the SEI as no information on the local number density is included. In order to include that information, the local number density is retrieved from the intensity of the vibrational Raman spectra which varies linearly with the number density, see Equation 53. The local number density is be then given by:

$$N(r) \propto \sum_v \frac{A_v}{v+1}, \tag{68}$$

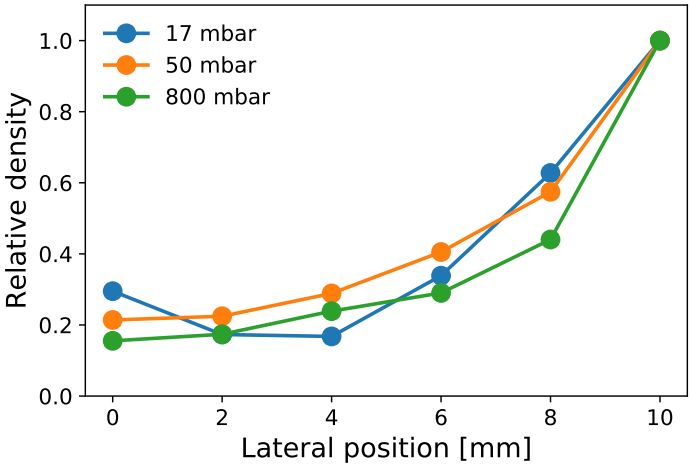

Figure 45: Normalized density profiles as calculated from the intensity of the Raman spectra by using Equation 68.

where the area (A_ν) of each vibrational band is divided by ($\nu + 1$) to take into account the ν dependence of the scattering cross section. Normalized number density profiles, as calculated by

$$\rho(r) = \frac{N(r)}{\max(N(r))} \tag{69}$$

are shown in Figure 45. It is worth pointing out that to obtain a measure for number density this method is insensitive to gas temperature variation. This is because the contributions of all vibrational levels, normalised by the corresponding cross sections (see Equation 64), are included in the calculation without making any assumption on the vibrational distribution. If rotational Raman ($\Delta\nu = 0$) is used, such a calculation becomes intractable as rotational transitions from several vibrational levels add to the measured intensity at almost the same Raman shift. A similar argument can be extended to Rayleigh measurements [65] [26], since light scattered from different vibrational states would eventually contribute to the same peak [39], or even for vibrational Raman when multiple modes are present like in CO_2 [117] [108]. Therefore, in contrast to these other techniques, vibrational Raman in N_2 requires no a–priori assumption about the vibrational distribution to calculate local number density.

With the aim of calculating a power balance, the local number density ρ (see Equation 69) is used to weight the local energy–per–molecule. The effective deposited energy densities are then calculated as:

$$U_\nu(r) = \langle E_\nu(r) \rangle \cdot \rho(r) \tag{70}$$

$$U_{r,t}(r) = \langle E_{r,t}(r) \rangle \cdot \rho(r). \tag{71}$$

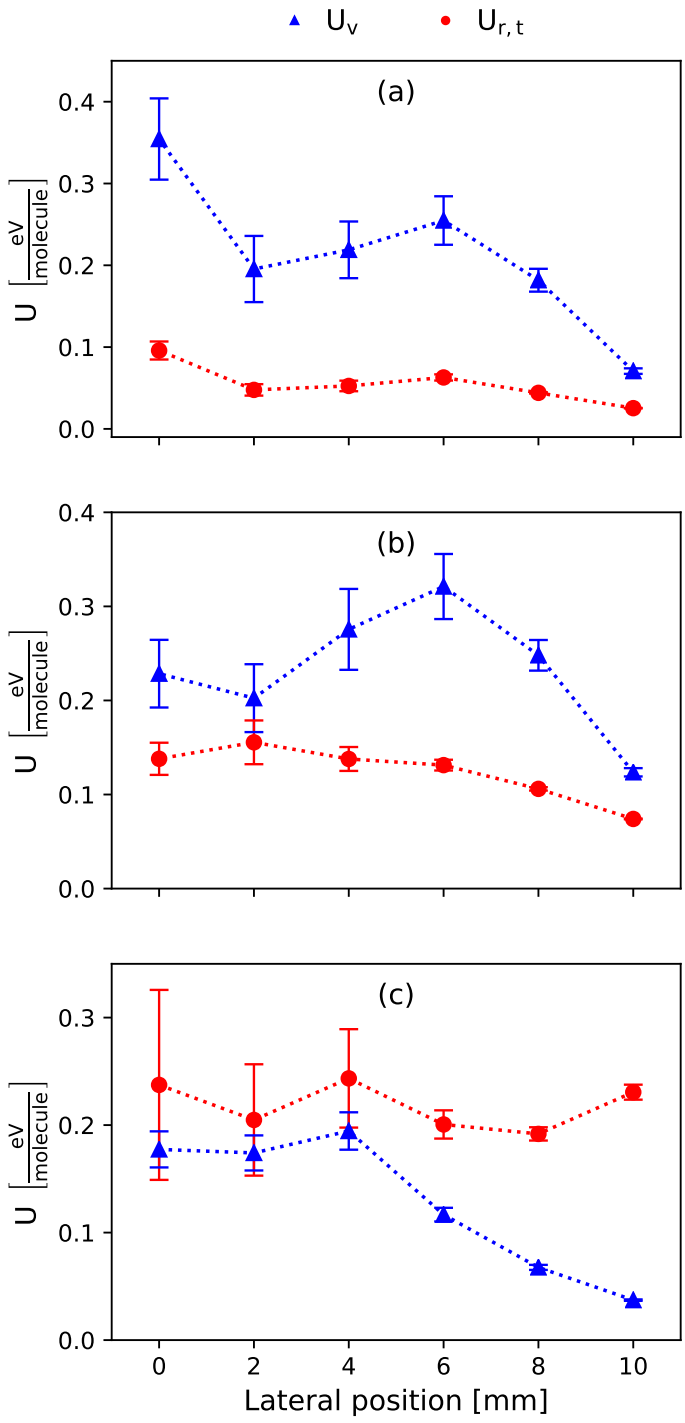

Figure 46: Vibrational and rotational deposited energy densities (see Equation 70 and Equation 71) measured for (a) 17 mbar, 7.8 slm, 130 W, (b) 50 mbar, 7.8 slm, 130 W, (c) 800 mbar, 7.8 slm, 330 W plasma.

Results are shown in Figure 46. For the two low pressure plasmas (17 mbar and 50 mbar) the deposited vibrational is larger than the rotational–translational one, for every radial position. Additionally, it is definitely higher than what would be found in a gas at thermal thermal equilibrium with a temperature equal to the local T_r. For comparison, $\langle E_{r,t} \rangle = 2.5 \langle E_v \rangle$ for N_2 in thermal equilibrium – provided $kT_r > E_1$, where E_1 is the energy of the $v = 1$ vibrational state. An opposite trend is found for the high pressure plasma. The two deposited energy densities are similar in the central region. Close to the reactor walls, the vibrational energy density is smaller than the rotational–translational one.

Although the radial profiles shown in Figure 46 provide information on the radial distribution of energy within the plasma, it does not provide the complete picture, as energy deposition from the plasma occurs over a length much longer than what the laser probes. Consequently, the local measurement presented here cannot account for all the deposited energy, For a complete analysis additional processes like ionisation, dissociation, energy loss via the quartz tube and radiation should be taken into account.

5.5.5 *Overall energy efficiency*

In contrast to measurements performed inside the waveguide, the downstream measurements should account for all the energy absorbed by the gas. Therefore, they can be more reliably used to quantify the energy efficiency of the microwave reactor to the internal energy of the effluents, since in this case molecules in the scattering volume have already passed throughout the entire waveguide.

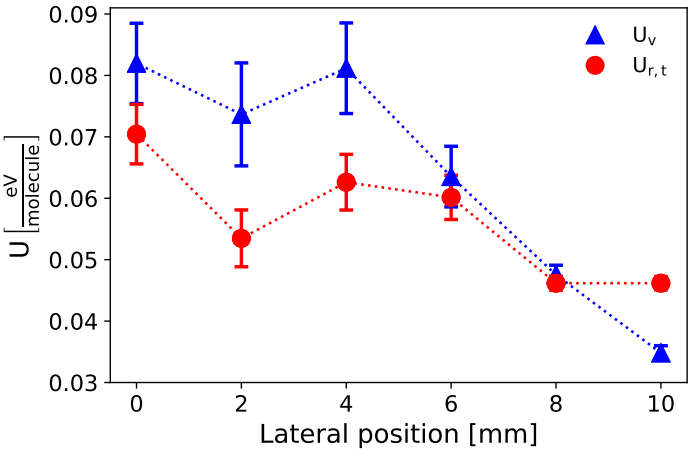

Figure 47: Radial profiles of vibrational and rotational excess energies (see Equation 66 and Equation 67) measured 25 mm after the waveguide for 50 mbar, 10 slm and 120 W.

Figure 47 shows the radial energy distribution of the gas right after having passed throughout the microwave discharge. A striking difference between this profile and that measured in the waveguide for a similar plasma condition, see Figure 46(b), is the location of its maximum. In the former, the maxima of both U_v and $U_{r,t}$ are found in the centre of the tube while in the latter they are found on the edge. This effect may suggest that strong gas mixing is occurring, redistributing energy (and molecules) along a cross section of the quartz tube. Averaging over the tube cross section is done as follows:

$$\langle U_v \rangle = \frac{\int_0^R \int_0^{2\pi} U_v(r)\rho(r) r \, dr d\theta}{\pi R^2}, \tag{72}$$

$$\langle U_{r,t} \rangle = \frac{\int_0^R \int_0^{2\pi} U_{r,t}(r)\rho(r) r \, dr d\theta}{\pi R^2}. \tag{73}$$

By averaging radially the values for U_v and $U_{r,t}$ it is possible to compare such quantities with the SEI. Two assumptions are made that both the energy deposition profile and the molecules' axial velocity do not vary as function of the radial position. The comparison with SEI then yields

$$\frac{\langle U_v \rangle + \langle U_{r,t} \rangle}{SEI} = 0.48, \tag{74}$$

so 48% of the SEI is deposited in the molecular gas as internal energy. Concerning vibrational energy only

$$\frac{\langle U_v \rangle}{SEI} = 0.23, \tag{75}$$

it is found that 23% of the SEI is deposited in the vibrational mode. These values have been calculated by extrapolating the measured temperatures and density to the reactor walls – experimental data is available till $r = 10\,mm$ while the inner radius of the tube is $R = 13.5\,mm$.

5.6 CONCLUSIONS AND OUTLOOK

Vibrational Raman scattering has been implemented as a diagnostic which simultaneously measures number density of reactants, rotational and vibrational temperatures to investigate the nonequilibrium character of the N_2 microwave plasmas.

High values of $T_{v(0,1)}/T_r$ are found on the edges of the plasma in the case of low pressure low input power where $T_{v(0,1)}$ equilibration rate is slower than T_r one. Conversely, at high pressure the plasma appears to be close to thermal equilibrium, showing values of $T_{v(0,1)}/T_r$ close to unity. Additionally, a careful analysis of the local energy density is carried out for vibrational (U_v) and rotational–translational ($U_{r,t}$) loaded energies. The presence of two distinct regions is observed in the low pressure case where the core of the plasma is char-

acterised by a lower energy density, due to the relatively low number density, while most of the energy added by the microwave plasma is confined in the outer shell close to the reactor walls. At low pressure U_v is always higher than what it would be if the gas was found in thermal equilibrium at the measured rotational temperature. Moreover, $U_v > U_{r,t}$ for the lowest investigated pressure. Conversely, the analysis of the energy distribution for the case of the high pressure plasma displays its quasi thermal character, confirming the results obtained by using $T_{v(0,1)}/T_r$.

The reactor is also investigated in the downstream where the gas has completely passed through the microwave discharge assuring a complete energy deposition. Radial measurements now show an opposite trend compared to what obtained in the centre of the discharge: most of the energy is now located in the centre of the tube. This finding suggests that strong gas mixing is at play by effectively redistributing energy and particles over the entire tube cross section, which is likely the result of vortex flow dynamics. Calculations show that right after the waveguide 48% of the SEI is deposited in the molecular gas as rotational, translational and vibrational energy. Concerning vibrational energy only, it is found that 23% of the SEI is stored in the vibrational mode, displaying the ability of the microwave flow reactor to load electric energy in N_2 vibrations.

This investigation of energy loading efficiency into the internal modes of N_2 in the microwave flowing reactor paves the way for a set of future studies. Especially the indication that the effluents retain a relevant amount of SEI into the vibrational mode, at $T_r \simeq 500\,K$, suggests the feasibility of vibrationally enhanced chemical reactions, with possible application of catalytic materials. For example, such an apparatus can be used to evaluate the the synthesis of NO or CO when O_2 or CO_2 are admixtured to the effluents, with the microwave flowing reactor used as a source of vibrationally excited N_2. Moreover, the applicability of the diagnostics is not limit to N_2 only, but can be extended to any gas that shows Raman activity. Specifically, the processing of other gases of interest, like CO_2 or CH_4, can be studied with in situ spatially resolved measurements of temperatures and product formation, to evaluate the extent by which vibrational nonequilibrium influences such a complex processes.

6

SUMMARY AND CONCLUSIONS

This thesis deals with the study of two promising plasma reactors for the electrification of the chemical industry: a NRP discharge for CO_2 dissociation and a microwave discharge for the vibrational activation of N_2. The deployment of laser diagnostics specifically designed for the investigation of those two plasma reactors represented a chief part of the whole thesis. Especially the case of LIF has been studied in detail because of its dependence upon interaction with collisional partners – and molecular plasmas are characterized by strong collisionality indeed.

The work is divided in two large parts with the NRP discharge investigated by LIF and the microwave discharge by Raman scattering. The common thread connecting these two studies is the in–situ investigation, performed by means of laser diagnostics, to reveal peculiar characteristics of each reactor. By using LIF, the temporal evolution of the absolute concentrations of OH and CO has been obtained. With Raman scattering, the degree of vibrational non–equilibrium has been mapped in the N_2 microwave discharge. Since the two studies are independent, conclusions are organized in the following two sections.

6.1 MEASUREMENTS OF OH BY LIF IN A NRP DISCHARGE FOR CO_2 DISSOCIATION

In order to use LIF for quantitative measurements, the quantum yield of the process needs to be known. Hence, detailed knowledge of the rate coefficients of the collisional partners present in the mixture is required. More specifically, this is necessary because both the intensity and the spectral feature of the fluorescence signal are modified by two concurring processes: electronic quenching (Q) and vibrational energy transfer (VET). On this regards, the measurements of Q and VET for a set of collisional partners commonly found in plasma–chemistry environments are reported in this thesis.

The investigation has been performed by resonant excitation of the OH $A^2\Sigma^+$ ($v' = 1$) state. Consequently, Q of both the A_0 and A_1 states, and VET between these two, were simultaneously obtained for each collisional partner. A novel data analysis method, working on the fluorescence pulse – where the contributions of A_0 and A_1 are not distinguished – and on the fluorescence spectrum, has been reported.

The obtained results have been carefully compared with the data already present in the literature. The comparison was made to high-

light the differences arising when the condition of rotational thermalization is satisfied, or not. Special attention has been devoted to this aspect since it is known that both Q and VET vary for different rotational levels. In conclusion, the obtained dataset is consistent with literature data, when it is present. Additionally, the knowledge on energy transfer rates of OH has been updated and extended, especially to VET and quenching of the A_1 state.

The measurements of collisional energy transfer rates on OH was not performed for its own sake, but it is rather propaedeutic to the quantification of OH in collisional environments. Such rate coefficients were then used for the quantification of OH in a NRP discharge for CO_2 dissociation.

The application of LIF to the study of a NRP discharge for CO_2 dissociation is definitely a challenging task. Fast and steep temperature and density variations define an environment extremely different from the gas cell where, by carefully controlling pressure, temperature and collider concentration, the collisional rate coefficients have been measured. Nevertheless, such knowledge obtained in a controlled environment is still valuable for real life applications.

Difficulties mainly arise from having to work with a pure molecular mixture that inevitably interferes with the measurement of LIF pulses, because of the very strong quenching. On one hand, molecular gases usually have a quenching rate coefficient much larger than the rotational energy transfer coefficient, $k_{Q0,Q1} \gg k_{RET}$, therefore precluding rotational thermalization of the excited state. Additionally, experimental conditions for which the quenching frequency is larger than the characteristic decay frequency of the laser pulse can be easily obtained. In these situations, the measurement of the LIF pulses cannot be used for the quantification of the target molecule. Hence, the discharge was operated in three different conditions of increasing complexity so as to demonstrate the use of LIF in such demanding collisional environments.

Firstly, the molecular mixture was diluted with helium – to decrease the effective quenching rate of the mixture – to measure both LIF pulses and spectra from which OH concentration could be measured quantitatively. Two different discharges, either with or without the use of a dielectric layer, have been tested on the same mixture, He + 4 Torr CO_2 + 0.75 Torr H_2O at 760 Torr. Obtained results showed relatively small concentration of OH, of the order of $10^{14}\,cm^{-3}$, two orders of magnitude smaller than the local CO concentration. The small concentration of OH, in conjunction with its temporal decay, too fast to be associated to the reaction $OH + CO \rightarrow CO_2 + H$, does not suggest a big role of OH in the CO back–reaction at these experimental conditions.

Complementary to the investigation of the CO_2/H_2O mixture diluted with helium, a NRP discharge in a CO_2 + 1% H_2O mixture

at 100 mbar has also been investigated as an industrially relevant reactor. In this case, quenching frequencies are too large and OH cannot be quantified. But every cloud has a silver lining, and when LIF ceases to be applicable a novel methodology named Collisional Energy Transfer LIF (CET–LIF) can be applied to study the composition of the gas mixture. Although sharing the same excitation–detection scheme, CET–LIF profoundly differs from LIF: CET–LIF uses the target molecule as a probe to obtain information about the composition of the mixture. Following this idea, CO_2 dissociation has been measured in a time resolved manner. Remarkable dissociation up to 80% was measured at short delay after the discharge event, to decrease steadily to a value of about 20%. Although the mechanisms behind such a temporal decay are not clear at this stage of research, the very high dissociation measured close to the discharge event indicates the potential of the NRP discharge.

6.2 VIBRATIONAL NON-EQUILIBRIUM IN N_2 MICROWAVE DISCHARGE

The work on the microwave discharge has been performed during my internship in the Non–equilibrium Fuel Conversion group headed by dr. ir. Gerard van Rooij, at DIFFER (Eindhoven, the Netherlands). A Raman scattering setup has been developed for the study of vibrational non–equilibrium in a N_2 microwave discharge.

As introduced in Chapter 4, vibrational energy is required to activate endothermic reactions. As described by Polanyi's laws, when reactants are vibrationally excited, that energy can be used to lower the energy barrier of the reaction. Consequently, reaction rates increase exponentially. In this context where vibrational energy is considered to be essential for the activation of endothermic reactions, it is natural to seek for reactors able to enhance such effect. Among the available plasma reactors, microwave discharges are expected to be particularly efficient in selectively loading energy in the vibrational mode.

A microwave flowing reactor has been investigated by means of Raman scattering. Specifically, radial profiles of vibrational and rotational temperatures were obtained. The reactor was operated at different pressures and input power to highlight the effect of such process parameters. In the low pressure regimes, with pressure lower than 50 mbar, rotational temperatures as high as 2000 K were measured in the centre of the plasma. The radial profiles then shows a decay down to about 500 K close to the reactor walls. At the same reactor conditions, vibrational temperature is generally higher for every radial position. The ratio between the two temperatures is chosen as good parameter to appreciate the degree of vibrational non–equilibrium. When calculated as function of the radial position, such ratio increases from about two, when measured in the centre of the

plasma, to about four close to the reactor walls. Conversely, when the reactor is operated at 800 mbar, very high rotational temperatures of about 7000 K are measured in the centre of the plasma. Additionally, the temperature ratio is close to unity at every radial position, indicating the thermal behaviour of the discharge.

The investigation of vibrational non–equilibrium was further extended to the calculation of the energy present in the rotational–translational and vibrational modes. A density profile was obtained from the same Raman spectra and used normalize the local energy density to the local number density. Ultimately, radial energy density profiles has been compared to the SEI to calculate the efficiency by which energy is loaded in the molecular gas. When such procedure is performed right outside the waveguide – so as to assure complete energy deposition from the plasma – it is found that about 35% of the SEI is specifically loaded in the vibrational mode, while if rotational and translational energies are added to the calculation the efficiency rises to 60%.

This study casts light on the potential that microwave discharges posses when vibrational excitation is desired. Since the discharge is run with pure N_2, the activated N_2 molecules are not exploited to synthesize any valuable compound. However, once the thermodynamic characteristics of the reactor are known, future studies can follow up with focus on vibrationally enhanced chemistry. For example, such an apparatus can be used to evaluate the synthesis of NO or CO when O_2 or CO_2 are added to the effluents, with the microwave flowing reactor used as a source of vibrationally excited N_2. Moreover, the applicability of the diagnostics is not limit to N_2 only, but can be extended to any gas that shows Raman activity. Specifically, the processing of other gases of interest, like CO_2 or CH_4, can be studied with in–situ spatially resolved measurements of temperatures and product concentration, to evaluate the extent by which vibrational non–equilibrium influences such a complex processes.

BIBLIOGRAPHY

[1] I V Adamovich, I Choi, N Jiang, J-H Kim, S Keshav, W R Lempert, E Mintusov, M Nishihara, M Samimy, and M Uddi. "Plasma assisted ignition and high-speed flow control: non-thermal and thermal effects". In: *Plasma Sources Science and Technology* 18.3 (2009), p. 034018.

[2] Gokhan Altinay and R. Glen Macdonald. "Determination of the Rate Constant for the $OH(X^2\Pi) + OH(X^2\Pi) \rightarrow H_2O + O(3P)$ Reaction Over the Temperature Range 295 to 701 K". In: *The Journal of Physical Chemistry A* 118.1 (2014), pp. 38–54. DOI: 10.1021/jp409344q.

[3] L. L. Alves. "The IST-Lisbon database on LXCat". In: *J. Phys. Conf. Series* 1 (2014).

[4] I. Armenise and F. Esposito. "N_2, O_2, NO state-to-state vibrational kinetics in hypersonic boundary layers: The problem of rescaling rate coefficients to uniform vibrational ladders". In: *Chemical Physics* 446.Supplement C (2015), pp. 30 –46. ISSN: 0301-0104. DOI: https://doi.org/10.1016/j.chemphys.2014.11.004.

[5] D. Arnoldi, K. Kaufmann, and J. Wolfrum. "Chemical Laser Induced Isotopically Selective Reaction of HCl". In: *Phys. Rev. Lett.* 34 (26 1975), pp. 1597–1600. DOI: 10.1103/PhysRevLett.34.1597.

[6] D. L. Baulch et al. "Evaluated Kinetic Data for Combustion Modelling". In: *J. Phys. Chem. Ref. Data* 21 (1992), pp. 411–734.

[7] Gert Due Billing and E.R. Fisher. "VV and VT rate coefficients in N_2 by a quantum-classical model". In: *Chemical Physics* 43.3 (1979), pp. 395–401. ISSN: 0301-0104. DOI: http://dx.doi.org/10.1016/0301-0104(79)85207-6.

[8] Waldo Bongers et al. "Plasma-driven dissociation of CO_2 for fuel synthesis". In: *Plasma Processes and Polymers* 14.6 (2017). 1600126, 1600126–n/a. ISSN: 1612-8869. DOI: 10.1002/ppap.201600126.

[9] Y.P. Butylkin, V.K. Zhivotov, E.G. Krasheninnikov, M.F. Krotov, V.D. Rusanov, Y.V. Tarasov, and A.A. Fridman. "Dissociation of CO_2 by a plasma–chemical process in a nonequilibrium microwave discharge". In: *Sov. Phys. - Tech. Phys. (Engl. Transl.); (United States)* 26:5 (May 1981).

[10] Pio Capezzuto, Francesco Cramarossa, Riccardo D'Agostino, and Ettore Molinari. "Contribution of vibrational excitation to the rate of carbon dioxide dissociation in electrical discharges". In: *The Journal of Physical Chemistry* 80.8 (1976), pp. 882–888. DOI: 10.1021/j100549a024.

[11] Mario Capitelli, ed. *Nonequilibrium Vibrational Kinetics*. Berlin, Heidelberg: Springer Berlin Heidelberg, 1986. ISBN: 978-3-642-48615-9. DOI: 10.1007/978-3-642-48615-9_2.

[12] M. Castela, S. Stepanyan, B. Fiorina, A. Coussement, O. Gicquel, N. Darabiha, and C. O. Laux. "A 3-D DNS and experimental study of the effect of the recirculating flow pattern inside a reactive kernel produced by nanosecond plasma discharges in a methane-air mixture". In: *Proceedings of the Combustion Institute* 36 (2017), pp. 4095 –4103. DOI: 10.1016/j.proci.2016.06.174.

[13] Robert J. Cattolica and Thomas G. Mataga. "Rotational-level-dependent quenching of OH by collisions with H2O in a low-pressure flame". In: *Chemical Physics Letters* 182.6 (1991), pp. 623 –631. ISSN: 0009-2614. DOI: https://doi.org/10.1016/0009-2614(91)90136-W.

[14] Guoxing Chen, Tiago Silva, Violeta Georgieva, Thomas Godfroid, Nikolay Britun, Rony Snyders, and Marie Paule Delplancke-Ogletree. "Simultaneous dissociation of CO2 and H2O to syngas in a surface-wave microwave discharge". In: *International Journal of Hydrogen Energy* 40.9 (2015), pp. 3789 –3796. DOI: http://dx.doi.org/10.1016/j.ijhydene.2015.01.084.

[15] N. Cherkasov, A.O. Ibhadon, and P. Fitzpatrick. "A review of the existing and alternative methods for greener nitrogen fixation". In: *Chemical Engineering and Processing: Process Intensification* 90 (2015), pp. 24 –33. ISSN: 0255-2701. DOI: http://dx.doi.org/10.1016/j.cep.2015.02.004.

[16] R. A. Copeland, M. J. Dyer, and D. R. Crosley. "Rotational-level-dependent quenching of A 2 + OH and 00". In: *J. Chem. Phys.* 82 (1985), pp. 4022–4032.

[17] R. A. Copeland, M. L. Wise, and D. R. Crosley and. "Vibrational energy transfer and quenching of OH($A^2\Sigma^+, v' = 1$)". In: *J. Phys. Chem.* 92 (1988), p. 5710.

[18] David R. Crosley. "Rotational and translation effects in collisions of electronically excited diatomic hydrides". In: *The Journal of Physical Chemistry* 93.17 (1989), pp. 6273–6282. DOI: 10.1021/j100354a005.

[19] C. Dang, J. Reid, and B. K. Garside. "Detailed vibrational population distributions in a CO2 laser discharge as measured with a tunable diode laser". In: *Applied Physics B* 27.3 (1982), pp. 145–151. ISSN: 1432-0649. DOI: 10.1007/BF00694640.

[20] G. Dilecce. "Optical spectroscopy diagnostics of discharges at atmospheric pressure". In: *Plasma Sources Sci. Technol.* 23 (2014), p. 015011. DOI: 10.1088/0963-0252/23/1/015011.

[21] G Dilecce and S De Benedictis. "Laser diagnostics of high-pressure discharges: laser induced fluorescence detection of OH in He/Ar–H 2 O dielectric barrier discharges". In: *Plasma Physics and Controlled Fusion* 53.12 (2011), p. 124006.

[22] G. Dilecce, L. M. Martini, P. Tosi, M. Scotoni, and S. De Benedictis. "Laser induced fluorescence in atmospheric pressure discharges". In: *Plasma Sources Sci. Technol.* 24 (2015), p. 034007.

[23] Baldur Eliasson, Ulrich Kogelschatz, Bingzhang Xue, and Li-Ming Zhou. "Hydrogenation of Carbon Dioxide to Methanol with a Discharge-Activated Catalyst". In: *Industrial & Engineering Chemistry Research* 37.8 (1998), pp. 3350–3357. DOI: 10.1021/ie9709401.

[24] Omar Ellabban, Haitham Abu-Rub, and Frede Blaabjerg. "Renewable energy resources: Current status, future prospects and their enabling technology". In: *Renewable and Sustainable Energy Reviews* 39 (2014), pp. 748 –764. ISSN: 1364-0321. DOI: http://dx.doi.org/10.1016/j.rser.2014.07.113.

[25] Fleming Crim F. "Chemical dynamics of vibrationally excited molecules: Controlling reactions in gases and on surfaces". In: *PNAS* 105.36 (2008), pp. 12654–12664. DOI: 10.1073/pnas.0803010105.

[26] Joseph Fielding, Jonathan H. Frank, Sebastian A. Kaiser, Mitchell D. Smooke, and Marshall B. Long. "Polarized/depolarized rayleigh scattering for determining fuel concentrations in flames". In: *Proceedings of the Combustion Institute* 29.2 (2002), pp. 2703 –2709. ISSN: 1540-7489. DOI: http://dx.doi.org/10.1016/S1540-7489(02)80329-7.

[27] Kraig Frederickson, Yi-Chen Hung, Walter R Lempert, and Igor V Adamovich. "Control of vibrational distribution functions in nonequilibrium molecular plasmas and high-speed flows". In: *Plasma Sources Science and Technology* 26.1 (2017), p. 014002.

[28] A. A. Fridman and V. D Rusanov. "Theoretical basis of non-equilibrium near atmospheric pressure plasma chemistry". In: *Pure & Appl. Chem.* 66 (6 1994), pp. 1267–1274.

[29] Alexander Fridman. *Plasma chemistry*. Cambridge university press, 2008.

[30] Javier F. de la Fuente, Sergio H. Moreno, Andrzej I. Stankiewicz, and Georgios D. Stefanidis. "Reduction of CO2 with hydrogen in a non-equilibrium microwave plasma reactor". In: *International Journal of Hydrogen Energy* 41.46 (2016), pp. 21067 –21077. DOI: http://dx.doi.org/10.1016/j.ijhydene.2016.08.032.

[31] A Gicquel, S Cavadias, and J Amouroux. "Heterogeneous catalysis in low-pressure plasmas". In: *Journal of Physics D: Applied Physics* 19.11 (1986), p. 2013.

[32] D. Giordano, V. Bellucci, G. Colonna, M. Capitelli, I. Armenise, and C. Bruno. "Vibrationally Relaxing Flow of N past an Infinite Cylinder". In: *Journal of Thermophysics and Heat Transfer* 11.1 (1997), pp. 27–35. DOI: https://doi.org/10.2514/2.6219.

[33] B. F. Gordiets, S. S. Mamedov, and L. A. Shelepin. "Vibrational kinetics of anharmonic oscillators under essentially nonequilibrium conditions". In: *Zhurnal Eksperimentalnoi i Teoreticheskoi Fiziki* 67 (Oct. 1974), pp. 1287–1300.

[34] David B Graves. "The emerging role of reactive oxygen and nitrogen species in redox biology and some implications for plasma applications to medicine and biology". In: *Journal of Physics D: Applied Physics* 45.26 (2012), p. 263001.

[35] Niek den Harder et al. "Homogeneous CO_2 conversion by microwave plasma: Wave propagation and diagnostics". In: *Plasma Processes and Polymers* 14.6 (2017). 1600120, 1600120–n/a. ISSN: 1612-8869. DOI: 10.1002/ppap.201600120.

[36] Gerhard Herzberg. *Molecular spectra and molecular structure. Infrared and Raman spectra of polyatomic molecules*. Vol. 1. D. VAN NOSTRAN COMPANY, Inc., 1945.

[37] Gerhard Herzberg. *Molecular spectra and molecular structure. Spectra of Diatomic Molecules*. Vol. 1. D. VAN NOSTRAN COMPANY, Inc., 1950.

[38] L. D. Hinkle and C. F. Mariano. "Toward understanding the fundamental mechanisms and properties of the thermal mass flow controller". In: *J. Vac. Sci. Technol., A* 9 (1991), p. 2043.

[39] Uwe Hohm and Klaus Kerl. "Temperature dependence of mean molecular polarizability of gas molecules". In: *Molecular Physics* 58.3 (1986), pp. 541–550. DOI: 10.1080/00268978600101351.

[40] Asisov R. I., Givotov V. K., Rusanov V. D., and Fridman A. In: *Sov. Phys. High Energy Chemistry* 14 (1980), p. 366.

[41] Witteman W. J. *The CO_2 laser*. Springer Series in Optical Sciences, 1987. ISBN: 978-3-662-13617-1.

[42] A. Jorg, A. Degli Esposti, and H. J. Werner. "Quantum scattering study of rotational energy transfer in OH(A 2+, v'=0) in collisions with He(1 S)". In: *J. Chem. Phys.* 93 (1990), p. 8757.

[43] E. Jwa, S.B. Lee, H.W. Lee, and Y.S. Mok. "Plasma-assisted catalytic methanation of CO and CO2 over Nizeolite catalysts". In: *Fuel Processing Technology* 108 (2013). Special Issue of APCRE11, pp. 89 –93. DOI: http://dx.doi.org/10.1016/j.fuproc.2012.03.008.

[44] R. Kienle, A. Jorg, and K. Kohse-Hoinghaus. "State-to-state rotational energy transfer in OH(A,v=1)". In: *Appl. Phys. B* 56 (1993), pp. 249 –258.

[45] R. Kienle, M. P. Lee, and K. Kohse-Hoinghaus. "A scaling formalism for the representation of rotational energy transfer in OH". In: *Appl. Phys. B* 63 (1996), pp. 403 –418.

[46] B. L. M. Klarenaar, F. Brehmer, S. Welzel, H. J. van der Meiden, M. C. M. van de Sanden, and R. Engeln. "Note: Rotational Raman scattering on CO2 plasma using a volume Bragg grating as a notch filter". In: *Review of Scientific Instruments* 86.4 (2015), p. 046106. DOI: 10.1063/1.4918730.

[47] E.V. Kustova and E.A. Nagnibeda. "On a correct description of a multi-temperature dissociating CO2 flow". In: *Chemical Physics* 321.3 (2006), pp. 293 –310. ISSN: 0301-0104. DOI: https://doi.org/10.1016/j.chemphys.2005.08.026.

[48] L. Landau and Teller E. In: *Physik Z. Sowjetunion* 10.34 (1936).

[49] Wonchul Lee, Igor V. Adamovich, and Walter R. Lempert. "Optical pumping studies of vibrational energy transfer in high-pressure diatomic gases". In: *The Journal of Chemical Physics* 114.3 (2001), pp. 1178–1186. DOI: 10.1063/1.1332400.

[50] J.C. Legrand, A.M. Diamy, R. Hrach, and V. Hrachova. "Methane Conversion in the Flowing Afterglow of a Dinitrogen Microwave Plasma: Initiation of the Reaction". In: *Contributions to Plasma Physics* 37.6 (1997), pp. 521–537. ISSN: 1521-3986. DOI: 10.1002/ctpp.2150370606.

[51] Ming-wei Li, Gen-hui Xu, Yi-ling Tian, Li Chen, and Hua-feng Fu. "Carbon Dioxide Reforming of Methane Using DC Corona Discharge Plasma Reaction". In: *The Journal of Physical Chemistry A* 108.10 (2004), pp. 1687–1693. DOI: 10.1021/jp037008q.

[52] A. Lo, A. Cessou, C. Lacour, B. Lecordier, P. Boubert, D. A. Xu, C. O. Laux, and P. Vervisch. "Streamer-to-spark transition initiated by a nanosecond overvoltage pulsed discharge in air". In: *Plasma Sources Sci. Technol.* 26.4 (2017), p. 045012. DOI: 10.1088/1361-6595/aa5c78.

[53] Derek A Long. "The Raman effect: a unified treatment of the theory of Raman scattering by molecules". In: *West Sussex* (2002).

[54] J Luque and D Crosley. *SRI Int. Rep. MP 99-009*. 1999.

[55] J. Luque and D.R. Crosley. "LIFBASE: Database and Spectral Simulation Program (Version 1.5)". In: *SRI International Report MP* (1999).

[56] Brown J. M. and Carrington A. *Rotational Spectroscopy of Diatomic Molecules*. Cambridge, 2003. ISBN: 9780521530781.

[57] Doroshenko V. M., Kudryavtsev N. N., Novikov S. S., and Smetanin V. V. "Dependence of heat transfer on the formation of vibrationally excited nitrogen molecules during the recombination of atoms in a boundary layer". In: *High Temperature* 28 (1990).

[58] Martini L. M. "Density measurement of OH radicals in non-thermal plasmas by laser induced fluorescence and time-resolved absorption spectroscopy". PhD thesis. University of Trento, Department of Physics, 2015.

[59] S. L. Manatt and M. R. R. Manatt. "On the Analyses of Mixture Vapor Pressure Data: The Hydrogen Peroxide/Water System and Its Excess Thermodynamic Functions". In: *Chem. Eur. J.* 10.24 (2004), pp. 6540–6557.

[60] L. M. Martini, G. Dilecce, G. Guella, A. Maranzana, G. Tonachini, and P. Tosi. "Oxidation of CH_4 by CO_2 in a dielectric barrier discharge". In: *Chem. Phys. Lett.* 593 (2014), pp. 55 –60. DOI: 10.1016/j.cplett.2013.12.069.

[61] L. M. Martini, N. Gatti, G. Dilecce, M. Scotoni, and P. Tosi. "Rate constants of quenching and vibrational relaxation in the $OH(A^2\Sigma^+, v = 0, 1)$, manifold with various colliders". In: *J. Phys. D: Appl. Phys.* 50 (2017), p. 114003. DOI: 10.1088/1361-6463/aa5b28.

[62] Luca Matteo Martini, Giorgio Dilecce, Mario Scotoni, Paolo Tosi, and Santolo De Benedictis. "OH Density Measurements by Time-Resolved Broad Band Absorption Spectroscopy in a He–H_2O Dielectric Barrier Discharge with Small O_2 Addition". In: *Plasma Processes and Polymers* 11.3 (2014), pp. 232–238. ISSN: 1612-8869. DOI: 10.1002/ppap.201300116.

[63] Luca Matteo Martini, Andrea Maranzana, Glauco Tonachini, Giulia Bortolotti, Marco Scapinello, Mario Scotoni, Graziano Guella, Giorgio Dilecce, and Paolo Tosi. "Reactivity of fatty acid methyl esters under atmospheric pressure plasma jet exposure: An experimental and theoretical study". In: *Plasma Processes and Polymers* (2017). doi: 10.1002/ppap.201600254. DOI: 10.1002/ppap.201600254.

[64] H. J. van der Meiden et al. "High sensitivity imaging Thomson scattering for low temperature plasma". In: *Review of Scientific Instruments* 79.1 (2008), p. 013505. DOI: 10.1063/1.2832333.

[65] R. F. G. Meulenbroeks, D. C. Schram, L. J. M. Jaegers, and M. C. M. van de Sanden. "Depolarization Rayleigh scattering as a means of molecular concentration determination in plasmas". In: *Phys. Rev. Lett.* 69 (9 Aug. 1992), pp. 1379–1382. DOI: 10.1103/PhysRevLett.69.1379.

[66] Richard B Miles, Walter R Lempert, and Joseph N Forkey. "Laser Rayleigh scattering". In: *Measurement Science and Technology* 12.5 (2001), R33.

[67] C. Bradley Moore, Robert E. Wood, Bei-Lok Hu, and James T. Yardley. "Vibrational Energy Transfer in CO2 Lasers". In: *The Journal of Chemical Physics* 46.11 (1967), pp. 4222–4231. DOI: 10.1063/1.1840527.

[68] M. Mosburger and V. Sick. "Single laser detection of CO and OH via laser-induced fluorescence". In: *Appl. Phys. B* 99 (2010), pp. 1 –6. DOI: 10.1007/s00340-010-3896-y.

[69] K Muraoka and M Maeda. "Application of laser-induced fluorescence to high-temperature plasmas". In: *Plasma Physics and Controlled Fusion* 35.6 (1993), p. 633.

[70] E. E. Nikitin and J. Troe. "70 years of Landau-Teller theory for collisional energy transfer. Semiclassical three-dimensional generalizations of the classical collinear model". In: *Phys. Chem. Chem. Phys.* 10 (11 2008), pp. 1483–1501. DOI: 10.1039/B715095D.

[71] *NIST Chemistry WebBook*. URL: http://webbook.nist.gov/chemistry/.

[72] Truman J Odiorne, Philip R. Brooks, and Jerome V. V. Kasper. "Molecular Beam Reaction of K with HCl: Effect of Vibrational Excitation of HCl". In: *The Journal of Chemical Physics* 55.4 (1971), pp. 1980–1982. DOI: 10.1063/1.1676338.

[73] R. Ono. "Optical diagnostics of reactive species in atmospheric-pressure nonthermal plasma". In: *Journal of Phys. D: Appl. Phys.* 49 (2016), p. 083001.

[74] Forster P. et al. In: *Changes in Atmospheric Constituents and in Radiative Forcing Chapter 2*. Cambridge University Press, 2007.

[75] J. G. Parker. "Rotational and Vibrational Relaxation in Diatomic Gases". In: *The Physics of Fluids* 2.4 (1959), pp. 449–462. DOI: 10.1063/1.1724417.

[76] P. H. Paul. "Vibrational Energy Transfer and Quenching of OH $A^2\Sigma^+$ ($v' = 0$) Measured at High Temperatures in a Shock Tube". In: *The Journal of Physical Chemistry* 99.21 (1995), pp. 8472–8476. DOI: 10.1021/j100021a004.

[77] P.H. Paul. "A model for temperature-dependent collisional quenching of OH $A^2\Sigma^+$". In: *Journal of Quantitative Spectroscopy and Radiative Transfer* 51.3 (1994), pp. 511 –524. ISSN: 0022-4073. DOI: https://doi.org/10.1016/0022-4073(94)90150-3.

[78] X. Pei, S. Wu, Y. Xian, X. Lu, and Y. Pan. "On OH Density of an Atmospheric Pressure Plasma Jet by Laser-Induced Fluorescence". In: *IEEE Trans. Plasma Sci.* 42 (2014), pp. 1206–1210.

[79] N. Pinhão, A. Moura, J.B. Branco, and J. Neves. "Influence of gas expansion on process parameters in non-thermal plasma plug-flow reactors: A study applied to dry reforming of methane". In: *International Journal of Hydrogen Energy* 41.22 (2016), pp. 9245 –9255. DOI: https://doi.org/10.1016/j.ijhydene.2016.04.148.

[80] J. C. Polanyi and W. H. Wong. "Location of Energy Barriers. I. Effect on the Dynamics of Reactions A + BC". In: *The Journal of Chemical Physics* 51.4 (1969), pp. 1439–1450. DOI: 10.1063/1.1672194.

[81] I.C. Prentice, G.D. Farquhar, M.J.R. Fasham, M.L. Goulden, M. Heimann, V.J. Jaramillo, H.S. Kheshgi, C. LeQuéré, R.J. Scholes, and Douglas W.R. Wallace. "The Carbon Cycle and Atmospheric Carbon Dioxide". In: *Climate Change 2001: the Scientific Basis. Contributions of Working Group I to the Third Assessment Report of the Intergovernmental Panel on Climate Change*. Ed. by J.T. Houghton, Y. Ding, D.J. Griggs, M. Noguer, P.J. van der Linden, X. Dai, K. Maskell, and C.A. Johnson. Cambridge, UK: Cambridge University Press, 2001, pp. 185–237.

[82] Krishna Priya Arjunan and Alisa Morss Clyne. "Hydroxyl Radical and Hydrogen Peroxide are Primarily Responsible for Dielectric Barrier Discharge Plasma-Induced Angiogenesis". In: *Plasma Processes and Polymers* 8.12 (2011), pp. 1154–1164. ISSN: 1612-8869. DOI: 10.1002/ppap.201100078.

[83] T.M. Razykov, C.S. Ferekides, D. Morel, E. Stefanakos, H.S. Ullal, and H.M. Upadhyaya. "Solar photovoltaic electricity: Current status and future prospects". In: *Solar Energy* 85.8 (2011). Progress in Solar Energy 1, pp. 1580 –1608. ISSN: 0038-092X. DOI: http://dx.doi.org/10.1016/j.solener.2010.12.002.

[84] Gustav Resch, Anne Held, Thomas Faber, Christian Panzer, Felipe Toro, and Reinhard Haas. "Potentials and prospects for renewable energies at global scale". In: *Energy Policy* 36.11 (2008). Transition towards Sustainable Energy Systems, pp. 4048 –4056. ISSN: 0301-4215. DOI: http://dx.doi.org/10.1016/j.enpol.2008.06.029.

[85] J. William Rich. "4 - Relaxation of Molecules Exchanging Vibrational Energy". In: *Gas Lasers*. Ed. by E.W. McDANIEL and WILLIAM L. NIGHAN. Academic Press, 1982, pp. 99 –140. ISBN: 978-0-12-478803-9. DOI: https://doi.org/10.1016/B978-0-12-478803-9.50010-0.

[86] J.William Rich, Sergey O. Macheret, and Igor V. Adamovich. "Aerothermodynamics of vibrationally nonequilibrium gases". In: *Experimental Thermal and Fluid Science* 13.1 (1996), pp. 1 –10. ISSN: 0894-1777. DOI: http://dx.doi.org/10.1016/0894-1777(95)00128-X.

[87] D. Ries, G. Dilecce, E. Robert, P.F. Ambrico, S. Dozias, and J.-M. Pouvesle. "LIF and Fast imaging plasma jet characterization relevant for NTP biomedical applications". In: *J. Phys D: Appl. Phys.* 47 (2014), p. 275401.

[88] Pachauri R.K. and Meyer L.A. In: *IPCC, 2014: Climate Change 2014: Synthesis Report. Contribution of Working Groups I, II and III to the Fifth Assessment Report of the Intergovernmental Panel on Climate Change IPCC, Geneva.*

[89] G. J. van Rooij, D. C. M. van den Bekerom, N. den Harder, T. Minea, G. Berden, W. A. Bongers, R. Engeln, M. F. Graswinckel, E. Zoethout, and M. C. M. van de Sanden. "Taming microwave plasma to beat thermodynamics in CO_2 dissociation". In: *Faraday Discuss.* 183 (0 2015), pp. 233–248. DOI: 10.1039/C5FD00045A.

[90] V. D Rusanov, A. A. Fridman, and Sholin G. V. In: *Usp. Fiz. Nauk* 134 (1981), pp. 185–235.

[91] M. Scapinello, L. M. Martini, G. Dilecce, and P. Tosi. "Conversion of CH_4 /CO_2 by a nanosecond repetitively pulsed discharge". In: *J. Phys. D: Appl. Phys.* 49 (2016), p. 075602.

[92] M Scapinello, L M Martini, G Dilecce, and P Tosi. "Conversion of CH_4/CO_2 by a nanosecond repetitively pulsed discharge". In: *Journal of Physics D: Applied Physics* 49.7 (2016), p. 075602.

[93] Marco Scapinello, Luca Matteo Martini, and Paolo Tosi. "CO_2 Hydrogenation by CH_4 in a Dielectric Barrier Discharge: Catalytic Effects of Nickel and Copper". English. In: *Plasma Process. Polym.* 11 (2014), 624–628. DOI: {10.1002/ppap.201400023}.

[94] George Scatchard, George M. Kavanagh, and Leland B. Ticknor. "Vapor-Liquid Equilibrium. VIII. Hydrogen Peroxide—Water Mixtures1". In: *Journal of the American Chemical Society* 74.15 (1952), pp. 3715–3720. DOI: 10.1021/ja01135a001.

[95] Richard R. Schrock. "Reduction of dinitrogen". In: *Proceedings of the National Academy of Sciences* 103.46 (2006), p. 17087. DOI: 10.1073/pnas.0603633103. eprint: http://www.pnas.org/content/103/46/17087.full.pdf.

[96] Erwin Schrodinger. *What is life?: The physical aspect of the living cell*. The Macmillan company, 1946.

[97] W. C. Schumb, C. N. Satterfield, and R. L. Wentworth. *Hydrogen Peroxide, A.C.S. Monograph No. 128*. Reinhold Publishing Corporation, New York, 1955.

[98] R. R. Smith, D. R. Killelea, D. F. DelSesto, and A. L. Utz. "Preference for Vibrational over Translational Energy in a Gas-Surface Reaction". In: *Science* 304.5673 (2004), pp. 992–995. ISSN: 0036-8075. DOI: 10.1126/science.1096309. eprint: http://science.sciencemag.org/content/304/5673/992.full.pdf.

[99] R. Snoeckx, Y. X. Zeng, X. Tu, and A. Bogaerts. "Plasma-based dry reforming: improving the conversion and energy efficiency in a dielectric barrier discharge". In: *RSC Adv.* 5 (38 2015), pp. 29799–29808. DOI: 10.1039/C5RA01100K.

[100] Ramses Snoeckx, Alp Ozkan, Francois Reniers, and Annemie Bogaerts. "The Quest for Value-Added Products from Carbon Dioxide and Water in a Dielectric Barrier Discharge: A Chemical Kinetics Study". In: *ChemSusChem* 10.2 (2017), pp. 409–424. ISSN: 1864-564X. DOI: 10.1002/cssc.201601234.

[101] Ramses Snoeckx, Alp Ozkan, Francois Reniers, and Annemie Bogaerts. "The Quest for Value-Added Products from Carbon Dioxide and Water in a Dielectric Barrier Discharge: A Chemical Kinetics Study". In: *ChemSusChem* 10 (2017), pp. 409–424. DOI: 10.1002/cssc.201601234.

[102] S M Starikovskaia. "Plasma assisted ignition and combustion". In: *Journal of Physics D: Applied Physics* 39.16 (2006), R265.

[103] Andrey Starikovskiy and Nickolay Aleksandrov. "Plasma-assisted ignition and combustion". In: *Progress in Energy and Combustion Science* 39.1 (2013), pp. 61 –110. ISSN: 0360-1285. DOI: https://doi.org/10.1016/j.pecs.2012.05.003.

[104] Kristen L. Steffens and David R. Crosley. "Vibrational energy transfer in OH $A^2\Sigma^+$ between 195 and 295 K". In: *The Journal of Chemical Physics* 112.21 (2000), pp. 9427–9432. DOI: 10.1063/1.481562.

[105] S.R. Sun, H.X. Wang, D.H. Mei, X. Tu, and A. Bogaerts. "CO_2 conversion in a gliding arc plasma: Performance improvement based on chemical reaction modeling". In: *Journal of CO2 Utilization* 17.Supplement C (2017), pp. 220 –234. ISSN: 2212-9820. DOI: https://doi.org/10.1016/j.jcou.2016.12.009.

[106] Francesco Taccogna and Giorgio Dilecce. "Non-equilibrium in low-temperature plasmas". In: *Eur. Phys. J. D* 70.11 (2016), p. 251. DOI: 10.1140/epjd/e2016-70474-0.

[107] M. Tamura, P. A. Berg, J. E. Harrington, J. Luque, J. B. Jeffries, G. P. Smith, and D. R. Crosley. "Collisional Quenching of CH(A), OH(A), and NO(A) in Low Pressure Hydrocarbon Flames". In: *Combust. Flame* 114 (1998), pp. 502 –514. DOI: 10-2180/98/$19.00.

[108] G. Tejeda, B. Mate, and S. Montero. "Overtone Raman spectrum and molecular polarizability surface of CO_2". In: *The Journal of Chemical Physics* 103.2 (1995), pp. 568–576. DOI: 10.1063/1.470091.

[109] Y. Teramoto, H.-H. Kim, A. Ogata, and N. Negishi. "Measurement of OH (X 2) in immediate vicinity of dielectric surface under pulsed dielectric barrier discharge at atmospheric pressure using two geometries of laseri nduced fluorescence". In: *J. Appl. Phys.* 115 (2014), p. 133302. DOI: 10.1063/1.4870598.

[110] C. E. Treanor, J. W. Rich, and R. G. Rehm. "Vibrational Relaxation of Anharmonic Oscillators with Exchange-Dominated Collisions". In: *The Journal of Chemical Physics* 48.4 (1968), pp. 1798–1807. DOI: 10.1063/1.1668914.

[111] Xin Tu and J. Christopher Whitehead. "Plasma dry reforming of methane in an atmospheric pressure AC gliding arc discharge: Co-generation of syngas and carbon nanomaterials". In: *Int. J. Hydrogen Energy* 39 (2014), pp. 9658 –9669. DOI: http://dx.doi.org/10.1016/j.ijhydene.2014.04.073.

[112] Wandinger U. *Raman Lidar*. Springer Series in Optical Sciences. Springer, New York, NY, 2005. DOI: https://doi.org/10.1007/0-387-25101-4_9.

[113] W. Urban, J.-X. Lin, V.V. Subramaniam, M. Havenith, and J.W. Rich. "Treanor pumping of CO initiated by CO laser excitation". In: *Chemical Physics* 130.1 (1989), pp. 389 –399. ISSN: 0301-0104. DOI: http://dx.doi.org/10.1016/0301-0104(89)87068-5.

[114] T. Verreycken and P. J. Bruggeman. "OH density in atmospheric N2–H2O mixtures". In: *Plasma Sources Sci. Technol.* 23 (2014), p. 015009. DOI: 10.1088/0963-0252/23/1/015009.

[115] J. Voráč, A. Obrusník, V. Procházka, P. Dvořák, and M. Talába. "Spatially resolved measurement of hydroxyl radical (OH) concentration in an argon RF plasma jet by planar laser-induced fluorescence". In: *Plasma Sources Sci. Technol.* 23 (2014), p. 025011. DOI: 10.1088/0963-0252/23/2/025011.

[116] Li Wang, Yanhui Yi, Chunfei Wu, Hongchen Guo, and Xin Tu. "One-Step Reforming of CO2 and CH4 into High-Value Liquid Chemicals and Fuels at Room Temperature by Plasma-Driven Catalysis". In: *Angewandte Chemie International Edition*

56.44 (2017), pp. 13679–13683. ISSN: 1521-3773. DOI: 10.1002/anie.201707131.

[117] P. Wienecke, H. Finsterhölzl, H. W. Schrötter, and J. Brandmüller. "Raman Spectra of Carbon Dioxide and its Isotopic Variants in the Fermi Resonance Region. Part IV: Temperature Dependence on Q-Branch Intensities from 300 K to 650 K". In: *Applied Spectroscopy* 40.1 (1986), pp. 70–76. DOI: 10.1366/0003702864815411.

[118] L. R. Williams and D. R. Crosley. "Collisional vibrational energy transfer of OH (A)". In: *J. Chem. Phys.* 104 (1996), pp. 6507–6514.

[119] I. J. Wysong, J. B. Jeffries, and D. R. Crosley. "Quenching of $A^2\Sigma^+$ OH at 300 K by several colliders". In: *J. Chem. Phys* 92 (1990), pp. 5218–5222.

[120] Q. Xiong, A. Y. Nikiforov, L. Li, P. Vanraes, N. Britun, R. Snyders, X. P. Lu, and C. Leys. "Absolute OH density determination by laser induced fluorescence spectroscopy in an atmospheric pressure RF plasma jet". In: *Eur. Phys. J. D* 66 (2012), p. 281. DOI: 10.1140/epjd/e2012-30474-8.

[121] Y.L. Yung and W.B. DeMore. *Photochemistry of Planetary Atmospheres*. Oxford University Press, 1999.

[122] Y. Zeng and X. Tu. "Plasma-Catalytic CO2 Hydrogenation at Low Temperatures". In: *IEEE Transactions on Plasma Science* 44.4 (2016), pp. 405–411. DOI: 10.1109/TPS.2015.2504549.

[123] Xiuling Zhang, Aimin Zhu, Xuehui Li, and Weimin Gong. "Oxidative dehydrogenation of ethane with CO2 over catalyst under pulse corona plasma". In: *Catalysis Today* 89.1 (2004), pp. 97–102.